Alma Mater Studiorum · Università di Bologna

Scuola di Scienze
Corso di Laurea Magistrale in Fisica

An inter-comparison between a VIS/IR and a MW satellite-based methods for cloud detection and classification

Relatore:

Prof. Vincenzo Levizzani

Presentata da:

Francesca Vittorioso

Correlatori:

Dott.ssa Elsa Cattani
Dott. Sante Laviola

Sessione II

Anno Accademico 2014/2015

Alla mia famiglia:
mamma, papà e Antonio.

« ... On a stormy sea of moving emotion
Tossed about I'm like a ship on the ocean
I set a course for winds of fortune
But I hear the voices say

Carry on my wayward son
There'll be peace when you are done
Lay your weary head to rest
Don't you cry no more ... »

KANSAS, *Carry on my wayward son (1976)*

ABSTRACT

Il presente lavoro di tesi magistrale è stato sviluppato con lo scopo di valutare affinità e discordanze fra gli output di due metodi indipendenti per la quantificazione e classificazione della copertura nuvolosa, che si fondano su basi fisiche molto differenti. Uno di essi è il pacchetto software della Satellite Application Facility in support of NoWCasting and very short range forecasting (SAFNWC), sviluppato per elaborare i dati acquisiti dal sensore Spinning Enhanced Visible and Infrared Imager (SEVIRI) nel range del visibile e infrarosso. L'altro è l'algoritmo MicroWave Cloud-type Classification (MWCC), il quale utilizza le temperature di brillanza acquisite dai sensori Advanced Microwave Sounding Unit B (AMSU-B) e Microwave Humidity Sounder (MHS) nei loro canali centrati sulla banda di assorbimento del vapore acqueo nelle microonde a 183.31 GHz.

Nella prima parte del lavoro è stata testata la capacità dei due diversi metodi di rilevare la presenza di nubi, comparando, tramite statistica dicotomica, le Cloud Masks da essi prodotte. Questa analisi ha mostrato un buon accordo fra i due metodi, sebbene alcuni punti critici siano emersi. L'MWCC, in effetti, non riesce ad individuare la presenza di nubi che, secondo la classificazione della SAFNWC, sono nubi fratte, cirri, nubi molto basse oppure alte e opache.

Nella seconda fase del confronto, invece, sono stati analizzati i pixel identificati come nuvolosi da entrambi i software coinvolti, al fine di poter valutare il loro livello di accordo anche nella classificazione. La tendenza generale mostrata dall'MWCC rispetto alla SAFNWC è di sovrastima delle classi di nubi più basse. Viceversa, più l'altezza delle classi cresce, più l'algoritmo alle microonde manca nel rivelare una porzione di nubi che, invece, viene registrata tramite il tool della SAFNWC. Questo è complessivamente quello che si riscontra anche da una serie di test effettuati usando le informazioni di altezza del top fornite dalla SAFNWC per valutare l'affidabilità dei range di altezza in cui sono definite le varie classi dell'MWCC.

Dunque, sebbene i metodi in questione si propongano di fornire lo stesso tipo di informazioni, in realtà essi restituiscono dettagli piuttosto differenti sulla stessa colonna atmosferica. Il tool della SAFNWC, essendo molto sensibile alla temperatura del top della nube, cattura l'effettivo livello da questo raggiunto. L'MWCC, d'altra parte, sfruttando le capacità delle microonde, è in grado di restituire un'informazione sugli strati nuvolosi che si trovano più in profondità.

The present Master thesis has been developed with the aim to assess similarities and mismatches between the outputs from two independent methods for the cloud cover quantification and classification. More specifically the two methods work on quite different physical basis. One of them is the SAFNWC software package

designed to process radiance data acquired by the SEVIRI sensor in the visible and infrared (VIS/IR) range. The other is the MWCC algorithm, which uses the brightness temperatures acquired by the AMSU-B and MHS sensors in their channels centered in the microwave (MW) water vapour absorption band at 183.31 GHz.

At a first stage their cloud detection capability has been tested, by comparing the Cloud Masks they produced through the dichotomus statistics. This analysis showed a good agreement between two methods, although some critical situations stand out. The MWCC, in effect, fails to reveal clouds which according to SAFNWC are fractional cirrus, very low and high opaque clouds.

In the second stage of the inter-comparison the pixels classified as cloudy according to both softwares have been analysed in order to assess the agreement in the cloud classiffication. The overall observed tendency of the MWCC method, with respect to the SAFNWC one, is an overestimation of the lower cloud classes. In other words, the lower is the cloud top, the more MWCC seems to be able to detect it. Viceversa, the more the cloud top height increases, the more the MWCC does not reveal a certain cloud portion, rather detected by means of the SAFNWC tool. This is what also emerges from a series of tests carried out by using the cloud top height information in order to evaluate the height ranges in which each MWCC category is defined.

Therefore, although the involved methods intend to provide the same kind of information, in reality they return quite different details on the same atmospheric column. The SAFNWC retrieval tool, in effect, being very sensitive to the top temperature of a cloud, brings the actual level reached by this. The MWCC, on the other hand, exploiting the capability of the microwaves is able to give an information about the levels that are located more deeply within the atmospheric column.

CONTENTS

LIST OF FIGURES

LIST OF TABLES

1

INTRODUCTION

"Fuori s'estende la terra vuota fino all'orizzonte, s'apre il cielo dove corrono le nuvole. Nella forma che il caso e il vento danno alle nuvole l'uomo è già intento a riconoscere figure..."

– Italo Calvino, *Le città invisibili*

Every day looking at the sky, we get to see the wonderful sight offered by the clouds. As it appears they differ in shape, color, thickness. Some of them cause precipitation, others do not.

In addition to their enchanting and moving appearance, clouds play a very important role in the mechanisms regulating life on Earth. They are an essential component of the Earth's water cycle and global energy balance. Moreover, they are one of the most complex element in climate and atmospheric physics.

The capability to quantify with a good confidence degree the cloud cover over a region may have practical implications on the further cloud characterization (e.g. optical depth, phase, top temperature, etc.), which in turn is fundamental to derive atmospheric or surface parameters and to give insights into weather and climate processes. Different cloud types on the other hand are associated to peculiar phenomena of which clouds are tracers or precursors. Consider for example storms associated with cumulonimbus or the foehn associated with altocumulus lenticularis and rotors downwind. Thus, having a proper classification of clouds can provide a support to the forecasts of local thunderstorm activity that numerical models struggle to simulate.

Cloud detection and classification, therefore, is a very topical issue finding many applications in climate studies and operational weather forecasting. Nowadays, there are several methods which allow to perform such tasks. Visual classification methods, or in situ methods providing information on the atmospheric parameters (e.g. humidity content or local temperature), are currently used.

The methods at present most reliable are, however, those which use radiance data collected by groundbased and spaceborne sensors. For example the Radar and Light Detection and Ranging (Lidar) based on the active remote sensing technology can provide direct measurements of the vertical structure and microphysical features of clouds. They also perform an accurate atmospheric profiling with their high accuracy and an excellent space and time resolution.

On the other hand, there are the passive remote sensing imagery and sounders, which have become perhaps the main tool for the cloudy scenario analysis. They investigate the underlying atmosphere from space, thus acquiring information on the reflected, transmitted or emitted radiation by the underlying cloud systems. The range of wavelengths in which they work can be very broad: there are radiometers working at VIS/IR wavelengths, others in the ultraviolet, still others focusing on the microwave range. The data thus collected constitute the basis for the totality of operational algorithms for cloud detection and classification.

In this work the output data obtained via two methods with very different characteristics will be examined and compared. One of them will be selected among the tools exploiting the VIS/IR data acquired by the geostationary satellite sensor SEVIRI. Specifically we will deal with the Cloud Mask (CMa), Cloud Type (CT), and Cloud Top Temperature/Height (CTTH) produced by the SAFNWC software package. This kind of technology was already used by more than half a century and is especially suitable for retrieval and classification of cloud properties. Actually, clouds present a significant reflectivity at visible wavelengths if compared to that of most other surfaces and emit thermal energy in the infrared region. Thus, spatial differentiation and thresholding techniques exploiting this kind of electromagnetic radiation can be used in order to detect and classify the cloud cover.

The second method used in the comparison will be a novel algorithm named MWCC. This techinque is able to reveal the vertical development of clouds while providing useful information on cloud type and cloud top height. Generally, the MW observations are very useful to provide information on the Earth's atmosphere, due to their penetration of the clouds with respect to VIS/IR measurements. In fact, if the optical frequencies only provide a measure of radiation from the top of clouds, microwave radiation can propagate through clouds showing a better ability to sense the bulk of cloud droplets interacting with radiation field and the underlying surfaces. For this reason, microwaves show high potentialities in detecting liquid water and ice content into the clouds by enhancing the possibility to retrieve the amount of rain for their direct link with the extinguished radiation by hydrometeors.

Thus, as will be more thoroughly explained throughout the following chapters, the microwave radiation generally is not employed to detect or classify the cloudy scenarios. In the last few years, however, some focused studies revealed the potential of certain MW channels employement in order to obtain a characterization of the structure of the thunderstorm convective core. The MWCC represents one of the earliest examples.

The purpose of the present effort is an evaluation the MWCC performances with respect to the SAFNWC products. Since they are totally different from a physical point of view, it results quite interesting to quantitatively evaluate their convergences and divergences, by also investigating the technical and scientific causes. Therefore, an inter-comaprison among the output they produce will be carried out. In a first stage their power of cloud detection will be tested so as to determine whether the different technologies produce the same results in identifying cloud presence or absence. Subsequently, over the regions covered by cloud according to both

softwares, a study will be performed in order to assess the agreement extent in the cloud classification. This work may also be useful in order to test the MWCC algorithm which still has not any kind of official numerical validation. Important information for its future development can thus be derived.

2

OVERVIEW OF CLOUD DETECTION AND CLASSIFICATION METHODS

The detection and the classification of clouds has always had a number of important applications in weather and climate studies. However, the scientific investigation of clouds dates from the early nineteenth century, when the French naturalist Jean Baptiste Lamarck and the Englishman chemist Luke Howard indipendently proposed the first visual methods for cloud classification. Lamarck's work was soon forgotten, whereas the Howard's activity was much more successful. He applied the Linnean principles of natural history for a visual cloud categorization, by using the universal Latin for the nomenclature and by also emphasizing the mutability of cloud systems [*Howard* (1803)]. The four basic cloud categories he introduced were: *Stratus* or predominantly horizontally rather than vertically extended clouds; *Cumulus* or cloud further extending in height; *Cirrus* or filamentous white clouds, that he described as "parallel, flexuous, or diverging fibres, extensible in any or all directions". He combined these names to form four more cloud types, among which there was the *Nimbus* category, or the precipitating one[1].

A long time has elapsed since then, but such a scheme of distinguishing and grouping clouds perfected through the years by a large number of scientists, is the one still adopted by the World Meteorological Organization (WMO) and published in the International Cloud Atlas (1956). WMO currently recognizes 10 cloud main genera, which describe where in the sky they form and their approximate appearance:

- **Low clouds**: lying between 0 and 2000 m, among which there are *Cumulus*, *Nimbostratus*, *Stratus* and *Stratocumulus*;
- **Middle clouds**: ranging in 2000 and 7000 m, they include *Altocumulus* and *Altostratus*;
- **High clouds**: to which *Cirrus*, *Cirrostratus* and *Cirrocumulus* belong;
- **Vertically developed clouds** affecting more layers and essentially including the towering *Cumulonimbus*.

This classification scheme is summarized in figure 2.1. Moreover, these genera are further subjected to a secondary classification on the basis of shape and internal structure, and also to a tertiary one, describing the cloud transparency and arrangement. In all there are about 100 combinations.

Over the last two centuries, the cloud cover quantification and qualification performed via a visual analysis, has remained in use. An example is represented by

1 taken from http://www.rmets.org/weather-and-climate/observing/luke-howard-and-cloud-names.

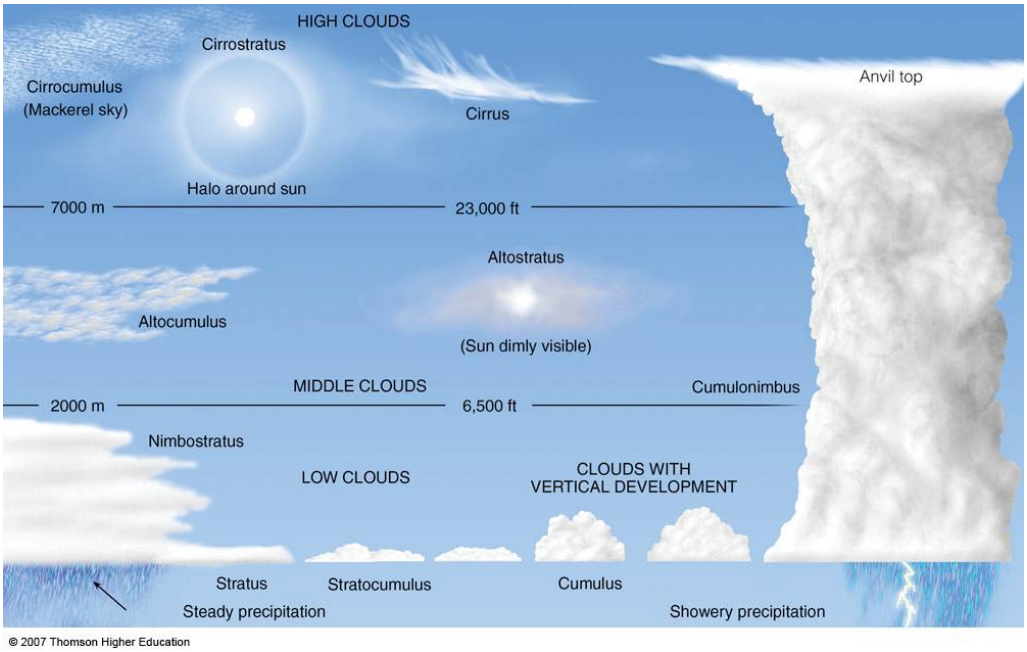

Figure 2.1: WMO official classification of the 10 main cloud genera.

the system mostly employed in aviation in order to assess the cloud cover amount. By using a convex mirror, it assimilates the overhanging portion of the sky to a circle to be divided into eight segments called *oktas*. Subsequently, according to the oktas fraction covered by cloud, the cloudy, half-cloudy, clear or the intermediate statuses are assigned[2].

Nevertheless, the cloud detection and classification methods have greatly grown up with technology advances. In particular, the real change in this research field was the beginning of the remote sensing, both *active* and *passive*:

- Active sensors transmit a pulse of electromagnetic energy to monitor the earth surface and atmosphere components. This is directed toward the target and once reflected off it returns to sensors thus providing a wide range of information. Examples of active sensor are Radar and Lidar.

- Passive sensors measure the reflected solar and the emitted radiation from the earth-atmosphere system. Equipped with spectrometers they measure signals at several spectral bands simultaneously, resulting in so-called multispectral images which allow numerous interpretations.

Remote sensing in the modern sense of the term begins after the World War II, when 25 airborne radars modified for ground meteorological use entered the forecasting practice. Just at the same time a large importance was acquired by the global scale observations and especially by the radiosounding network, which

2 more info e.g. available on http://www.metoffice.gov.uk/media/pdf/k/5/Fact_sheet_No._17.pdf and https://bmtc.moodle.com.au/mod/book/view.php?id=2171&chapterid=36

allowed a constant monitoring of the planetary situation up to 15-20 km height. Also the airborne observations became determinants in this field, starting to carry instruments suitable for meteorological studies.

Anyway, the greatest innovation in the remote sensing field came with the launch of meteorological satellites. These could cover much more land surface than planes and also monitor areas on a regular basis. The ability to derive an accurate cloud mask from satellite data under a variety of conditions has thus been a research topic since launch of the the first satellite bringing on board meteorological instruments, or the Vanguard-2 in 1959. Designed by the National Aeronautics and Space Administration (NASA), this mission was conceived to measure cloud cover distribution over the daylight portion of its orbit[3]. However, due to an unsatisfactory orientation of the spin axis the telemetry data resulted to be poor and then, the first images actually transmitted by a weather satellite, date back to year 1960, when NASA sends into orbit Television and Infrared Observation Satellite Program (TIROS) - 1. It was equipped with two vidicon cameras, at the time typically used for the television broadcast, and remained operational for 78 days[4].

Since then, several geostationary and polar-orbiting meteorological satellites were launched and the constantly developing technology of the onboard instruments allowed to acquire information pertaining to a wide electromagnetic frequency range from the ultraviolet (UV), to visible (VIS), near-infrared (NIR), infrared (IR) and MW wavelenghts. The main energy source for the earth-atmosphere system is represented by solar radiation, travelling as an electromagnetic wave extending all over electromagnetic spectrum, from the UV to IR. The incoming solar radiation is partly absorbed, partly deflected (or *scattered*) and partly reflected by the atmospheric gases, aerosols and clouds (figure 2.2). The remaining energy fraction reaching surface is almost completely absorbed and only partly reflected. After that, the absorbed radiation is re-emitted towards space at different wavelenghts. As this happens, clouds and other atmospheric gases interact again with the incident radiation and coming from various directions, further reflecting, absorbing and then emitting, or scattering. A discussion of the heat balance of the atmosphere can be found in *Wallace and Hobbs* (1979).

The solar radiation reaches its maximum in the visible (short wave radiation), whereas the earth emitted radiation has its peak in the thermal IR (long wave radiation) as illustrated in figure 2.3. The first sensors built and put side by side to the vidicon cameras were able to work in the visible frequencies and to acquire radiances reflected from the underlying surfaces. Actually clouds have a high solar reflectivity in the visible compared to that of most surface features as shown in figure 2.4. Thus, spatial differentiation and thresholding techniques could be used to distinguish clouds from less reflective land and ocean surfaces. Then to the simple visible sensors the infrared channels were added in order to characterize the cloud coverage on the basis of cloud emitted radiation. IR brightness temperatures can

3 http://nssdc.gsfc.nasa.gov/nmc/spacecraftDisplay.do?id=1959-001A.
4 http://science.nasa.gov/missions/tiros/.

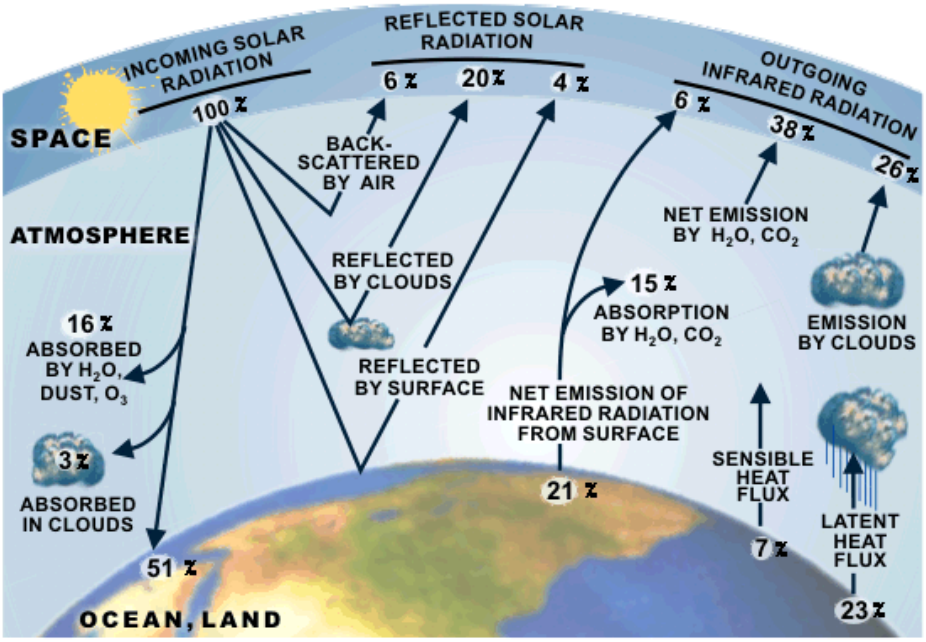

Figure 2.2: Radiative balance of the Earth: the incoming solar radiation is partly absorbed, partly scattered and partly reflected by the atmospheric gases, aerosols, clouds and Earth surface. A fraction of the absorbed radiation is re-emitted in the thermal bands. Note that the percentages of each kind of radiation are shown too. Image available online at http://www.thermopedia.com/content/569/#ATMOSPHERE_FIG2.

be used as a proxy for the surface or cloud top temperatures, which under normal lapse rate conditions, decrease with height. Therefore when the emitted radiance is converted to equivalent blackbody temperature it can be used to distinguish the presence of opaque clouds from a warm surface.

For example, the National Oceanic and Atmospheric Administration (NOAA) Scanning Radiometer (SR), put into operation in 1970, measured reflected radiation from the earth-atmosphere system in the 0.52 - 0.73 μm (VIS) band during the day and the emitted radiation in the 10.5 - 12.5 μm (IR) band during the day and night[5]. It was put side by side with vidicon cameras, but unlike a camera, it formed an image by using a continuously rotating mirror which acquired radiances coming from below. *Rossow et al.* (1983) used the SR imagery in order to derive the cloud amount, optical thickness and cloud top temperature in a pilot programme aimed to develop a cloud climatology.

The SR successor was the Advanced Very High Resolution Radiometer (AVHRR)/2 aboard the NOAA polar orbiting satellites. It gave daily global coverage in 5 spectral bands ranging from 0.58 - 12.5 μm (the latest and improved instrument version, AVHRR/3, is still operating and is equipped with 6 spectral channels). Several attempts were made over the years in order to establish AVHRR data processing

5 http://nssdc.gsfc.nasa.gov/nmc/experimentDisplay.do?id=1970-106A-03.

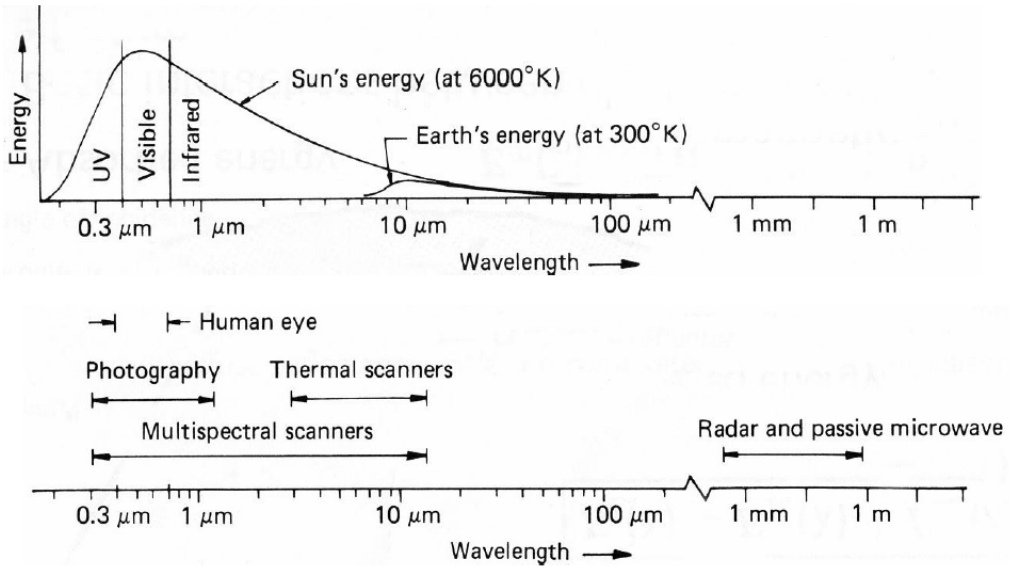

Figure 2.3: Solar and Earth black body radiation emission curves. In the lower panel also the instrumentation sensitivity to the different kind of radiation is highlighted. Taken from *Menzel* (2012).

schemes able to provide an accurate cloud cover estimation and sometimes also a cloud type analysis [e.g *Liljas* (1984) or *Arking and Childs* (1985)]. Some of these techniques for example considered the spatial variance of infrared radiances to separate the clear or cloudy scenes [*Coakley and Bretherton* (1982)]. However, the first algorithm making use of all 5 the AVHRR spectral channels was AVHRR Processing scheme over cLouds, Land and Oceans (APOLLO). After deriving some physical properties, it processed each pixel of the imagery, to which a label was assigned according to whether its radiance was lower or higher than the given threshold.

In other words, the first stage of the APOLLO software processing scheme is to generate a cloud mask product via a set of threshold tests, distinguishing four categories (cloud free, fully cloudy, partially cloudy, and snow/ice) [*Saunders and Kriebel* (1988)]. Subsequently the cloud cover is derived for each fully cloudy or partially cloudy pixel, according to two different methodologies. In particular each fully cloudy pixel is checked for the presence of thin or thick cloud, based on the VIS relectances during the day and on the IR brightness temperatures during night-time [*Kriebel et al.* (1989)]. Pixels covered by thick clouds are considered water cloud filled, whereas thin clouds are treated as ice clouds, i.e. cirrus. In case of partially cloudy pixels the cloud coverage is obtained through the reflectances and temperatures of the cloudy and cloud-free portion of the pixels. These quantities are taken from the nearest fully cloudy and cloud-free pixels, assuming horizontal homogeneity. The cloud cover of the partially cloudy pixels is assigned to the most frequent cloud type in a 50 by 50 pixels environment. Finally cloud optical depth, liquid/ice water path and emissivity are derived during daytime for every fully cloudy pixels by means of parameterization schemes based on the VIS reflectance, whereas the cloud top

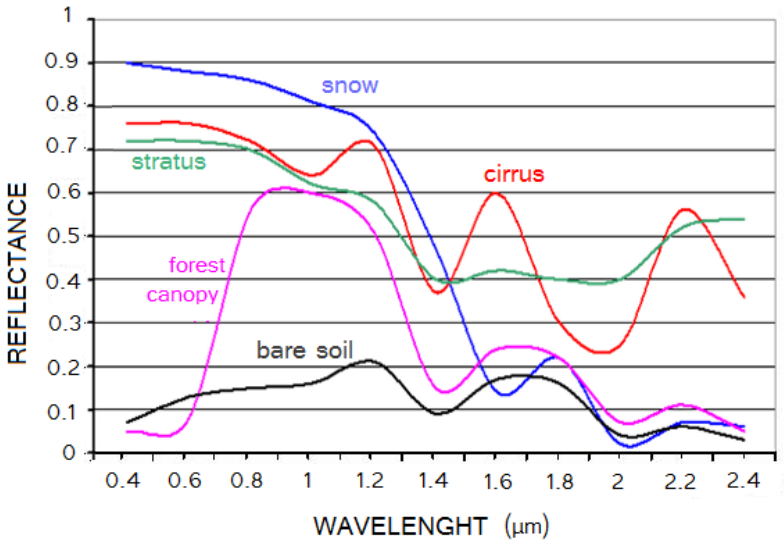

Figure 2.4: Typical reflectance values for a series of different surfaces as a function of wavelength, taken from *Jedlovec* (2009).

temperature is obtained by means of a correction for the water vapour above the cloud [*Kriebel et al.* (2003)].

Later on, other operational algorithms partly referred to APOLLO were developed [e.g. *Stowe et al.* (1991), *Derrien* (1993)]. An example was an automated cloud classification model based on NOAA/AVHRR satellite data, named SMHI Cloud ANalysis model using DIgital AVHRR data (SCANDIA). The SCANDIA first version was implemented in 1988 [*Karlsson* (1989)] and it operated exclusively on Sweden and adjacent areas. SCANDIA made use of imagery from all 5 AVHRR/2 channels at maximum horizontal resolution (at nadir 1.1 km) and it was based on a series of threshold tests performed on the acquired brightness temperatures or reflectances differences [*Karlsson and Liljas* (1990)].

However these methodologies based on the exploitation of the AVHRR polar sensors did not ensure the adequate space-time coverage requested for a regular monitoring of the cloudy scenarios. This could be provided by continuos framing of the geostationary satellites, able to observe a large portion of Earth surface. So, the first of the Geostationary Operational Environmental Satellites (GOES), was launched in October 1975. Two more followed, in June 1977 and 1978 respectively. Such satellites were spin stabilized spacecraft, which provided imagery through the Visible Infrared Spin-Scan Radiometer (VISSR). The instrument, by using a common optical system, acquired information both in a VIS and an IR spectral band[6]. Besides in November 1977, the first among the geostationary meteorological satellites of the Meteosat programme was launched too. It provided Earth and atmosphere images every half-hour in three spectral channels via the Meteosat Visible and Infrared Imager (MVIRI) instrument. In addition to acquiring information in the VIS/IR range, this is one of the very first cases in which a channel centered in an IR water vapour

6 http://nssdc.gsfc.nasa.gov/nmc/experimentDisplay.do?id=1977-048A-01.

absorption band was used. It was more sensitive to the water vapour variations furthemore providing important data about the water vapour amount.

After that, a series of new automatic methods for cloud detection and classification using the operational analysis of geostationary satellite data, were thus developed. In literature, in addition to thethreshold techniques [*Minnis and Harrison* (1984); *Rossow et al.* (1985)] also some statistical methods appeared. These classified a pixel as belonging to a specific cloud class, by costructing frequency histograms considering the image as a whole and then evaluating the position of such pixel in the feature space [*Desbois et al.* (1982); *Simmer et al.* (1982); *Porcù and Levizzani* (1992)].

These experiments clearly surfaced the need for an increasing number of spectral channels. Many authors pointed out that such additional information could improve the cloud detection and differentiation quality [e.g. *Desbois et al.* (1982); *Coakley* (1983)]. Some of them have especially focused on the high-altitude cirrus cloud distinction, wich in general resulted quite difficult owing to contamination of the IR frequency signal by the underlying layers (lower clouds or surface) [*Inoue* (1985); *Jin and Rossow* (1997)].

The last twenty years have seen great progresses in this direction. The latest technology, in fact, allowed to increase the multispectral capabilities of the new generation of VIS/IR imager. Among them, in addition to improved version of the instruments belonging to the previous releases (e.g. AVHRR and GOES), the Moderate Resolution Imaging Spectroradiometer (MODIS) must be mentioned. The instrument was launched into Earth orbit by NASA on board the *Terra* (1999) and *Aqua* (2002) satellites belonging to the Earth Observing System (EOS)[7] programme. The instruments make measurements in 36 spectral bands ranging in wavelength from 0.4 to 14.4 μm and at varying spatial resolutions (250, 500 and 1 m). They are designed to provide measurements of large-scale global dynamics including changes in Earth's cloud cover, radiation budget and processes occurring in the oceans, land and lower troposphere [*Ackerman et al.* (1998); *Frey et al.* (2008)]. The MODIS operational cloud products consist of cloud mask, cloud top properties (i.e. temperature, pressure, effective emissivity), cloud thermodynamic phase, cloud optical thickness and microphysical properties. The cloud mask algorithm identifies several conceptual domains according to the kind of surface and solar illumination. After that a series of threshold tests attempt to detect the presence of clouds, returning also a confidence level that the pixel is clear, ranging in value from one (high confidence clear) to zero (low confidence clear). The four confidence levels thus included in the output are: confident clear, probably clear, uncertain/probably cloudy and not clear/cloudy [*Platnick et al.* (2003)].

A turning point was also constituted by the Meteosat Second Generation (MSG) geostationary satellites carrying on board the SEVIRI. With its 12 spectral channels and a high spatial and temporal resolution, the observations thus provided have shown large improvements in the cloud property retrieval. The data thus collected are now processed through a wide variety operational tools, including the most

7 http://eospso.nasa.gov/mission-category/3

advanced SAFNWC software package. This topic is throughly illustrated in section 3.1.

While the VIS/IR sensors was developing, the weather satellites began to be also equipped with passive MW sensors.

Electromagnetic radiation in the reange of microwave wavelenghts is characterized by a mechanism of interaction with matter different than other spectral regions. Microwave radiation emission from an object is strongly tied to the physical properties of the object itself, such as atomic composition and crystalline structure. Contrarily to the IR spectral region where the black body approximation often well describes the real behaviour of the emitters, the microwave emitters surfaces must be considered as a grey body with an emissivity value typically lower than 1.

The great advantage of these frequencies with respect to the optical ones is the high capability to penetrate the majority of clouds [e.g., *Greenwald and Cristopher* (2002); *Burns et al.* (1997)]. Moreover, contrarily to VIS/IR observations, which only sense reflected or emitted radiation from the cloud top, microwave radiation can propagate through clouds, showing sensitivity to the total cloud layer in addition to the potential to estimate cloud water and ice contents (see section 3.2).

For this reason, since the introduction of the first radiometers able to capture this kind of long wave radiation, the data acquired were not used for cloud detection or classification, but rather to obtain information about the water vapour atmospheric column or about the underlying surfaces.

For example, spaceborne MW observation were obtained by the the Special Sensor Microwave/Imager (SSM/I), a 7 channels, four-frequency, linearly polarized passive microwave radiometer system on board the Defense Meteorological Satellite Program (DMSP) satellite. It measured surface and atmospheric microwave brightness temperatures at 19.35, 22.235, 37.0 and 85.5 GHz and it has been a very successful instrument. Its combination of constant-angle rotary-scanning and total power radiometer design has become standard for passive microwave imagers, e.g. Advanced Microwave Scanning Radiometer (AMSR). Over ocean, cloud liquid water paths were routinely estimated from the cloud emissions measured between 19 and 85 GHz by such a kind of imagers [e.g. *Greenwald et al.* (1993); *Ferraro et al.* (1996); *ODell et al.* (2008)]. Moreover, due to the strong contamination of the surface type (different emissivity) on microwaves measurements, over land the problem was more complicated. The land surface emissivity generally ranges between 0.6 and 1, making atmospheric features difficult to identify against such a background because of the limited contrast. In addition, the land surface emissivity is variable in space and time and difficult to model. Efforts have been made to estimate cloud liquid water over land, using a priori information on the surface properties [*Aires et al.* (2001)].

At frequencies below 80 GHz, the microwave signal is essentially dominated by emission and absorption by cloud droplets and rain and is little affected by the presence of ice. At higher frequencies, the scattering effect on frozen particles increases. Ice particles modify the upwelling radiation by scattering photons away from the satellite sensors, causing a brightness temperature depression. Then, from

observations above 80 GHz, cloud ice information has been extracted from both imagers such as SSM/I and water vapour sounders such as the AMSU-B, a passive microwave sounder on board the NOAA polar orbiting satellites, operationally used to estimate temperature and water vapour atmospheric profiles [*Greenwald and Cristopher* (2002); *Hong et al.* (2005a); *Weng et al.* (2003)], as will be throughly explained in section 3.2.

Therefore, the physical properties of microwaves have been fully exploited in the weather analysis, albeit only in recent years they begun to be employed for detecting or classifying clouds. A criterion based on the difference between measured brightness temperatures at the three AMSU-B channels centered in the MW water vapour absorption band (183.31 GHz) was suggested in order to screen out convective clouds by *Burns et al.* (1997). The same channels have also been used for the production of information about the convective core of the tropical cyclons [*Hong et al.* (2005a)].

In 2011, *Aires et al.* tried a statistical cloud classification and cloud mask algorithm on the basis of AMSU-B observations, by using the VIS/IR data from SEVIRI in order to train the microwave classifier. They obtained in this way a confidence level of more than 80%,

In the last few years, a multichannel passive microwave cloud classification algorithm has been developed in the context of the rain rate retrieval algorithm Water vapour Strong Lines at 183 GHz (183-WSL) [*Laviola and Levizzani* (2011); *Laviola et al.* (2013)]. It is able to detect and also to classify the mid-latitude clouds and also to give important information about the deep convection vertical development, by using the brightness temperatures of the three MW water vapour opaque channels (see subsection 3.2.2).

In the present work we propose to understand differences and errors that may take place by using two indipendent methods for cloud detection and classification based on different physical features. One of them will be chosen among the VIS/IR-based software packages, the other one instead will be an algorithm working in the MW frequencies. Although both, in principle, are intended to provide the same kind of output, as based on different physical principles they should sometimes "see" different cloud properties. What we intend to do, is to quantitatively evaluate their deviation, trying to explain the technical and phenomenological causes.

3

TOOLS AND METHODS

The basic purpose of this research work, as already discussed in the previous chapters, is to assess the differences between two methods for cloud detection and cloudy scenario classification. The two methods are based on satellite data from different parts of the electromagnetic spectrum, one in the MW and the other in the VIS/IR wavelengths. What we intend to do, is to quantitatively evaluate their differences and to explain the technical and phenomenological causes.

Thus, the first part of this chapter describes the characteristics of the two classification algorithms, by focusing on their different scientific basis, the output they produce, and the satellite sensors whose data are used as input.

Whereupon, a threshold test based on the brightness temperature difference (BTD) between SEVIRI data acquired in the water vapour absorption band centered at 6.2 μm and in the IR atmospheric window at 10.8 μm (i.e. where atmospheric absorption/emission is negligible) is illustrated. It will be employed in the following analysis as a first investigation method in order to verify the severity and vertical extent of each analysed cloud system.

Afterwards, a brief description of *dichotomous statistics* will follow, used as a tool for the quantification of the differences between the two cloud classification algorithms.

3.1 VIS/IR DATA ACQUISITION AND PROCESSING

This section illustrates the characteristics of the SEVIRI instrument on board the MSG satellites and the SAFNWC software package. This latter together with SEVIRI data are exploited in this study for the cloudy scenario analysis in the VIS/IR spectral range.

3.1.1 *SEVIRI instrument*

The MSG consists of a series of four geostationary satellites in a circular orbit at about 36000 km above the equator with the same Earth's angular rotation speed. The monitoring service is currently provided by MSG-3, the prime operational geostationary satellite positioned at 0 degrees and providing full disc imagery every 15 minutes. MSG-2 is exploited for the Rapid Scanning Service, delivering more frequent images every five minutes over parts of Europe, Africa and adjacent seas, whereas MSG-1 presently serves as back-up to both sensors. The last satellite of the MSG series, MSG-4, was launched on July 2015. The current policy is to keep two

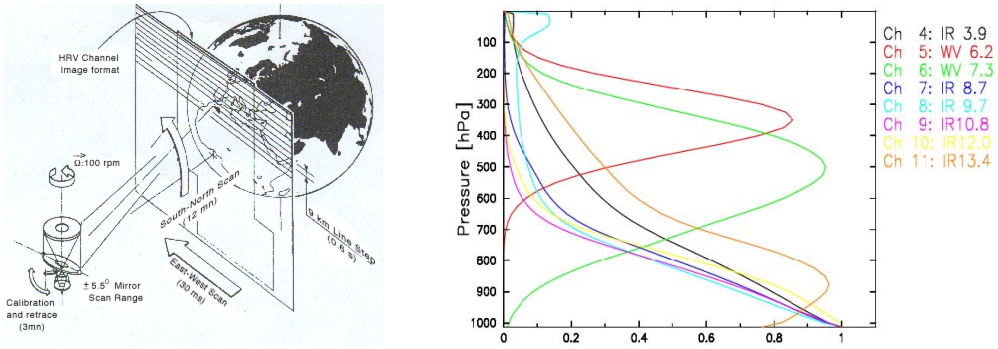

(a) (b)

Figure 3.1: (a) Scanning system of SEVIRI; (b) Weighting functions for SEVIRI channels 4-11 (from http://eumetrain.org/data/2/204/204.pdf).

operational satellites in orbit and to launch a new satellite close to the date when the fuel on the oldest of the two starts to run out[1].

The main MSG payload is SEVIRI, a 12-channel imager observing the earth-atmosphere system. It provides detailed information due to an imaging-repeat cycle of 15 minutes and image sampling distance of 3 km at nadir for all channels, except the high-resolution visible (HRV) at 1 km. For the first 11 channels a full SEVIRI image consists of 3712×3712 pixels and is acquired in about 12 minutes by combining satellite spin and rotation of the scan mirror. This phase is followed by a brief calibration of the thermal infrared channels, after which the scanning mirror returns to its initial position, by obtaining in this way the repeat cycle of 15 minutes [*Schmetz et al.* (2002)]. Such acquisition mechanism proceeds from east to west and from south to north, as shown in figure 3.1(a).

The 12 channels of SEVIRI are centred at frequencies covering the portion of electromagnetic spectrum ranging from visible to infrared. The weighting functions displayed in figure 3.1(b) and the spectral channels illustrated in table 3.1, demonstrate that each channel has been selected in order to gather information on the major atmospheric constituents, the earth's surface and the cloud cover.

3.1.2 *SAFNWC software package*

The software package developed by SAFNWC includes 12 Product Generator Elements (PGEs), i.e. softwares for the retrieval of variuos cloud analysis products from SEVIRI data. The PGEs can generate products over a user-defined area within the full disk, thus providing useful information for nowcasting applications.

For the data analysis carried out in the following, only three PGEs have been used, i.e. PGE01 providing the Cloud Mask (CMa) product, PGE02 for the Cloud

1 more info available on https://directory.eoportal.org/web/eoportal/satellite-missions/m/meteosat-second-generation.

Table 3.1: *SEVIRI channels.*

Channel Number		Characteristics of spectral band (μm)			Main gaseous absorber or window	Main observational application
		λ_{cen}	λ_{min}	λ_{max}		
1	VIS0.6	0.635	0.56	0.71	Window	Surface, clouds, wind fields
2	VIS0.8	0.81	0.74	0.88	Window	Surface, clouds, wind fields
3	NIR1.6	1.64	1.50	1.78	Window	Surface, cloud phase
4	IR3.9	3.90	3.48	4.36	Window	Surface, clouds, wind fields
5	WV6.2	6.25	5.35	7.15	Water vapour	Water vapour, high level clouds, upper air analysis
6	WV7.3	7.35	6.85	7.85	Water vapour	Water vapour, atmospheric instability, upper-level dynamics
7	IR8.7	8.70	8.30	9.10	Window	Surface, clouds, atmospheric instability
8	IR9.7	9.66	9.38	9.94	Ozone	Ozone
9	IR10.8	10.80	9.80	11.80	Window	Surface, clouds, wind fields, atmospheric instability
10	IR12.0	12.00	11.00	13.00	Window	Surface, clouds, wind fields, atmospheric instability
11	IR13.4	13.40	12.40	14.40	Carbon dioxide	Cirrus cloud height, atmospheric instability
12	HRV	Broadband (about 0.4 – 1.1)			Window/water vapour	Surface, clouds

Type (CT) and Cloud Phase extraction, and, finally the PGE03 generating the Cloud Top Temperature/Height (CTTH) information.

The first two products provide, respectively, a cloud detection and classification and are performed via a multispectral thresholding technique [*Derrien and Le Gléau* (2005)]. With regard to the computation of cloud top height, instead, the technique depends on the cloud type as available in the CT product [*Derrien* (2013)]. For example in case of opaque clouds, the CTTH values can be deduced from the brightness temperature (BT) acquired in the IR window channels. This technique cannot be applied in presence of semitransparent or fractional clouds, mainly due to contamination of the BTs in the IR frequencies by the underlying surface. Therefore, a multispectral approach is needed.

The software works also in case only a limited number of channels are available. Actually, even if the optional information enables to perform a more accurate analysis, the CMa and CT algorithms mandatory input are the BTs acquired at 3.9, 10.8 and 12.0 μm, in addition to the radiance at 0.6 μm. The CTTH module needs the IR10.8 channel information and at least one among the 6.2, 7.3 and 13.4 μm radiances.

Most thresholds and coefficients are computed from ancillary data and radiative transfer models, by obtaining in this way values specifically computed for any

Table 3.2: *PGE01 output description: Cloud Mask.*

CMa classes	Description
Non-processed	containing no data or corrupted data
Cloud-free	no contamination by snow/ice covered surface, no contamination by clouds; contamination by thin aerosol (dust clouds or volcanic plume) remains possible
Cloud contaminated	partly cloudy or semi-transparent; may also include dust clouds or volcanic plumes
Cloud filled	opaque clouds completely filling the FOV; may also include thick dust clouds or volcanic plumes
Undefined	has been processed but not classified due to known separability problems

time and geographical area selected by the user. Ancillary data mainly consists of atlas, climatology maps and Numerical Weather Prediction (NWP) model forecast fields, supplied by European Centre for Medium-Range Weather Forecasts (ECMWF) on specific user request. The Second Simulation of a Satellite Signal in the Solar Spectrum (6S) advanced code [*Tanre et al.* (1990); *Kotchenova et al.* (2006)] is exploited to simulate the atmospheric effects in the solar bands and for the pre-computation of a great variety of parameters (e.g., angles, water vapour and ozone content).

On the other hand, among the fast radiative transfer model employed there is also the Rapid Transmissions for TOVs (RTTOV) [*Eyre* (1991); *Saunders et al.* (1999)]. It works in the thermal bands and is applied to radio-soundings from a data set provided by ECMWF [*Chevallier* (1999)] in order to compute the look-up tables subsequently used for the threshold calculations. In the CTTH module context, the RTTOV is also applied using NWP temperature and humidity vertical profile to simulate 6.2, 7.3, 10.8, 12.0 and 13.4 μm cloud free and overcast radiances and brightness temperatures[2]. This process is performed online on each segment of the processed image.

The overall operational strategy of the SAFNWC software package involves, as a first step, the detection of clouds by the CMa software. It delineates all absolutely cloud free pixels in a satellite scene with a high degree of confidence and identifies pixels that are contaminated by either clouds, dust or snow/sea ice. Whereupon, each pixel classified as cloudy is distinguished per type using the CT module, which is also able to produce a further output concerning the cloud particle phase (CT_PHASE). Only after these two steps, the application of the third module, CTTH, provides information about cloud top temperature or, in an equivalent way, height or pressure.

2 source http://www.nwcsaf.org/HD/MainNS.jsp.

Table 3.3: *PGE02 output description: Cloud Type.*

CT classes	Description
Non-processed	containing no data or corrupted data
Cloud free land/sea	no contamination by clouds or snow/ice covered surface; contamination by thin aerosol (dust cloud or volcanic plume) possible
Land/sea contaminated by snow/ice	land contaminated by snow or sea contaminated by snow/ice
Very low clouds	include fog, used for all very low clouds (< 2 km)
Low clouds	used for all low clouds (2 - 3.6 km)
Medium clouds	used for all medium level clouds (3.6 – 6.3 km)
High opaque clouds	used for all high opaque clouds (6.3 – 9 km)
Very high opaque clouds	used for all very high opaque clouds (> 9 km)
High semi-transparent thin cirrus	used for all the thinner high semi-transparent clouds
High semi-transparent meanly thick cirrus	used for all the meanly thick high semi-transparent clouds
High semi-transparent thick cirrus	used for all the thicker high semi-transparent clouds
High semi-transparent cirrus above low or medium clouds	distinguished from fractional cover or mid-level clouds only in daytime illumination condition
Fractional clouds	sub-pixel water clouds (including cloud edges)
Undefined	undefined by CMa

Finally, on all the mentioned products a parallax correction is applied by means of a dedicated tool included in the software package.

The output content of PGE01 and PGE02 (both cloud type and cloud particles phase) is illustrated in tables 3.2, 3.3 and 3.4, respectively[3].

In table 3.3 it can be observed that, by using PGE02, it is also possible to make a distinction between high semi-transparent (cirrus) clouds and high or very high opaque clouds. Moreover, for medium to low and high opaque cloud classes, a rough

3 available at ftp://iacftp.ethz.ch/pub_read/giuntai/SAF-NWC-CDOP-INM-SW-ICD-3_v6.0.pdf.

Table 3.4: *PGE02 output description: Cloud Phase.*

CT_PHASE classes
Non-processed (containing no data or corrupted data)
Water cloud
Ice cloud
Undefined (due to known separability problems)

evaluation of the range of clouds top heights, obtained by analysing statistics of retrieved cloud top pressure, is provided [*Derrien* (2013)].

A quality flag is associated to each products, describing, among other things, illumination conditions and quality of the processing itself.

As regards the illumination parameter we can distinguish: *night-time* (solar elevation <-3°), *twilight* (-3°< solar elevation <10°), *daytime* (10°< solar elevation) and *sunglint* (Ref_{Cox}>10% [4], solar elevation >15°) .

On the other hand, the quality flag provides an indication of the confidence attributable to the retrieval processes and its possible values are:

0 *Non-processed*: containing no data or corrupted data;

1 *Good quality*: high confidence;

2 *Poor quality*: low confidence;

3 *Reclassified*: (after spatial smoothing) very low confidence [5].

For CMa and CT products a pixel is flagged as of low confidence if for each executed test the difference between the threshold value and the mesurements is lower than a specified tolerance value depeding on the test itself. In the CTTH retrieval, however, the quality assessment is conditioned by the cloud type and the used retrieval techniques [more info are available in *Derrien* (2013)].

3.2 MW DATA ACQUISITION AND PROCESSING

This section contains technical and physical information on the AMSU-B/MHS radiometers and on the MWCC algorithm, respectively used for data acquisition and processing in the MW frequencies for cloud type characterization.

4 Ref_{Cox} stands for the top of atmosphere reflectance at 0.6 μm simulated over the ocean using the Cox and Munck theory [*Cox and Munck* (1954)].

5 flag number 3 is available only for CMa and CT products, not for CTTH.

3.2.1 *AMSU-B/MHS instrument*

The AMSU-B is a five-channel microwave radiometer, whose main purpose is the retrieval of global data on water vapour profiles. It works combined with the fifteen-channel AMSU-A, to provide a 20 channel microwave radiometer. Both sensors are installed on board the Meteorological Operational satellite programme (MetOp) and NOAA - K, L, M polar-orbiting satellite series flying in sun-synchronous orbit. For NOAA-18 (NOAA - N) satellite, AMSU-B was replaced by the new generation radiometer MHS with basically similar characteristics of its predecessor.

The AMSU-B/MHS instrument is cross-track scanning, so it acquires continuously scene radiances at each channel frequency in a *whisk broom* mode, as illustrated in figure 3.2. During each 8-second observation cycle, it makes 3 scans of 90 observations each, with a spacing of 1.1° [NOAA (2009)]. Further information on the spatial resolution of the instrument is given in table 3.5 [*Saunders et al.* (1995); *Bennartz et al.* (2002)].

Table 3.5: *AMSU-B/MHS instrument characteristics.*

Spatial resolution	1.1°
Total viewing angle	± 48.95°
Nadir effective field of view	20 × 16 km^2
Scan edge effective field of view	64 × 52 km^2

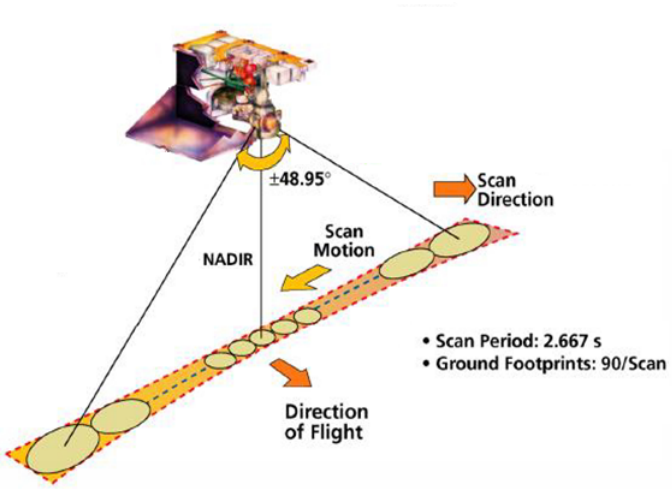

Figure 3.2: AMSU-B/MHS scan geometry.

The instrument works within a wide frequency range, from 89 to 190 GHz: two of its channels are nominally centred in the atmospheric window frequencies 89 and 150 GHz, whereas the other three are selected within the water vapour absorption band at 183.31 GHz (see table 3.6) and hereafter defined as the 184, 186 and 190 GHz channels.

Table 3.6: *AMSU-B/MHS channels.*

Channel number	Central Frequency (GHz)	Main gaseous absorber or window	Main observational application
16	89 ± 0.9	Window	Rain rate, ice water path, snow cover, snow water equivalent
17	150 ± 0.9 (157 MHS)	Window	Rain rate, ice water path
18	183.31 ± 1.0	Water vapour	Rain rate, profiling of atmospheric moisture
19	183.31 ± 3.0	Water vapour	Rain rate, profiling of atmospheric moisture
20	183.31 ± 7.0 (190.3 MHS)	Water vapour	Rain rate, profiling of atmospheric moisture

The two window channels, 16 and 17, as such, can sense through the lower atmosphere, as can also be observed by looking at the respective weighting functions peaks, shown in figure 3.3. According to *Hong et al.* (2005b), even in the case of deep convection the surface emissivity greatly influences the channel at 89 GHz and, even if to a lesser extent, that at 150 GHz . This ability to see the lower layers makes them greatly affected by the kind of background and, thus, not very useful in precipitation retrieval or in medium-high cloud observations.

The other three channels, instead, being selected in a water vapour absorption band, were originally designed and dedicated to the profiling of the atmospheric moisture [*Wang and Chang* (1990); *Wilheit* (1990)]. However, several studies on the effects of clouds on microwave radiances at the AMSU-B/MHS channels, performed through observations [e.g., *Wang et al.* (1997); *Hong et al.* (2005b)] and simulations [e.g., *Muller et al.* (1994); *Burns et al.* (1997); *Bennartz and Bauer* (2003)], have demonstrated that these three channels are very sensitive to ice crystals and rain drops. So, the combination of scattering by the former and absorption by the latter, largely contribute to radiation extinction.

On the other hand, due to their weighting functions peaking between 2 and 8 km altitude (figure 3.3), low level-clouds and surface emissivity have little effects on the signal detected within these wavelengths [*Hong et al.* (2005b)]. This means having at the same time the advantage of probing successfully over any surfaces, but also the disadvantage while observing clouds lying within lower atmospheric layers, which are virtually undetectable.

Moreover for such opaque channels, in the presence of hydrometeors in the upper level of vertically developed clouds, the farther is the frequency from the centre of the water vapour absorbtion band, the larger is the brightness temperature depression [*Burns et al.* (1997)]. In other words, the 190 GHz frequency displays the greatest signal extintion, followed by the 186 and 184 GHz. This happens because their

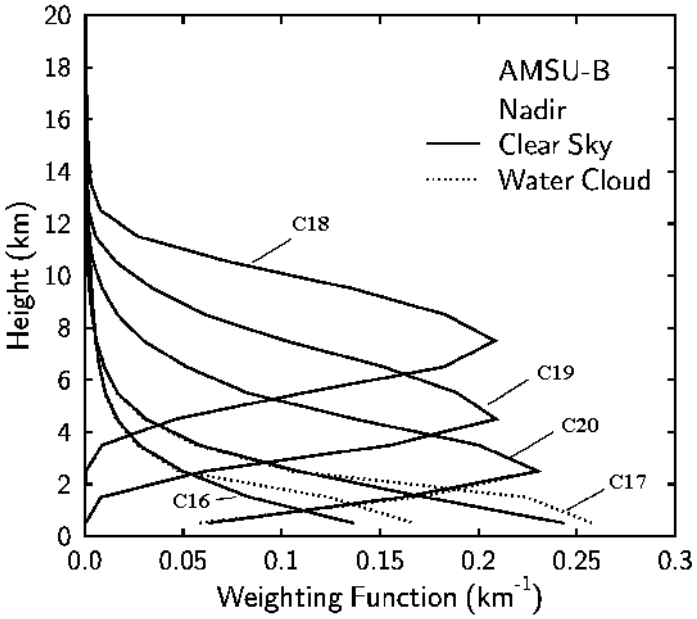

Figure 3.3: AMSU-B/MHS five channels weighting functions. The peaks heights, described in the above figure, change critically in the presence of a cloud system or of a great amount of water vapour.

weighting functions reach their maximum at different altitudes, and the more distant channel (190 GHz) can see deeper through clouds than the others, as illustrated in figure 3.3.

From sensitivity studies by *Hong et al.* (2005b) for deep convection in the Tropics, it appears also that the 190 GHz channel, as well as being the one that can see deeper inside the convective core, is also the one that has the strongest sensitivity to the frozen hydrometeor scattering and the channel within which there is the strongest incident radiation absorbtion by water vapour inside or surrounding clouds.

Therefore, for the 183.31 GHz AMSU-B/MHS channels, the magnitude of signal extinction depends both on the height of the scattering hydrometeors and on the channel wavelengths.

3.2.2 *MWCC algorithm*

All the physical features outlined in subsection 3.2.1, suggest the potential to delineate a vertical structure of deep convective systems by using the three water vapour channels centred at 183.31 GHz, as already shown by *Hong et al.* (2005a) in their analysis on the tropical systems.

Along the same lines as the aforementioned work, a new method has been studied to detect and classify the mid-latitude clouds and to give more information about the cloud vertical development, by using the brightness temperatures of these three opaque channels. Such method for the MicroWave Cloud-type Classification (MWCC) has been developed in the context of the rain rate retrieval algorithm

183-WSL [*Laviola and Levizzani* (2011); *Laviola et al.* (2013)], acquiring, subsequently, an its own identity while still being finalized.

It works by calculating the differences between the brightness temperature observed on a clear sky pixel and brightness temperatures recorded in the three 183 GHz frequencies. Thus on the basis of the signal perturbations, it performs a series of threshold tests selected by means of statistical analysis on several events particularly occurring in mid-latitudes.

Through the use of the MWCC, it is possible to detect the presence of clouds and to evaluate a cloud type in terms of stratiform (ST) and convective (CO) clouds by identifying three intensity classes for each type and evaluating the cloud top height.

As illustrated in table 3.7, to each class a range of heights is associated: in some cases this definition bands are rather wide and in some others these are overlapped. All of this is due to the principle on which the algorithm works, since it assigns each class based on the height of the weighting functions peak, but, in the presence of clouds or high concentrations of water vapour, these heights vary. Therefore, the MWCC is able to give a response with respect to one atmospheric layer within which the cloud top is located, rather than an exact height value.

MWCC	Height range
ST1	1 ÷ 2 km
ST2	2 ÷ 4 km
ST3	4 ÷ 5 km
CO1	4 ÷ 6 km
CO2	6 ÷ 8-10 km
CO3	> 8 km

Table 3.7: *MWCC classes in terms of cloud top height.*

The algorithm has been designed in order to provide information on the vertical development of clouds in particular for convective type. Thus, starting from the identification of signal perturbation of clouds in the lower atmosphere, the MWCC method tries to identify further perturbations in the middle and higher atmosphere by assuming in a bottom-up mode the vertical continuity of cloud development. This process, if on one hand well describes stratiform and convective clouds (the continuity is guaranteed by the cloud development from the surface to the top of atmosphere) on the other is unable to represent the "isolated" clouds, such altostratus due the convection dissolution.

Recently, the computational scheme of the MWCC has been improved with a probability-based module for hail detection. It is still under revision and it aims to classify the hail by size in Hail Storm Large (HSL) and Hail Storm EXtra Large (HSXL).

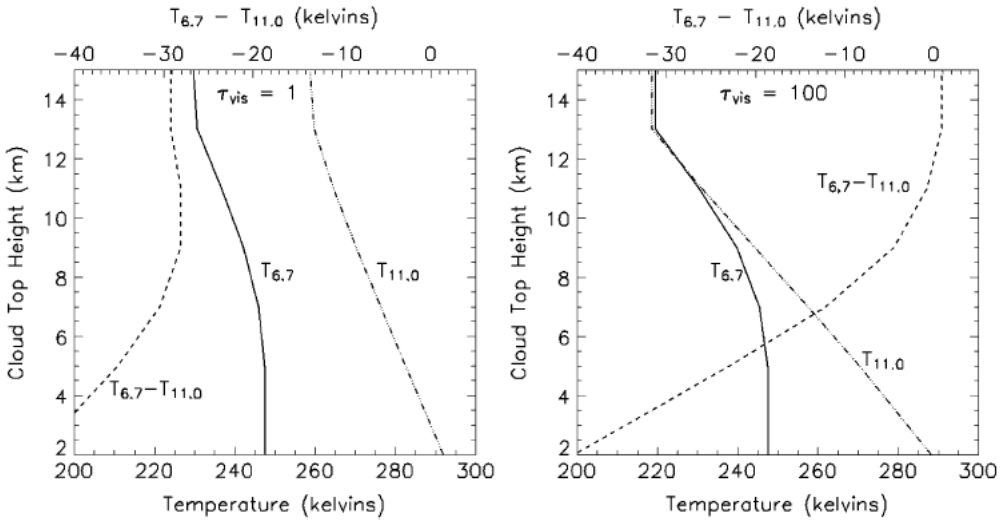

Figure 3.4: Nadir simulation of MODIS 11 μm IR window channel and 6.7 μm water vapour absorption bands for (a) optically thin and (b) optically thick clouds, illustrating their combined utility in the flagging of high-altitude, optically thick cloud structures [from *Turk and Miller* (2005)].

3.3 BRIGHTNESS TEMPERATURE DIFFERENCE TEST

In order to identify deep convection among the cloud systems in every case studies analysed, an IR threshold test was exploited. This is based on the difference between the brightness temperatures (BTD) available in the SEVIRI channel centred in the water vapour absorption band at 6.2 μm ($BT_{6.2}$) and the brightness temperatures acquired in the channel residing in the infrared atmospheric window at 10.8 μm ($BT_{10.8}$):

$$BTD = BT_{6.2} - BT_{10.8} \tag{3.1}$$

This pure infrared (and hence day/night indipendent) technique is able to detect deep convective clouds and convective overshooting, as proposed by *Schmetz et al.* (1997), and also to identify optically thick high altitude clouds, as suggested by *Turk and Miller* (2005).

With the aim of better understanding the functioning of this test, we refer to the figure 3.4. This shows some radiative transfer simulations for BT as a function of cloud top height, involving the two MODIS channels at 6.7 and 11.0 μm, corresponding to the SEVIRI channels WV6.2 and IR10.8 respectively. Plotted in both panels are three curves depicting the variations of the BTs and their difference in two cases, for which peculiar behaviours emerge:

- *Optically thin cloud* (left-hand panel): the 6.7 μm signal has no sensitivity to clouds below about 5 km and the 11.0 μm signal gradually decreases as the top height increases. Due to transparency of outermost layers of this cloud kind, the measured temperature does not correspond to the environmental

cloud-top temperature, but it is much higher in both bands, in this way the BTD never exceeds - 28 K for any cloud height.

- *Optically thick cloud* (right-hand panel): the 6.7 μm channel continues to mask the signal of low level clouds, meanwhile the 11.0 μm temperature heavily decreases in accordance with the atmospheric lapse rate because of the negligible cloud transmittance and near-blackbody emittance. As the cloud top rises into the upper tropospheric layers, the 6.7 μm signal also begins to respond and the temperatures for both channels significantly converge, so that at the tropopause the BTD is near zero and, in the case of an increasing temperature profile in the lower stratosphere, the 6.7 μm brightness temperature may actually exceed that at 11.0 μm due to the presence of absorbing/emitting vapour at these levels [*Turk and Miller* (2005)].

Therefore, according to what has been illustrated above, if an opaque cloud is strongly developed in height up to the tropopause or overshooting into the stratosphere, the BT in the water vapour channel can approach or be larger than the BT in the infrared channel. Subsequently, the BTD that assumes values very close to zero is a useful indicator of the presence of optically thick cloud at or near the tropopause, meanwhile positive values provide a good hint on the presence of an overshooting top. *Schmetz et al.* (1997) found that, in these cases in contrast to the normal condition (clear sky or low level cloud), the BTD can get up to 6 - 8 K.

Thus, this simple but specific test can provide a very good information about cloud systems populating scenes to be studied in the following.

3.4 DICHOTOMOUS STATISTICS

In this work the *dichotomous statistic* is used to compare the outputs of both softwares described in previous sections.

The discrete dichotomous variables are nominal variables which have only two categories or levels, *yes* or *no*. In order to apply this kind of statistic to the present analysis, the response of the two different methods has to be interpreted or arranged so as to be treated like a variable, e.g. in the cloud mask case we will study the presence or absence of cloud, or cloudy(yes)/cloud free(no). Moreover, one of the analysed softwares will have to be considered as truth, then leading the comparison, (software 1) and the other to be treated as the one to be tested (software 2)[6].

In this way the combination of the outputs (yes or no) of the two softwares gives rise to four event categories:

- ***hits***: events that occur according to both softwares;
- ***misses***: events that occur for software 1, but not for software 2;
- ***false alarms***: events that occur for software 2, but not for software 1;

6 the assignment of these two roles will be explained in chapter 5.

- ***correct negatives***: events that do not occur according to both softwares.

These can be represented in a 2×2 contingency matrix (table 3.8).

		Software 1	
		YES	**NO**
Software 2	**YES**	Hits	False Alarms
	NO	Misses	Correct Negatives

Table 3.8: *Contingency Matrix.*

A perfect agreement between the two compared systems would produce only hits and correct negatives and no misses or false alarms. Moreover, a large number of categorical statistics can be computed from the elements in the contingency matrix[7]. The parameters used in this study are listed below:

- accuracy (ACC), describing the fraction of correctly detected occurrences and given by

$$ACC = \frac{hits + correct\ negatives}{total} \tag{3.2}$$

  it ranges in $[0, 1]$ and has a perfect score value equal to 1;

- bias (BIAS), ranging from 0 to ∞, with a perfect score amounting to 1, it is defined as

$$BIAS = \frac{hits + false\ alarms}{hits + misses} \tag{3.3}$$

  and it indicates whether the software 2 has a tendency to underestimate (BIAS$<$ 1) or overestimate (BIAS$>$ 1) the events;

- probability of detection (POD), defined as

$$POD = \frac{hits}{hits + misses}, \tag{3.4}$$

  it ranges from 0 to 1 with a perfect score value equal to 1, and describes what fraction of software 1 "yes" events are correctly detected by software 2;

7 more info available on the website http://www.cawcr.gov.au/projects/verification/#Standard_verification_methods

- false alarm ratio (FAR), has a perfect score amounting to 0 and a value range of $[0, 1]$, is defined as

$$FAR = \frac{false\ alarms}{hits + false\ alarms} \tag{3.5}$$

  and indicates the fraction of detected events by software 2, which do not occurr according to software 1;

- probability of false detection (POFD), which represents the fraction of the software 1 "no" events that are incorrectly classified as "yes" by software 2, is given by

$$POFD = \frac{false\ alarms}{correct\ negatives + false\ alarms} \tag{3.6}$$

  with a perfect score amounting to 0 in the range of values $[0, 1]$;

- Heidke Skill Score (HSS), even known as the *Cohen's* κ, is defined as

$$HSS = \frac{(hits + correct\ negatives) - (expected\ correct)_{random}}{total - (expected\ correct)_{random}} \tag{3.7}$$

  where

$$\begin{aligned}(expected\ correct)_{random} = \frac{1}{total}[&(hits + misses)(hits + false\ alarms) + \\ &+ (correct\ negatives + misses)(correct\ negatives + false\ alarms)].\end{aligned} \tag{3.8}$$

  The HSS measures the accuracy of consistent detections after eliminating those which would be correct due purely to random chance. The parameter ranges in $[-1, 1]$: negative values indicate that the detection chance is better, 0 means no skill, and 1 is the perfect score value.

4

CASE STUDIES

In the current chapter a description is provided of the analysed case studies. They have been chosen in order to contain a wide variety of cloud types with particular regard to convective systems, which have an enormous importance in weather forecasting due to the risk they represent. Moreover very thick and vertically developed cloud systems represent the cloud type for which MWCC algorithm gives better feedbacks.

The selected case studies include:

- two cases of highly localized convective systems, which caused floods in the affected areas;
- one hailstorm event;
- three scenes containing convective systems over the Mediterranean Sea with the emission of Terrestrial Gamma-ray Flashes (TGFs).

Details on the temporal and geographical collocation of the events are shown schematically in table 4.1. Note that the selection of the satellite overpass times has been dictated by the AMSU-B/MHS acquisitions. Indeed, being these sensors on board polar orbiting satellites, they provide only two overpasses per day over a given area and thus it could be more difficult to find the overpasses that are temporally and spatially close to the event. On the contrary the selection of the acquisition times for SEVIRI is easier, since this sensor is located on a geostationary platform performing an entire Earth disk acquisition every 15 minutes. However, notice that the difference between the acquisition times of the concerned sensors are always small and never exceed 6 minutes.

Since the processing paths of both cloud classification softwares and the resulting output interpretation, are affected by the lighting conditions, the different cases are classified also according to this feature (table 4.2), by using the provided SAFNWC flag. So, taking advantage of this information, the scenes can be divided into four cases predominantly or totally *daytime* and four cases mainly classified as *twilight* or *night-time*.

Hereafter a brief description of each weather event and of its characterizing physical phenomenon, is presented and completed with the results of the BTD test illustrated in chapter 3. This is a very useful tool to evaluate the cloud vertical development and the possible presence of an overshooting top.

	YYYY/MM/DD	hh:mm (AMSU-B/MHS)	hh:mm (SEVIRI)	Location	Region
Localized systems causing floods	2006/07/03	10:18	10:15	Vibo Valentia	Calabria
		12:33	12:30		
	2014/09/05	08:36	08:30	Gargano	Apulia
Hailstorm	2015/01/22	19:28	19:30	Metapontino	Basilicata
TGF emission	2004/05/27	20:32	20:30	Mediterranean Sea	Eastern Basin
	2004/11/07	12:47	12:45	Mediterranean Sea	Central Basin
		16:14	16:15		
	2006/10/16	04:54	05:00	Mediterranean Sea	Central-Eastern Basin

Table 4.1: *Case studies selected.* These are categorized in three classes by the phenomenon characterizing them, and, for each one the date, AMSU-B/MHS and SEVIRI acquisition UTC times, location and region of occurrence are given. Note that, for the events of 2006/07/03 and 2004/11/07, two times have been taken, showing different stages in the involved system evolution.

Daytime	Night-time or Twilight
2004/11/07 - 12:47	2004/05/27 - 20:32
2006/07/03 - 10:18	2004/11/07 - 16:14
2006/07/03 - 12:33	2006/10/16 - 04:54
2014/09/05 - 08:36	2015/01/22 - 19:28

Table 4.2: Case studies classified via the SEVIRI illumination flag which characterizes the majority of the involved scenes.

4.1 LOCALIZED SYSTEMS CAUSING FLOODS

Vibo Valentia - 2006/07/03

On July 3rd 2006 exceptional and intense rainfall affected central Calabria lasting a few hours. A rain gauge in the city of Vibo Valentia registered more than 200 mm of rain in about 2 hours. Such rainfall amount was far above the usual seasonal

average [*Gabriele and Chiaravalloti* (2011)] and then it caused severe and widespread damage.

This kind of unpredictable event is among those classified as *flash floods*, that is very intense and sudden rainfall events with a considerable thunderstorm severity. It is typically activated by a line of convective convergence that persists for several hours on the same locations.

Radar images are not available in this specific case in order to analyse and classify the system. Nevertheless from the satellite imagery and pluviometric analysis conducted by *Gabriele and Chiaravalloti* (2011), we can deduce that it was a very powerful thunderstorm with the most intense phase between approximately 8:30 and 11:00 UTC.

Therefore two colocated AMSU-B/MHS and SEVIRI overpasses are selected. The first of them concerns the mature phase of the storm, as it can further be deduced by examining the figure 4.1(a), a map in shades of gray of the brightness temperatures acquired in the IR10.8 SEVIRI channel, where pixels having BTD greater than or equal to 0 are marked with colors. The positive BTD values thus detected, albeit in a minimal amount, display the presence of clouds high and cold enough to give a signal in the carried out threshold test. The second time chosen, instead, involves the same system, but in its final dissipation phase, where only cirrus and altostratus cloud has remained, as proved by the results in figure 4.1(b) in conjunction with the recorded observations.

Gargano - 2014/09/05

Another isolated system, which affected a small area of Southern Italy causing severe flooding, is the one strucking Apulia in the days 2014/09/03-06.

Unlike the previous case, this system has continued to regenerate itself for a long time producing considerable rainfall, 600 mm of rain in 4 days, an amount comparable to the average during a whole year in the same areas[1]. Such extreme weather event was caused by a persistent low pressure vortex resulting from a cold perturbation from the north, and its interaction with the warm and moist atmospheric layer in contact with the sea.

By observing the brightness temperature data illustrated in figure 4.2(a), the storm over the Gargano's area can be identified. The little amount of pixels over the storm exhibiting positive BTD values is probably due to a convective plume and, as a consequence, to a concentrated overshooting top. This latter, however, is not so evident maybe due to the system small size, which prevents it from reaching the stratosphere, or to a satellite overpass, which should have captured a little intense storm stage.

1 taken from http://polaris.irpi.cnr.it/wp-content/uploads/Report-annuale-2014.pdf and http://www.lagazzettadelmezzogiorno.it/notizie-nascoste/report-della-protezione-civile-no752082/.

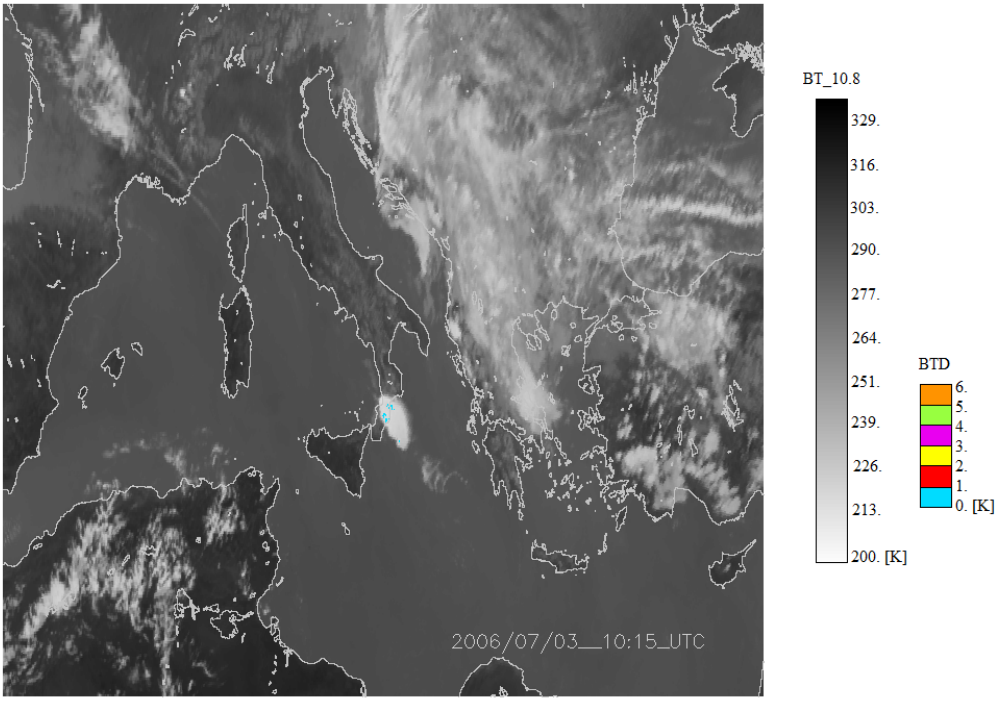

(a) 2006/07/03 10:15 UTC

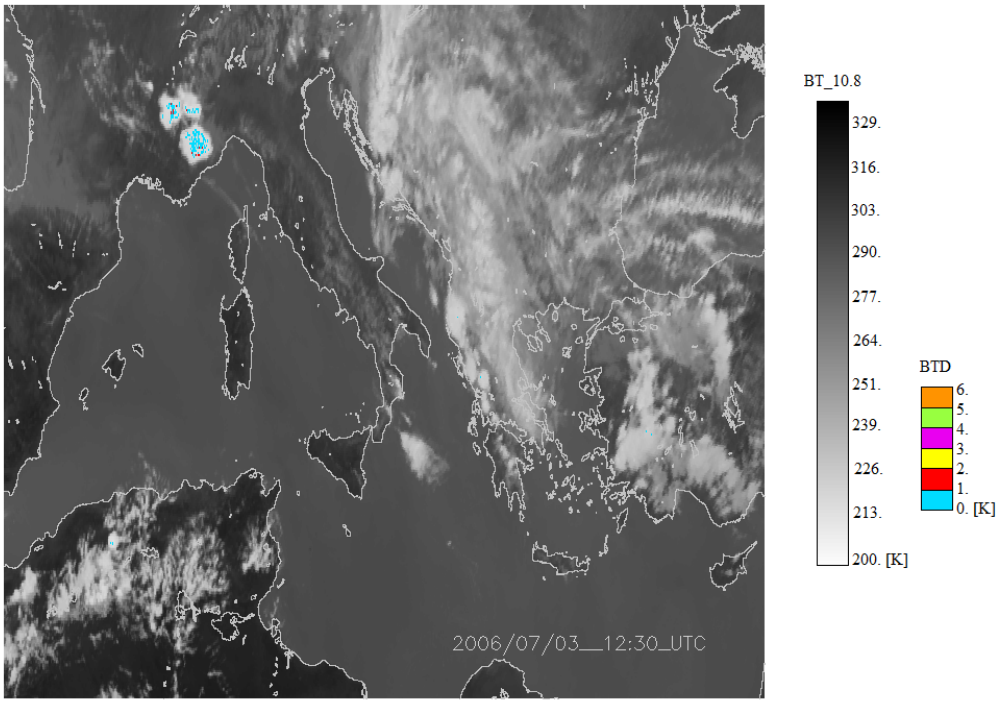

(b) 2006/07/03 12:30 UTC

Figure 4.1: BTD test results for Vibo Valentia flash flood. The maps in shades of gray depict the brightness temperatures acquired in the IR10.8 SEVIRI channel, to which all pixels having BTD values greater than or equal to zero are overlaid in RGB colors.

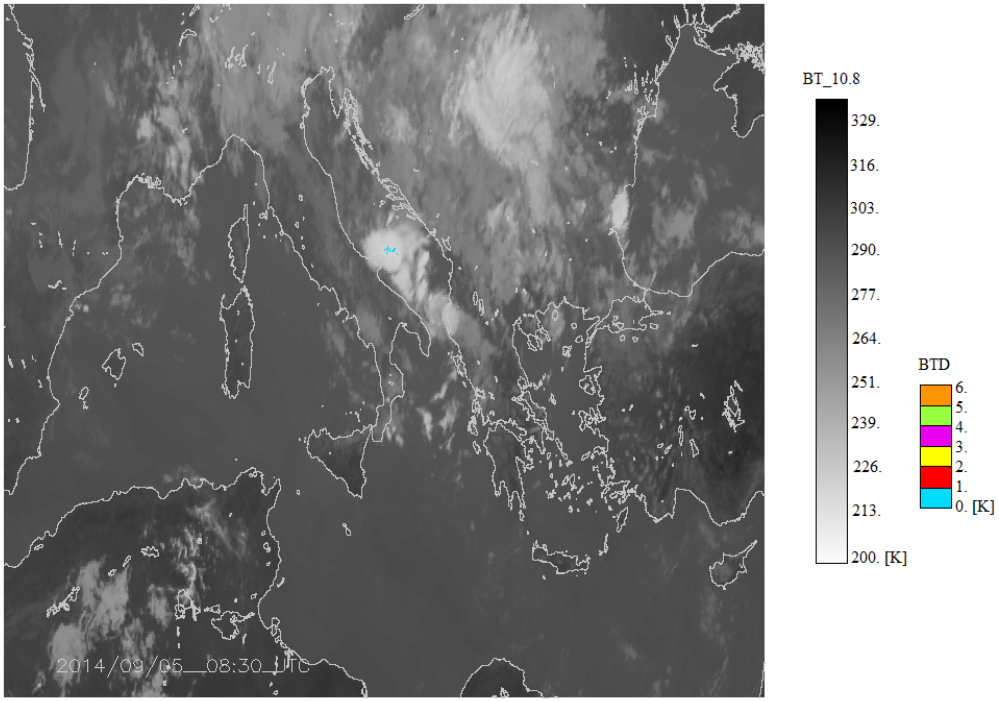

(a) 2014/09/05 08:30 UTC

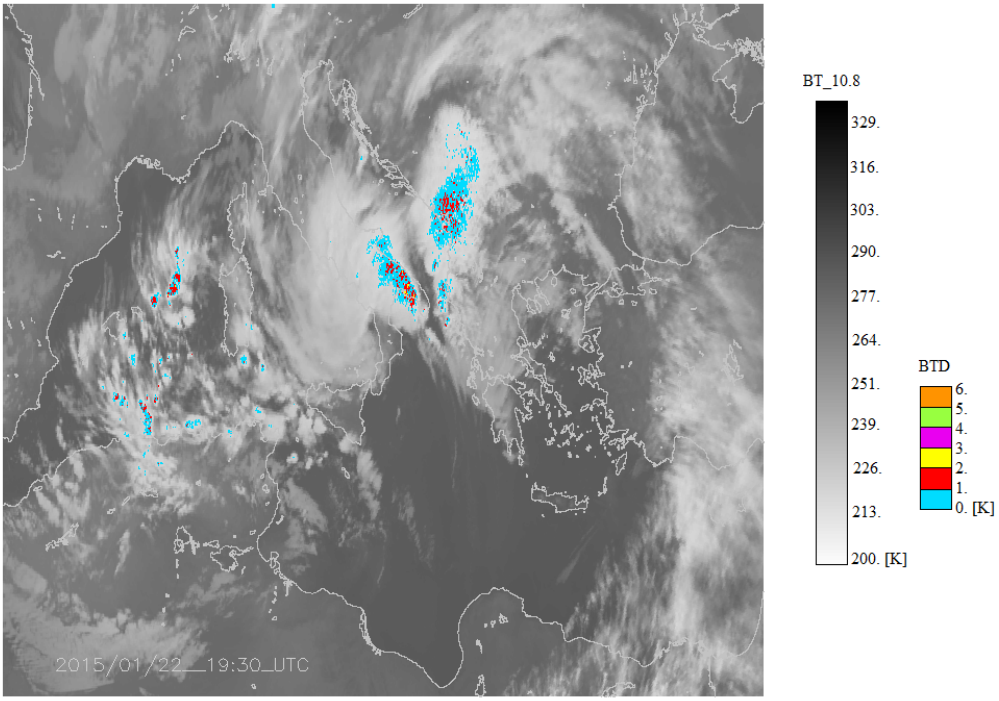

(b) 2015/01/22 19:30 UTC

Figure 4.2: The same as in 4.1 but for the localized event affecting Apulia region on 2014/09/05 (a) and the hailstorm hitting Southern Italy on 2015/01/22 (b).

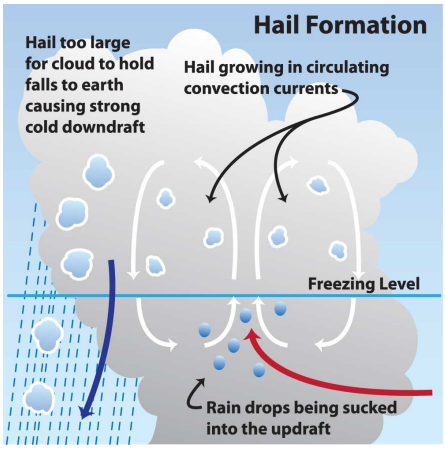

Figure 4.3: Schematic representation of the hail formation process. Image from NASA- http://scijinks.jpl.nasa.gov/review/rain/

4.2 HAILSTORM EVENT

Southern Italy - 2014/09/05

Hail storms are defined as any thunderstorm that produces hailstones that fall to the ground, also if, such term is especially used when the amount or size of the hail is considered significant [*American Meteorological Society* (2014)].

Hail stones, usually, form in the strong thunderstorm clouds characterized by intense updraft winds and where they can grow by colliding with supercooled water dropletss. Within this kind of storm systems, in effect, the supercooled water freeze on contact with ice crystals, frozen raindrops, dust or some other nuclei. After that the strong upwards winds carry the frozen hydrometeors thus formed up towards the cloud top, where they encounter more supercooled water and continue to grow (*accretion process*). But, at some point, gravity takes over and the hail stones start to fall back through the cloud, before being pushed back again towards the high cloud layers by the updraft gusts. The stronger the updraft the larger the hailstone can grow. The hail formation cycle is schematically depicted in figure 4.3 and, under appropriate conditions (i.e. high liquid water content, large cloud-drop sizes, great vertical cloud extent), can be repeated many times before the hail stones become heavy enough to overcome the updraft winds and to fall finally to the ground.

All the necessary requirements for a hailstorm development generally occur in the warmer seasons, when the significant surface heating allows to accumulate enough energy to trigger the storm described above. Therefore, the strong hail-producing event hitting Southern Italy (Sicily, Calabria and Basilicata regions) in January 2015 and that we have chosen as case study, represents a notable exception. It caused very intense wind gusts, lightning and hailstones with diameters up to 5 cm and, therefore, it is a very good cloud structure example to be studied by means of several instruments.

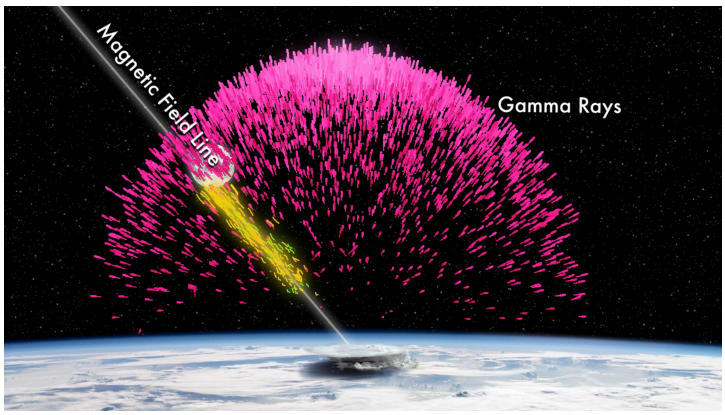

Figure 4.4: Schematic representation of Gamma-ray emission by a sever thundercloud. Image available at https://svs.gsfc.nasa.gov/cgi-bin/details.cgi?aid=10706.

Through an observation of the BTD threshold test output, which also for this case has been performed and shown in figure 4.2(b), we infer the system was very intense, developed in height and with a marked presence of overshooting top. In front of the system we note another one of almost equal intensity, but separated from the first by a strip of dry air.

4.3 TGF EMISSIONS

Mediterranean Sea - 2004/05/27 - 2004/11/07 - 2006/10/16

The Terrestrial Gamma-ray Flashes (TGFs) are short gamma-ray bursts (up to 1 ms) from coarse areas coincident with thunderstorms regions, first discovered by *Fishman et al.* (1994). The physics behind the production of TGFs is not completely known. The current theory states that the strong electric fields in larger thunderclouds, sometimes, accellerate electrons to nearly the speed of light, so they emit gamma-rays via bremsstrahlung interactions with air. The measured photons energies in TGFs are found to be up to several tens of MeV [*Smith et al.* (2005); *Marisaldi et al.* (2010)], which make them the most energetic natural photon phenomenon on the Earth.

This phenomenon, illustrated in figures 4.4 and 4.5, is observed more frequently in the equatorial belt, where there are the deeper and stronger convections and most of the satellites that can observe such a type of emission. However, also at mid-latidudes similar events occur and three examples are those detected in the Mediterranean Basin:

- 2004/05/27 19:40 UTC,
- 2004/11/07 17:03 UTC,
- 2006/10/16 07:21 UTC.

The satellite sensor acquisitions nearest to the previous dates and times are selected as case studies, as summarized in table 4.1.

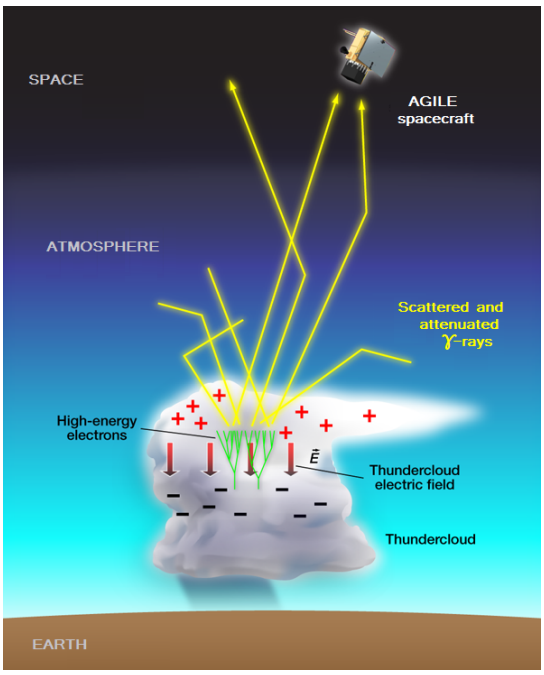

Figure 4.5: Schematic representation of a TGF emission. Image available at http://agile.asdc.asi.it/news.html.

As for the November 2004 event, a second AMSU-B overpass at 12.47 UTC is taken into account despite the greater temporal distance from time of TGF burst. In this way it is possible to study the same system in two different stages of its evolution, as for the Vibo Valentia flash flood case. In effect, by observing the BTD test results in figures 4.7(a) and 4.7(b), it can be seen how the same system has been caught in two different phases, one with a convection still not very pronounced 4.7(a) and the other in its phase of greater intensity 4.7(b).

Then, from the maps in figures 4.6(b)-4.7(b) regarding the October 2006 and November 2004 systems in their phase closest to the TGF emission, we can notice the presence of well developed deep convective clouds with possible overshooting tops characterized by positive BTD ranging from 1 to 3 K. Moreover, by looking at the results related to the May 2004 case in figure 4.6(a), it is possible to observe something different if compared to the others, or specifically the scarcity of pixels with BTD greater than or equal to zero. This result could be due to a scarcely overshooting top or to an icy structure presence above the system in question. Actually Weather Research & Forecasting Model (WRF) simulations support the hypothesis of the presence of frozen structures standing above a shallow convection.

Hence, two of the systems generating a gamma-ray emission have been observed above longlasting deep conventions, whereas the third one, has occurred on a shallow convection system and, therefore, it seems to be an exception to the current theory of TGFs. For this reason, there is an interest in investigating the aforementioned scenes through methods using different physical principles, by observing the results and comparing them with each other.

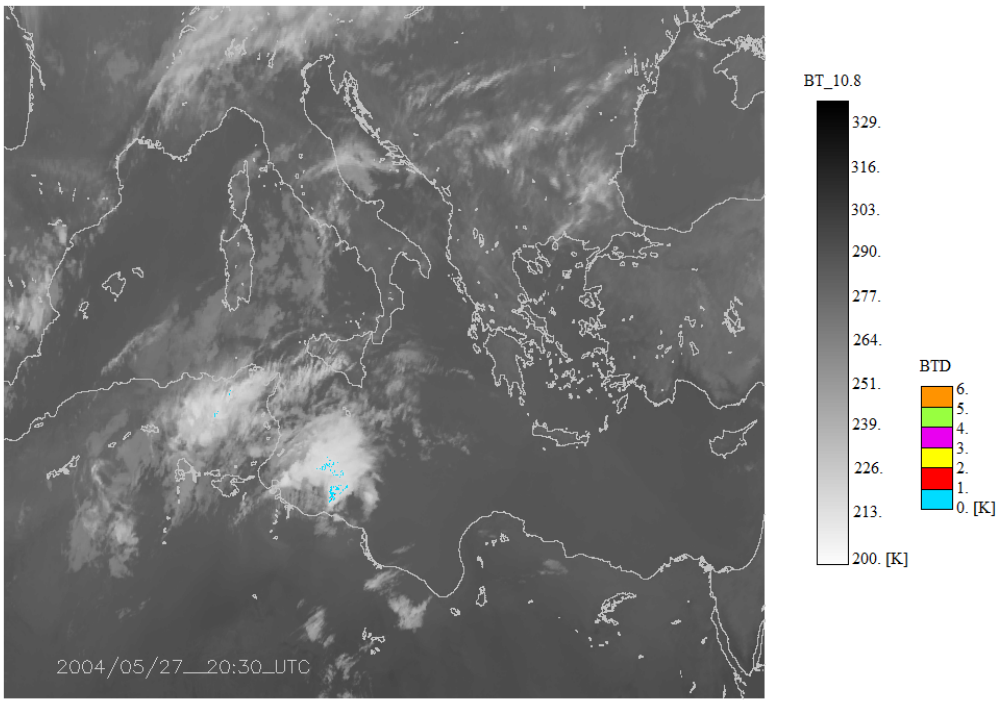

(a) 2004/05/27 20:30 UTC

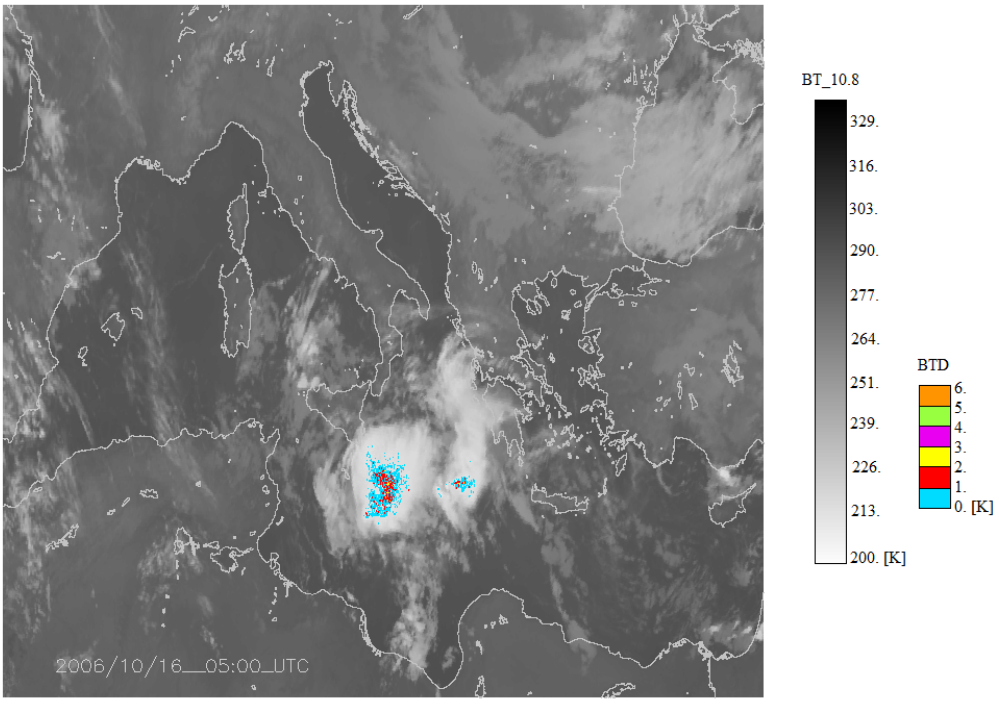

(b) 2006/10/16 05:00 UTC

Figure 4.6: The same as in 4.1 but for the 2004/05/27 (a) and 2006/10/16 (b) events characterized by a TGF emission.

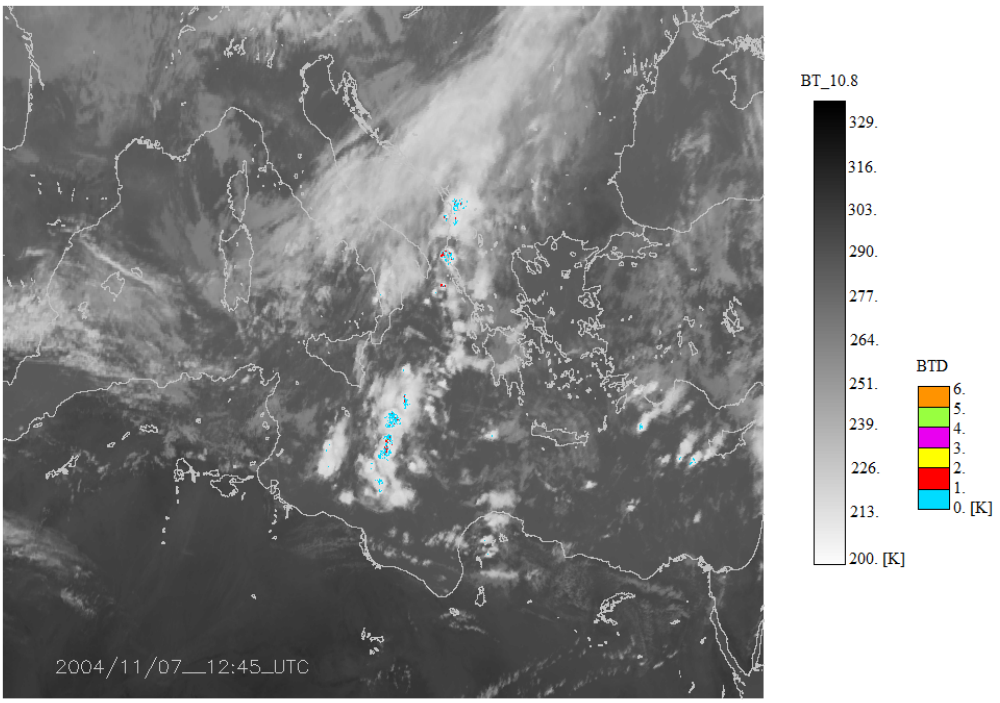

(a) 2004/11/07 12:45 UTC

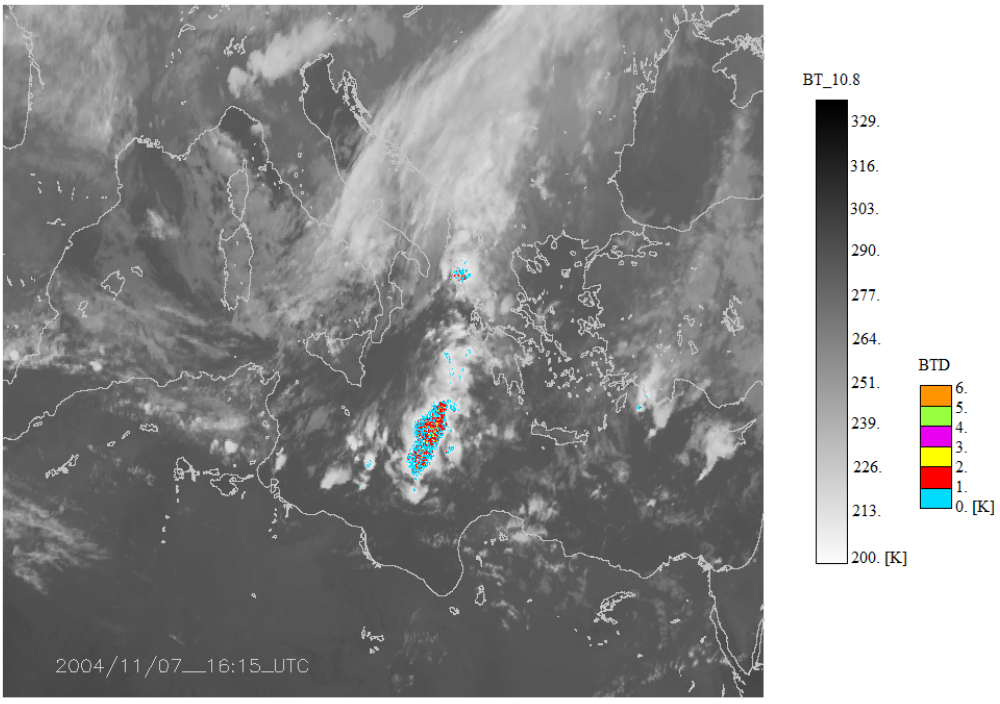

(b) 2004/11/07 16:15 UTC

Figure 4.7: The same as in 4.1 but for the 2004/11/07 event characterized by a TGF emission.

5 ANALYSIS AND RESULTS

In this chapter the analytical treatment of the data and the final results are presented.

First of all the general remapping strategy of the two cloud classification method outputs, customized for each output type, is presented. This procedure is motivated by the different spatial resolution of SAFNWC and MWCC outputs. Thus to enble any kind of comparisons between them, it is necessary to project all the data on a common grid.

After this pre-processing, the comparison concening the cloud masks is shown, so as to determine whether the different technologies produce the same results in identifying cloud presence or absence. Subsequently, over the pixels covered by cloud according to both softwares, a study is performed in order to assess the agreement extent in the cloud classification. Note that, for the cirrus cloud classes a separate mention is made.

5.1 DATA REMAPPING PROCESS

As discussed in chapter 3, the sensors for data acquisition have a different spatial resolution (3 km at nadir for SEVIRI and 16 km at nadir for AMSU-B/MHS) and also the outputs from the processing codes reflect such features. To be able to make any kind of comparison, therefore, the first step is using a common resolution.

The choice of the new grid element size is fixed by the following factors: firstly, this can not be smaller than the worse instrumental resolution, since a rise in resolution would be physically not allowed; secondly, it can not be too large, considering that this would imply a great detail loss. The right compromise, therefore, seems to be the grid step of 0.25° (about 27.75 km), already widely known and used in gridded satellite products and comparisons between datasets which had, originally, a different resolution.

5.1.1 *SAFNWC software product remapping*

Cloud Mask

The data remapping process begins from the SAFNWC CMa output, the maps of which are shown in figure 5.1 for the 2006/10/16 event as an example.

Since this is the first attempt to get an idea of the correct approach to be used, different remapping criteria have been designed and subsequently tested on all case studies, in order to get comparable data of reasonable quality while keeping a significant statistical sample. They employ different combinations of CMa classes and processing quality flags (see subsection 3.1.2), so as to realize the kind of pixels

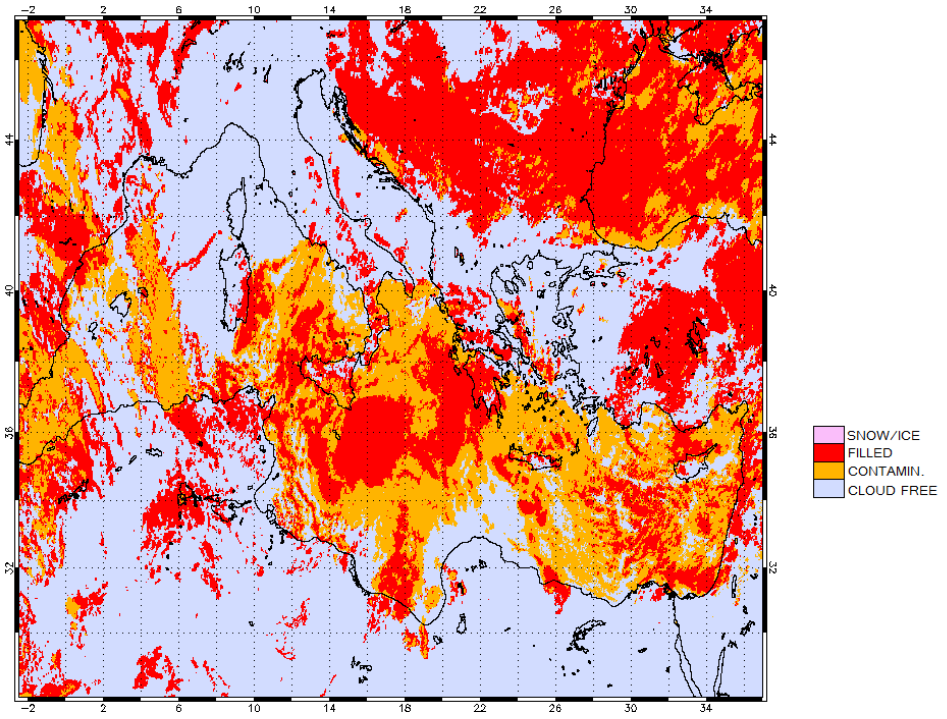

(a) CMa

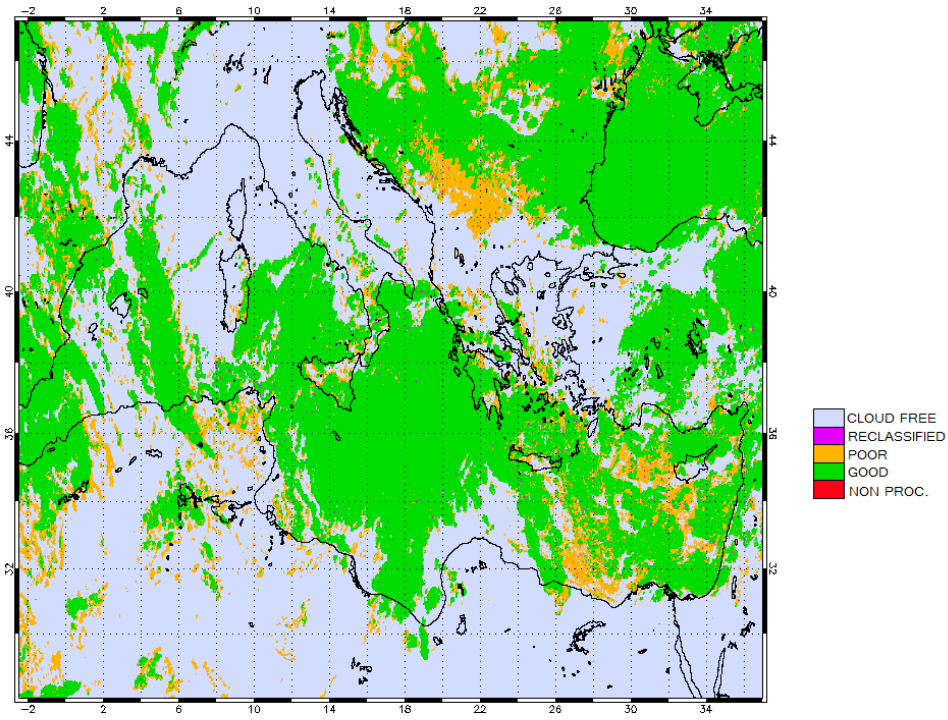

(b) CMa quality flag

Figure 5.1: SAFNWC CMa (a) and associated processing quality flag (b) for the 2006/10/16 event.

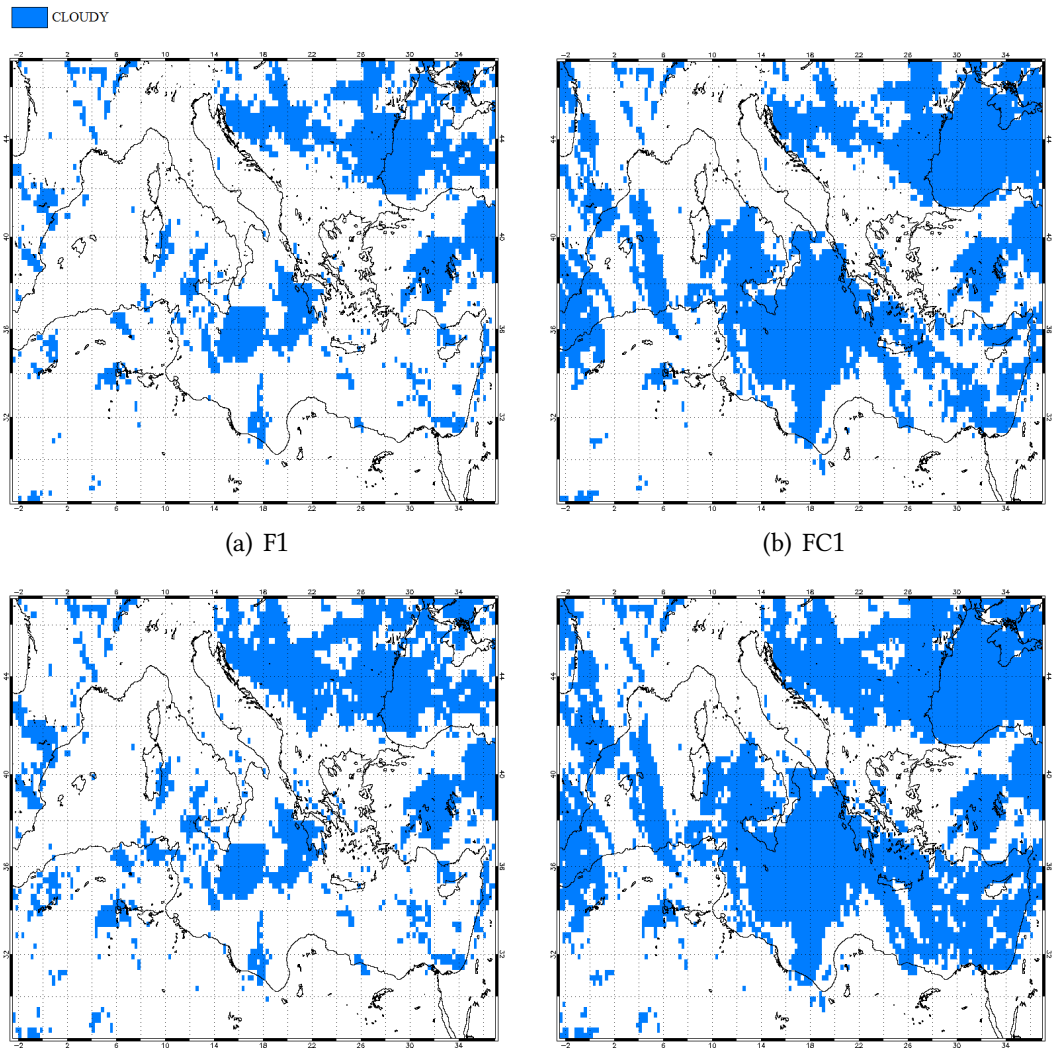

(a) F1 (b) FC1

(c) F12 (d) FC12

Figure 5.2: SAFNWC CMa remapped for the 2006/10/16 event.

to keep or discard by building the new grid. Note that all the corrupted or very low quality pixels have not been taken into account in the test elaboration, in order to base the subsequent analysis on a data set with a good reliability degree.

These criteria require that a cell of the new grid is defined as cloudy if, at least 70% of the highest resolution pixels inside that belong to:

- cloud filled category with a processing quality flag associated amounting to 1 (F1)[1];
- cloud filled category with a processing quality flag associated amounting to 1 or 2 (F12);
- cloud filled or cloud contaminated category with a processing quality flag associated amounting to 1 (FC1);

1 the abbreviation by which each criterion is named, is given in brackets.

– cloud filled or cloud contaminated category with a processing quality flag associated amounting to 1 or 2 (FC12).

Note that a SEVIRI pixel belongs to the 0.25° cell, if its central coordinates fall inside the considered cell. Moreover, the filling threshold has been fixed at 70% in order to ensure that the cloudy category allocation of the largest pixel, only occurs in the presence of a reasonable population of the SEVIRI cloudy pixels.

As it was possible to observe from the results thus obtained, considering or not the pixels with a quality flag value of 2 (poor quality) does not substantially affect the remapping procedure in particular relatively to the areas analysed in the case studies. In fact these pixels are not very recurrent in these situations. As a consequence, the map couples F1-F12 and FC1-FC12 appear to be quite similar, as it is shown in panels (a)-(c) and (b)-(d) of the figure 5.2 related to the 2006/10/16 event and well representing the recorded general trend.

On the other hand, the cloud contaminated category, due to its remarkable presence within the various scenes, significantly reduces the amount of exploitable pixels when it is excluded.

For the reason mentioned above, therefore, the choice is to be made among the categories FC1 and FC12. But, since the software calculates the subsequent products, i.e. PGE02 and PGE03, on whatever the pixels classified as cloudy irrispective of the processing quality, the class choosen is the less restrictive one FC12. The SEVIRI CMa remapping algoritm is summarized in the chart of figure 5.3.

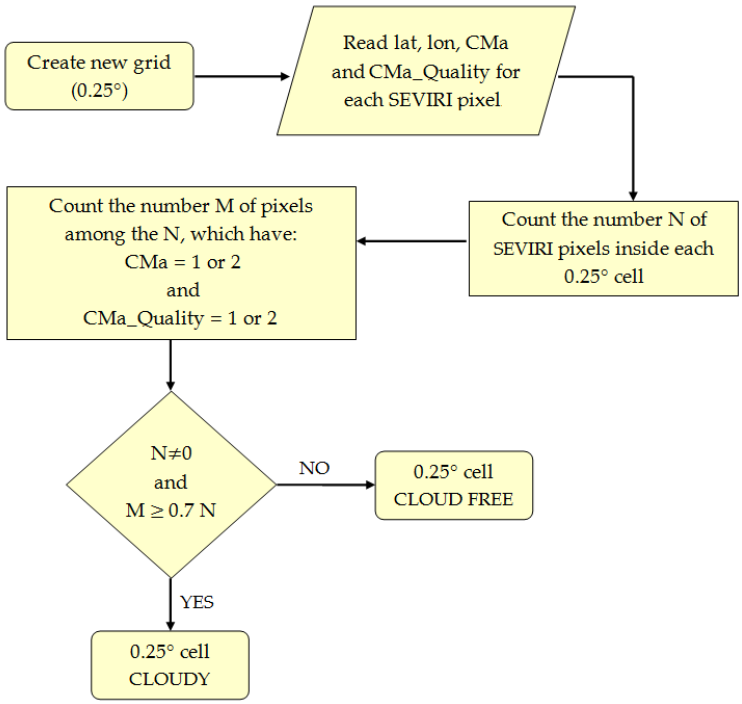

Figure 5.3: Summary chart for the SAFNWC CMa remapping algoritm.

Cloud Phase

The first condition to be satisfied is that the new grid pixels are at least at 70% filled by SEVIRI pixels with a phase value greater or equal to 1 (i.e. ice, water or undefined). This requirement allows to keep only the pixels already considered in the CMa remapping and then to make such products perfectly overlapping. Whereupon, if this is fulfilled, each pixel at 0.25° is flagged with the most recurrent cloud phase category, with a quality flag amounting to 1 or 2 (see chart in figure 5.4). Otherwise it is classified as cloud free and then discarded from the comparison. Note that, if the pixels are all equally numerous, the "undefined" flag is assigned.

In figure 5.5 an example of a phase map before and after the remapping is shown.

Cloud Type

Also in this case only the SEVIRI pixels characterized by a quality flag equal 1 or 2 are taken into account and allocated to the 0.25° grid cells. Then the most frequent cloud type is assign to each 0.25° cell. In case it is not possible to assign a cloud type to 0.25° cells (lack of a predominant cloud type at the SEVIRI pixel levels), the *"mode" method* is applied taking into account the cloud type of a set of surrounding remapped cells.

As it is shown in the example of figure 5.7 and in the chart of figure 5.6, for the current product certain classes are grouped together during the remapping, because their degree of detail is too high if compared to the classes extracted from microwave data. Thus, in order to make the comparison less unequal the undefined, non processed, cloud free land/sea and snow/ice contaminated classes, are all categorized as cloud free. Moreover, cirrus cloud categories are also reduced from 4 to 3, by combining the meanly thick with the thick ones, even if still preserving the thin and above low or medium cloud classes.

Cloud Top Temperature and Height

Compared to the previous products the CTTH is not identified by means of a flag, but through continuous values. Therefore, in order to assign to the new grid pixel a value of height, pressure or temperature, an arithmetic average computation is performed considering the SEVIRI pixels allocated in each 0.25° cell.

In this case, however, the CTTH assignement is carried out only for those 0.25° cells, where 50% of SEVIRI pixels are flagged with a height value greater than zero and a quality flag of 1 or 2 (see figure 5.8). The necessity of relaxing the threshold value from 70% as for the previous products to 50% derives from the fact that the CTTH product is not calculated for all cloud type classes[2] . Thus with the 70% threshold value a significant decrease in the number of 0.25° cells with a valid CTTH assignment would occur.

A remapping example is shown in figure 5.9.

2 no technique is proposed for low broken clouds in the software version used [*Derrien* (2013)]

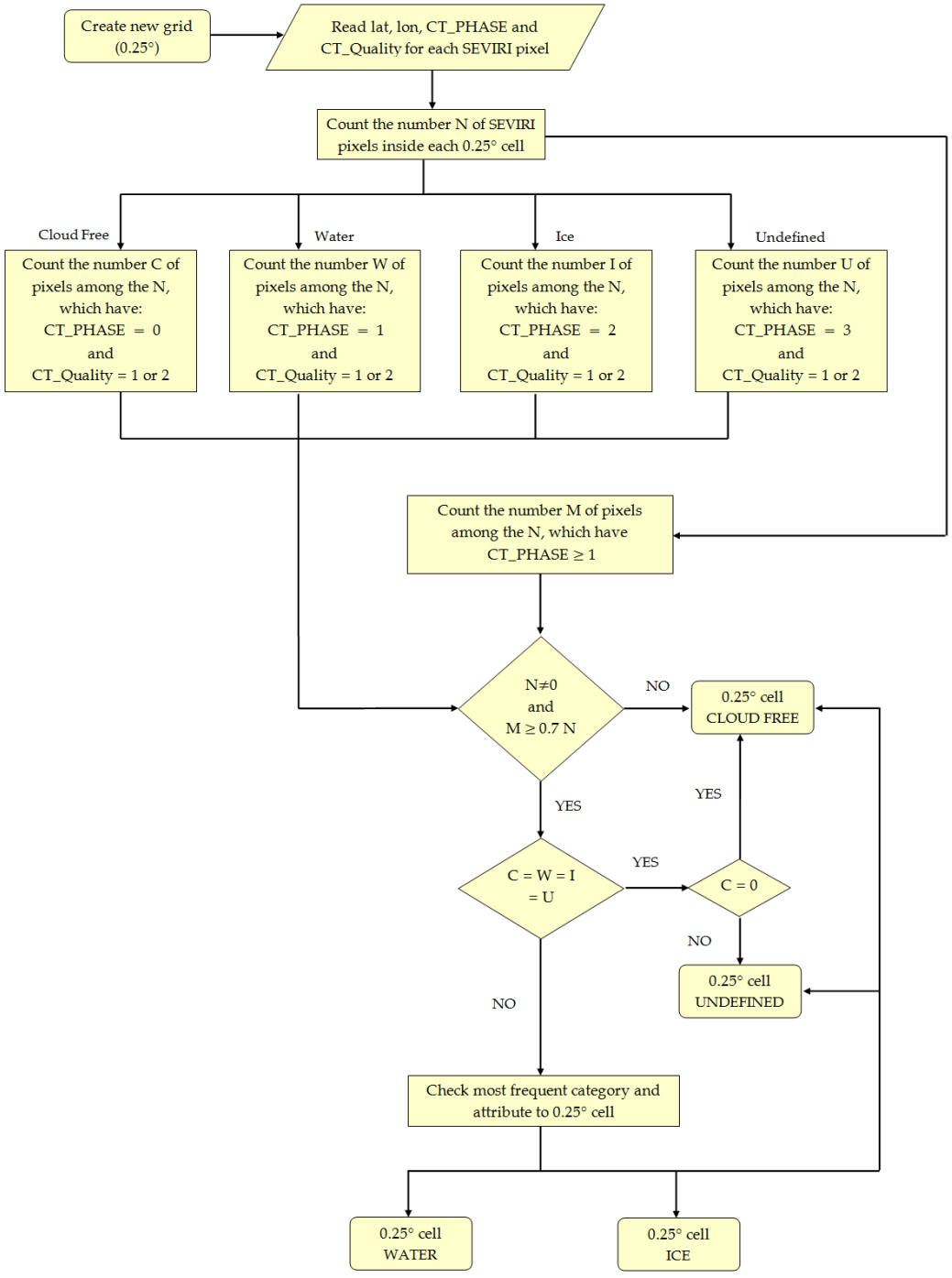

Figure 5.4: Summary chart for the SAFNWC Cloud Phase remapping algoritm.

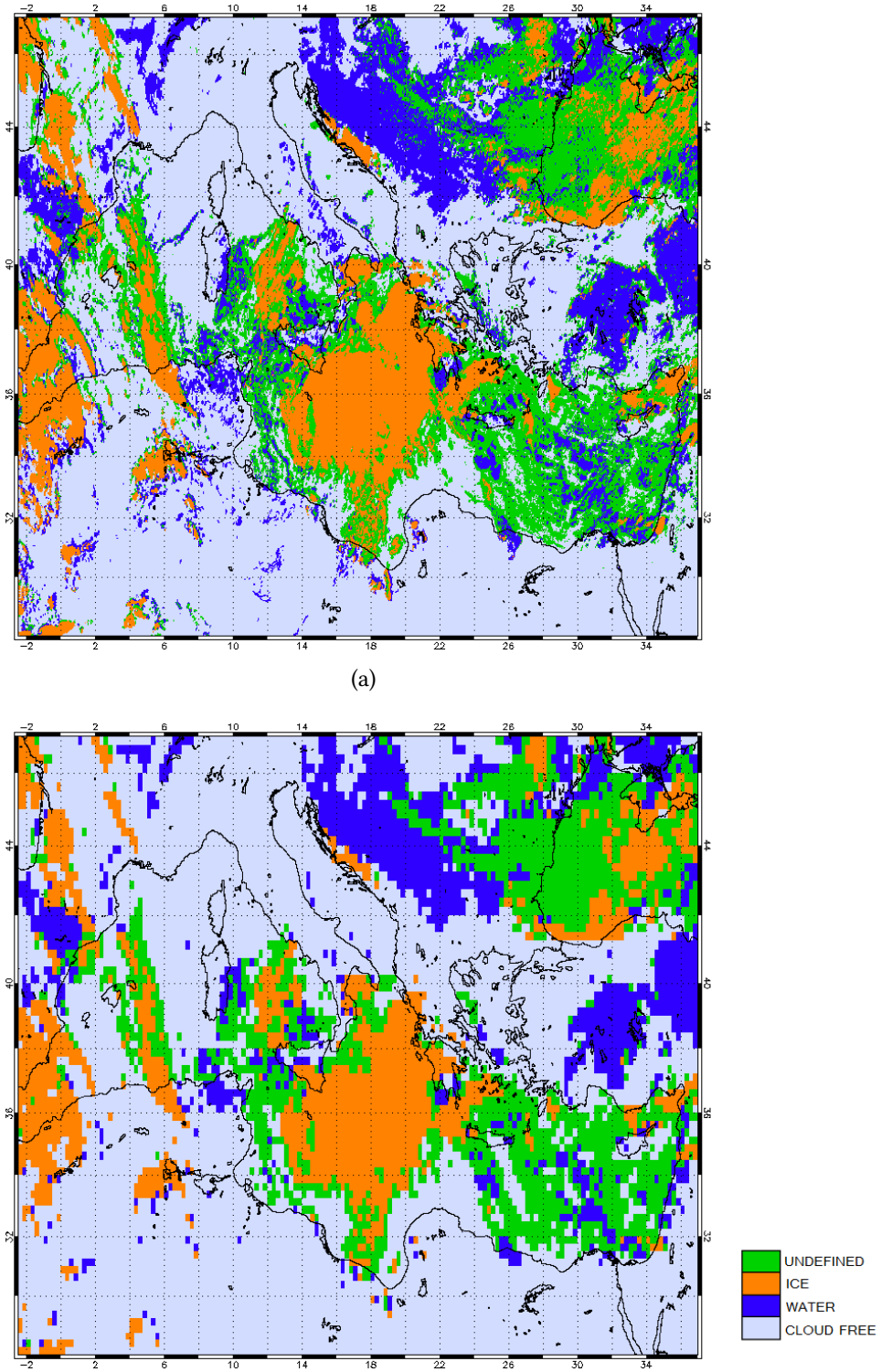

(a)

(b)

Figure 5.5: SAFNWC CMa remapped for the 2006/10/16 event.

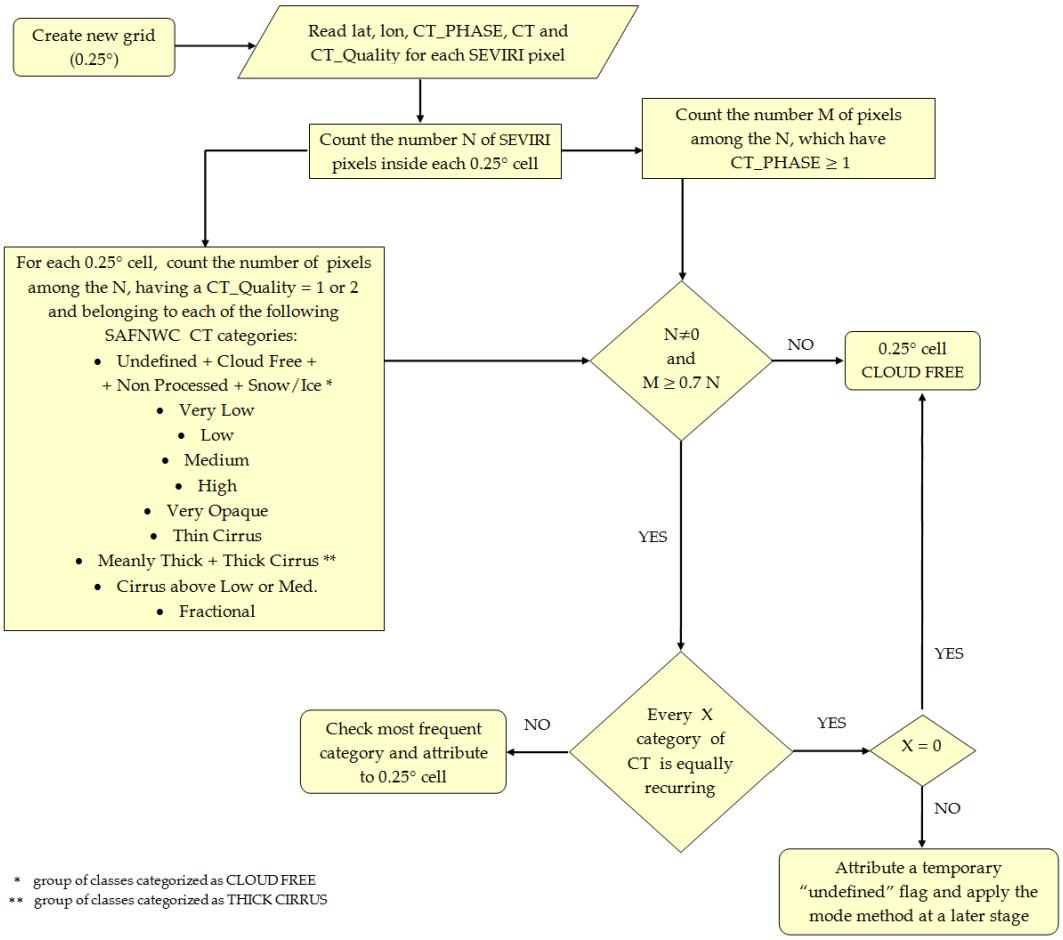

Figure 5.6: Summary chart for the SAFNWC CT remapping algoritm.

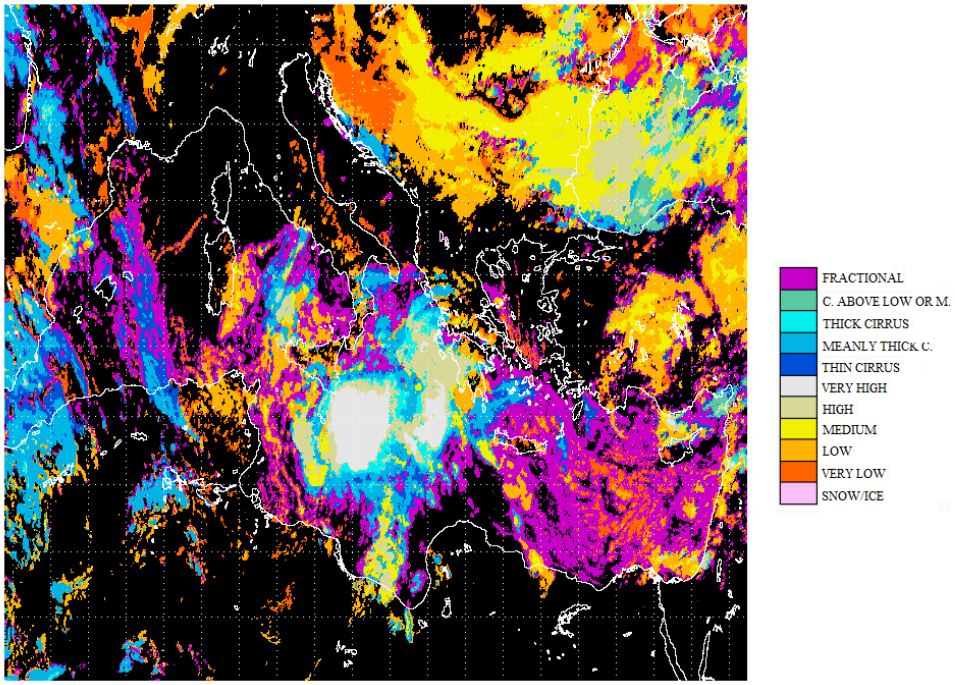

(a)

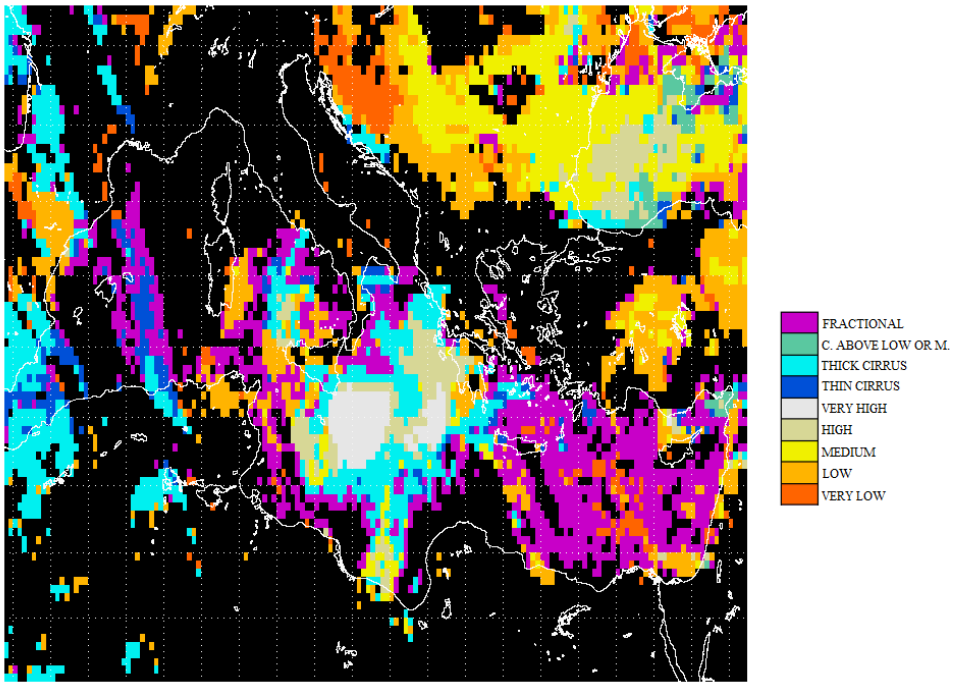

(b)

Figure 5.7: SAFNWC CT product for the 2006/10/16 event, before (a) and (b) after the remapping.

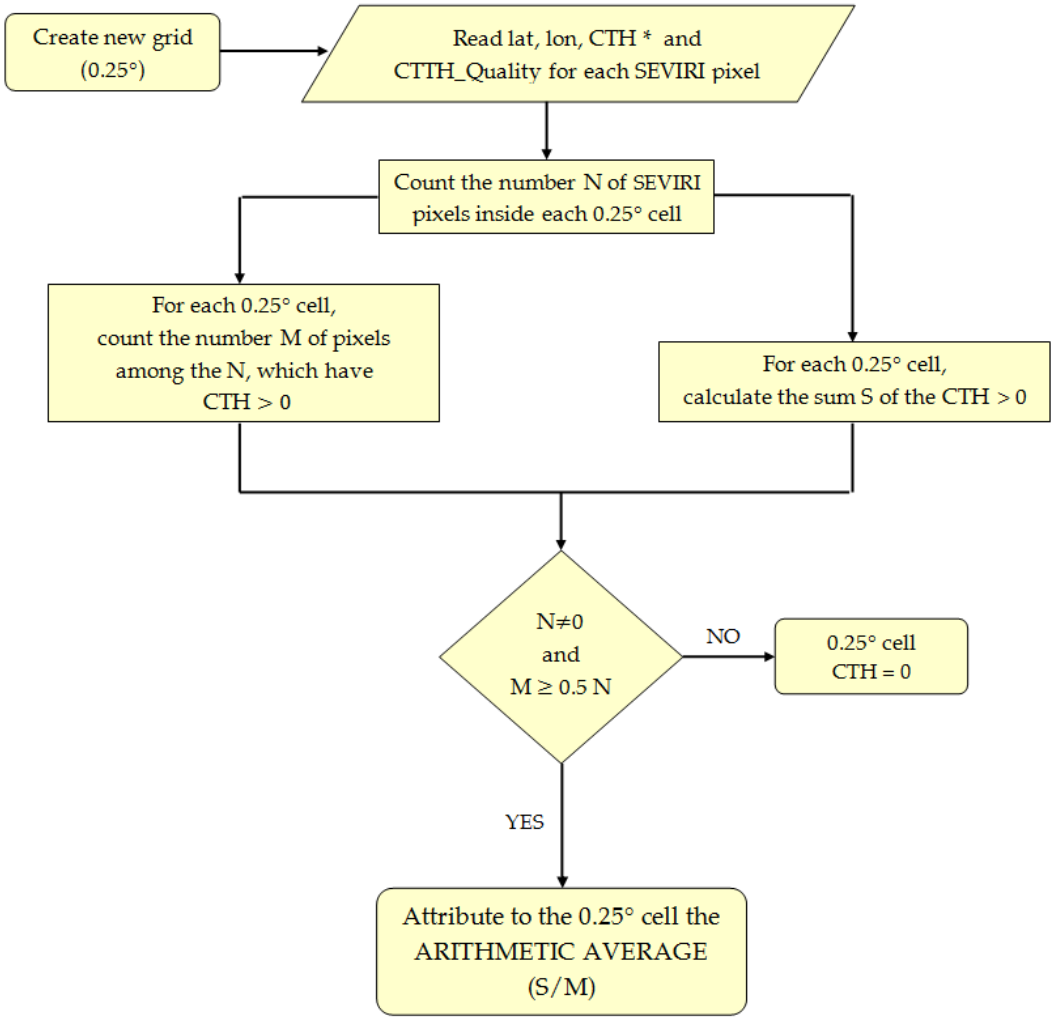

Figure 5.8: Summary chart for the SAFNWC CTTH remapping algoritm.

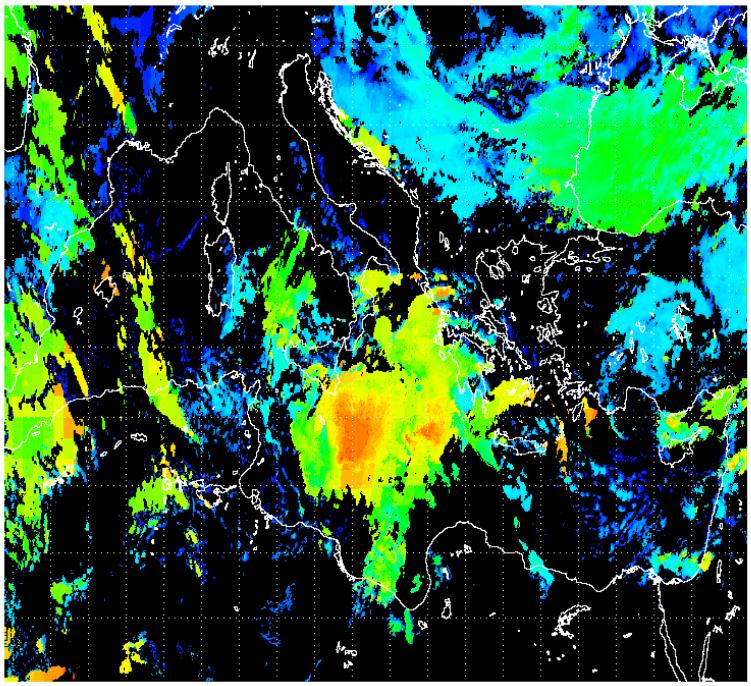

(a)

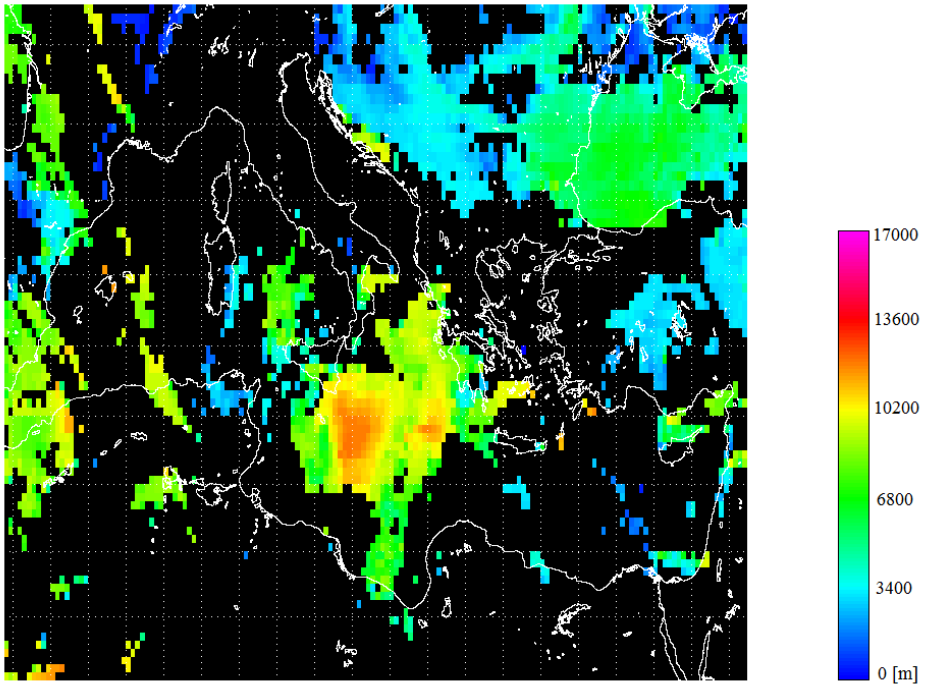

(b)

Figure 5.9: SAFNWC CT product for the 2006/10/16 event, before (a) and (b) after the remapping.

5.1.2 *MWCC algorithm output remapping*

MW Cloud Mask

The approaches used for the MW products are similar to those described above, even if in this case no quality flag is available.

Hence, in regard to the CMa remapping, a cell at 0.25° is defined as cloudy if its MWCC cloudy pixels are at least the 70%. Otherwise this is classified as cloud free, as shown in figure 5.10.

MWCC

The microwave cloud classification is carried out on the same pixels selected for the MW cloud mask, and, again, the new grid pixel flag is allocated according to the most numerous among the smaller ones located within it. Furthermore, even in this case as already done for the SAFNWC CT, if the highest resolution pixels are equally recurring, the new grid cell is flagged, at a second time, by using the mode method applied to the sorrounding cells. A summary chart for the MWCC CT remapping algoritm is given in figure 5.11.

An example of the MWCC cloud classification product and of the remapping results (both cloud mask and cloud classification), is displayed in figures 5.12-5.13.

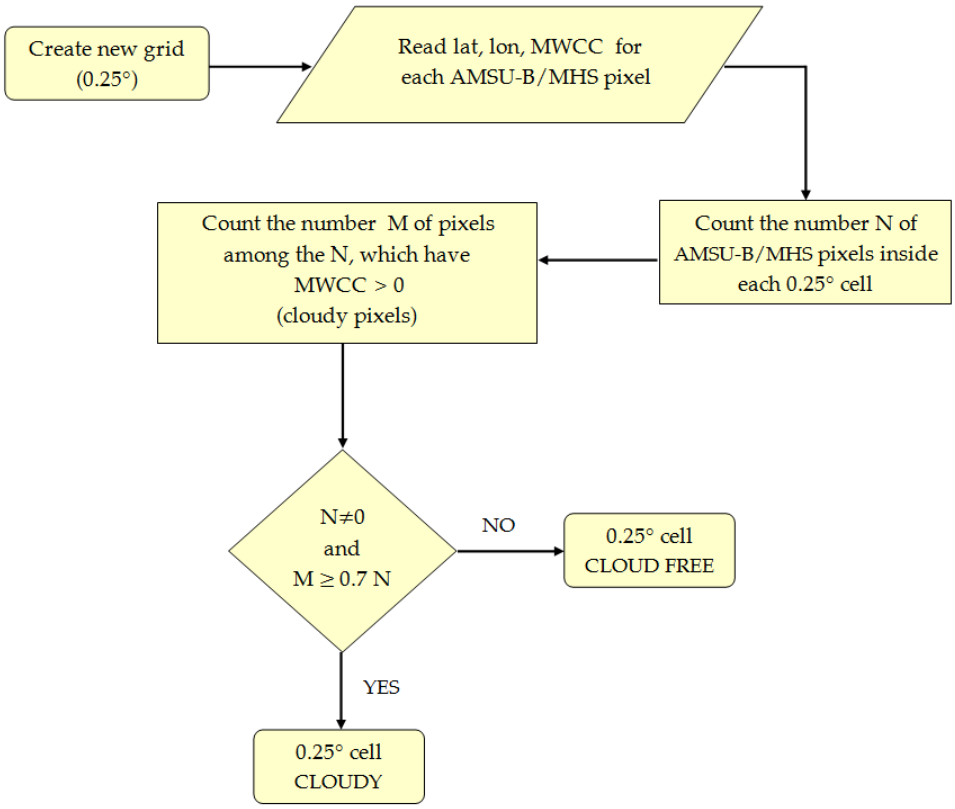

Figure 5.10: Summary chart for the MW CMa remapping algoritm.

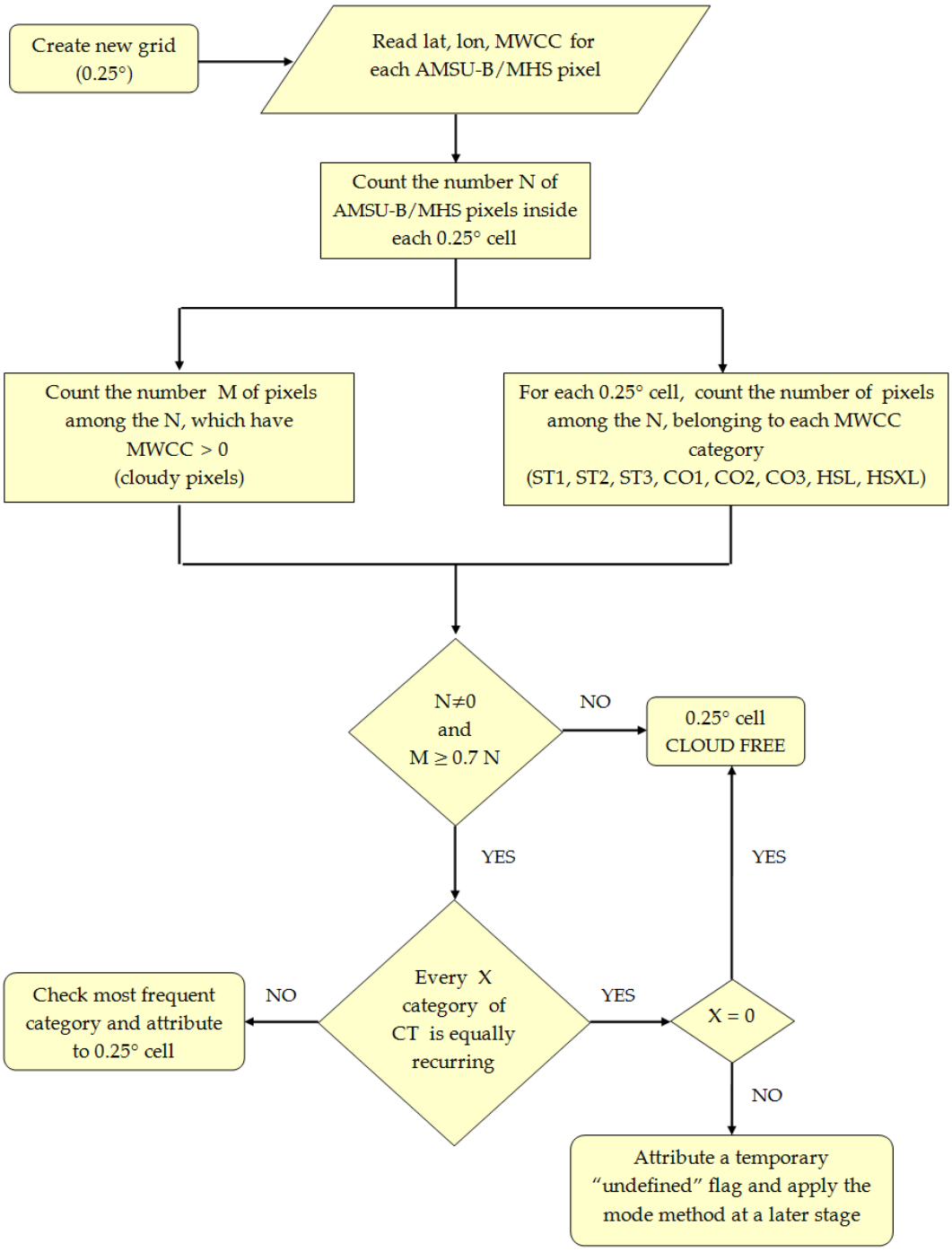

Figure 5.11: Summary chart for the MWCC remapping algoritm.

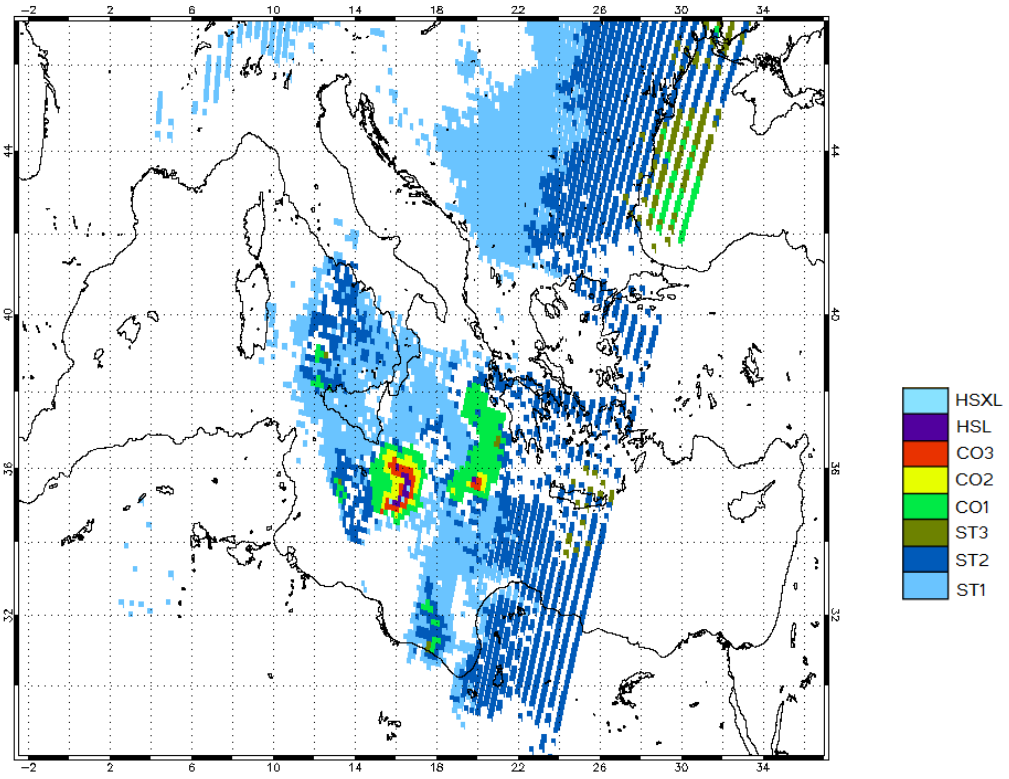

Figure 5.12: MWCC at the satellite resolution for the 2006/10/16 event.

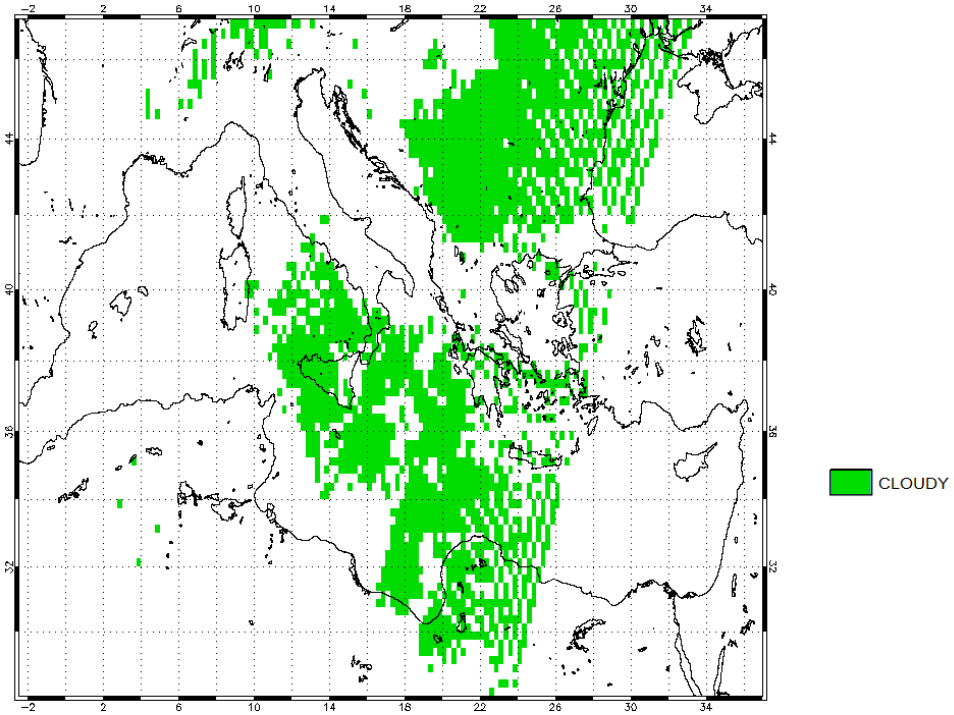

(a)

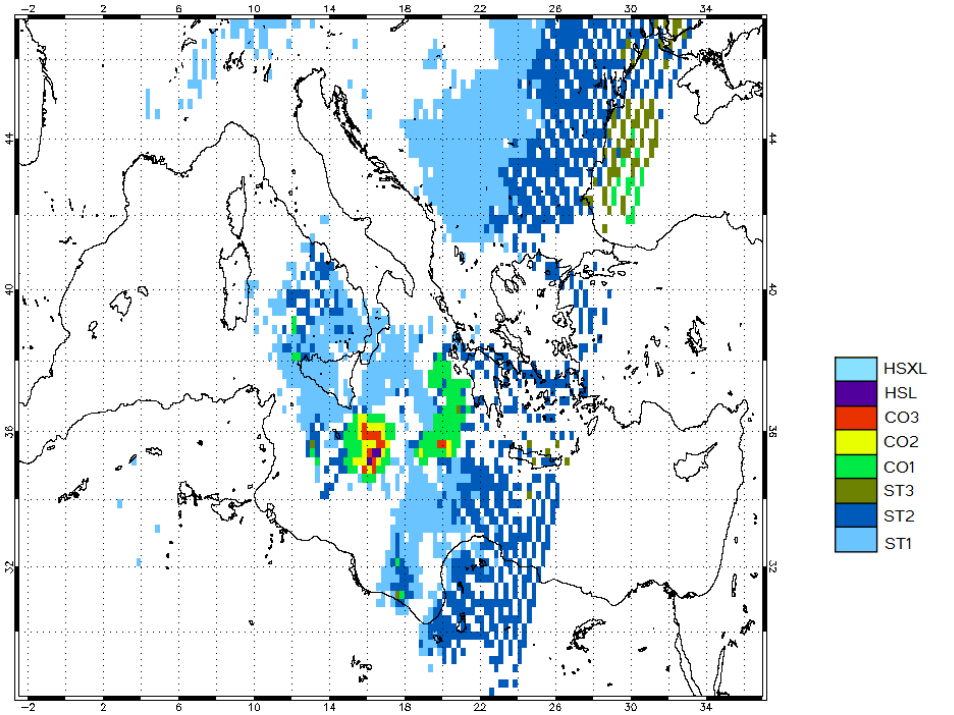

(b)

Figure 5.13: MW CMa (b) and MWCC (c) remapped for the 2006/10/16 event.

5.2 CLOUD MASK INTER-COMPARISON

The first stage of the analysis concerns the cloud mask comparison through the use of the dichotomous statistic, the aim of which is to reveal if the different cloud detection methods are in agreement or not and to what extent.

In order to apply this kind of statistics to the present analysis, it is necessary to establish which of the two methods will guide the comparison, then the response of which will be taken as truth. For this purpose, the SAFNWC software package is chosen, due to the wide range of evaluations and tests that have been already carried out on it [e.g. *Dybbroe et al.* (2001); *Derrien and Le Gléau* (2005); *Derrien* (2012)]. The role of the software to be tested, instead, is covered by the MWCC algorithm, which, as still under review, does not present yet any kind of validation document in support.

Then, for each case study, the cloud mask obtained by the MWCC algorithm and the one produced by the SAFNWC software, are compared, and, by using the obtained dichotomous indexes, the statistical parameters (equations 3.2-3.7) are calculated. Finally, the results obtained from the CMa inter-comparison for each case study are summarized in table 5.1 together with the total scores.

Table 5.1: Cloud Mask inter-comparison results.

Events	*Hits*	*Misses*	*False Alarms*	*Correct Negatives*	*Total*	ACC	BIAS	POD	FAR	POFD	HSS
2004/05/27 - 20:32	1436	457	1303	3242	6438	0,73	1,45	0,76	0,48	0,29	0,42
2004/11/07 - 12:47	2926	1313	424	1990	6653	0,74	0,79	0,69	0,13	0,18	0,48
2004/11/07 - 16:14	2938	651	765	1972	6326	0,78	1,03	0,82	0,21	0,28	0,54
2006/07/03 - 10:18	363	580	453	1915	3311	0,69	0,87	0,38	0,56	0,19	0,20
2006/07/03 - 12:33	591	598	365	2421	3975	0,76	0,80	0,50	0,38	0,13	0,39
2006/10/16 - 04:54	1396	1151	653	3247	6447	0,72	0,80	0,55	0,32	0,17	0,39
2014/09/05 - 08:36	1677	765	609	3443	6494	0,79	0,94	0,69	0,27	0,15	0,54
2015/01/22 - 19:28	1062	2055	52	1662	4831	0,56	0,36	0,34	0,05	0,03	0,25
Total	**12389**	**7570**	**4624**	**19892**	**44475**	**0,73**	**0,85**	**0,62**	**0,27**	**0,19**	**0,44**

By examining the cumulative data produced, it is observed that the two software are in a fair agreement about the detection of cloud presence or absence (HSS = 0.44). In detail we find that the ACC value is, in general, pretty good and, therefore, there is a notable amount of correct detection, or rather of pixels classified as cloudy or cloud free according to both softwares.

The number of misses, however, results fairly high as it can be seen by observing the BIAS, which approaches, but does not reach the perfect score, and the POD value, which is not exactly optimal. Actually, the latter parameter decrease is mainly due to two cases which will be treated in the following. Both the POD and BIAS results prove that the MWCC algorithm tends to underestimate the presence of cloud if

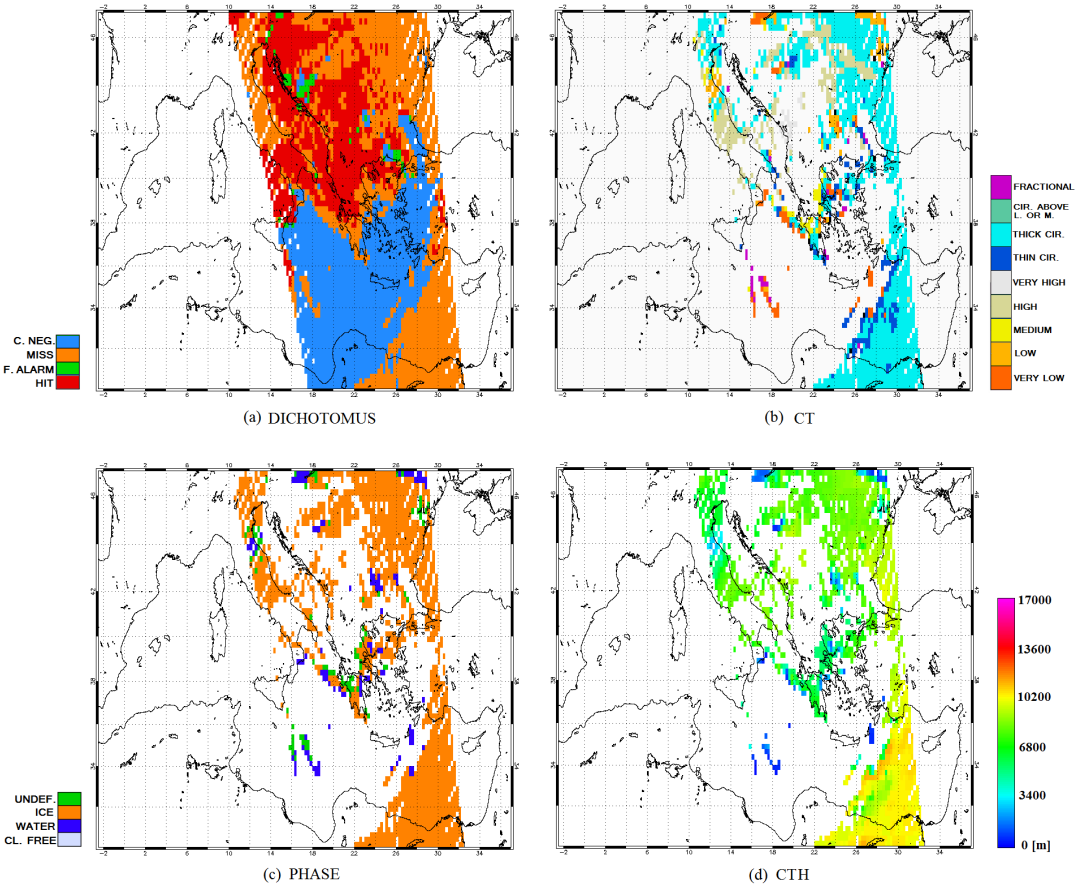

Figure 5.14: Analysis on the nature of misses pixels on the 2015/01/22 scene. Map of the contingency table parameters (a), SAFNWC Cloud Type (b), Cloud Phase (c), and Cloud Top Height (d) only for the missed cells.

compared with the SAFNWC software or, in other words, that there is a fair amount of areas evaluated as free by the MW classifier, but cloudy according to the PGE01 outcome.

The amount of false alarms, i.e. pixels ranked as cloudy by the MWCC, but free according to the other software, is generally lower than the number of misses, as evidenced by the FAR and POFD values, but still significant.

Even taking into account a small time lag between the scene acquisition time of AMSU-B/MHS and SEVIRI, and an uncertainty due to the loss of detail resulting from the data degradation, it still remains a certain predominance of misses and false alarms. Then, we are going to investigate further to understand what kind of clouds populate these two categories.

5.2.1 *Cloud Mask Misses*

From table 5.1 it is evident that the greater predominance of misses refers to the January 2015 event. In this particular case, therefore, it is interesting to understand

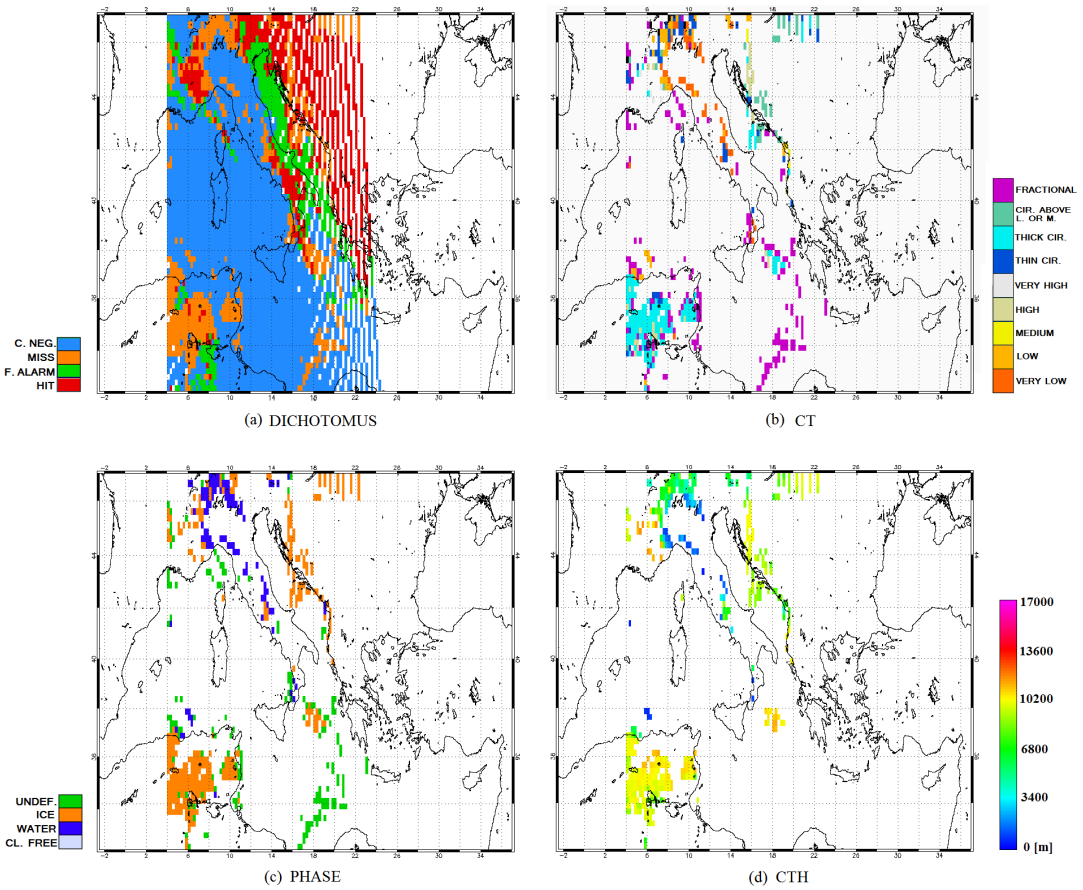

(a) DICHOTOMUS (b) CT

(c) PHASE (d) CTH

Figure 5.15: As in figure 5.14 for the 2006/07/03 12:33 UTC case study.

how the dichotomous categories are geographically distributed and, only for the misses, what is the corresponding classification in terms of cloud type, phase and top height. For this purpose, a map displaying the dichotomous analysis results, is created and put side by side to the aforesaid SAFNWC products (figure 5.14). Through this totally qualitative examination appears that, most of the pixels not detected as cloudy by the MWCC but classified as such by the SAFNWC, correspond to high, semitransparent, ice clouds, i.e. cirrus clouds. In addition, however, a further small set of misses pixels, is formed by a high opaque cloud system located above the central Apennines.

Another interesting scene to be analysed, is the one of July 2006 (12:33 UTC). This latter catches, among the other systems, the final stage of the flood-inducing event off the Ionian Calabria coast, which consists of frozen high clouds, figures 5.15(c)-5.15(d), and in particular, of a small Altostratus and a wider area covered by thick cirrus to be observed in figure 5.15(b). Such type of clouds, is not detected by the MW algorithm, just as it happens for the cirrus clouds above northern Africa and for the low water clouds set in north-central Italy. This can be seen in panel (a) of figure 5.15.

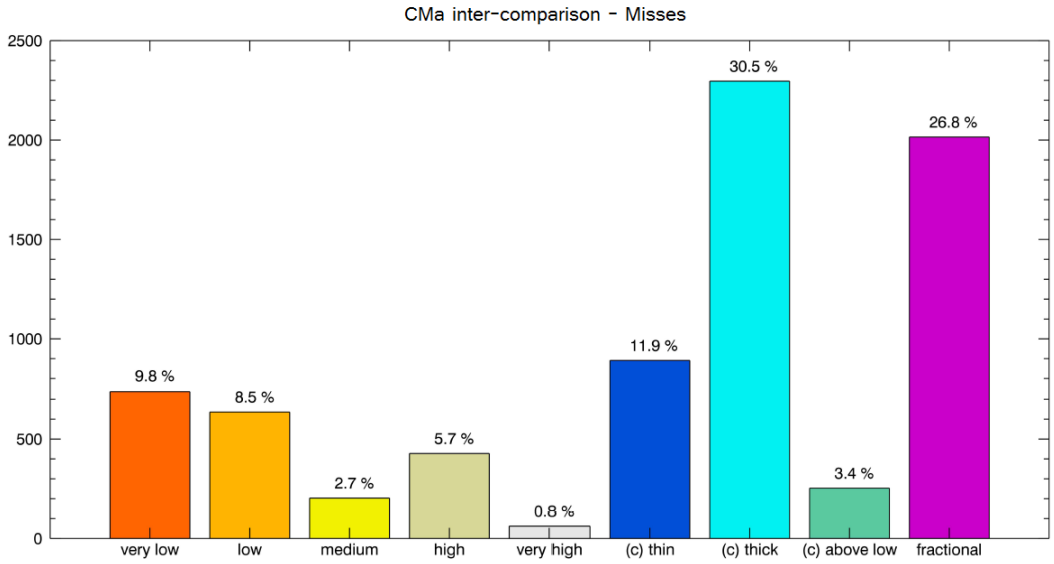

Figure 5.16: The histogram summarizes the results of a numerical analysis intended to figure out what kind of cloud the MWCC algorithm fails to reveal. On the x-axis are the SAFNWC CT categories held after the remapping (please observe that the (c) distinguishes the three cirrus cloud classes), along the y-axis is the number of occurrences and, finally, in correspondence of each category the percentage calculated over the total number of pixels flagged as misses, is shown.

Thus, based on an examination of these specific cases, it appears that the microwave algorithm misses mostly in the cirrus clouds detection and presents some problems also in case of the fractional, low and high opaque clouds.

In order to get a numerical assessment on the cloud types populating the class of misses arising from the cloud mask comparison, a focused study, involving all of the cases, is performed and summarized in the histogram of figure 5.16. This latter provides a detailed numerical information about the SAFNWC cloud type associated to MWCC missed grid cells.

The first thing we can observe is, precisely, a large percentage of thick cirrus: this category covers the 30.5% of the total missed pixel number. This matter is not entirely unexpected, in fact, even if all the AMSU-B/MHS channels are influenced by ice particles in thick cirrus clouds [*Buehler et al.* (2007); *Hong et al.* (2005b)], the MWCC algorithm is not conceived to detect this cloud type, i.e. cirrus clouds with no other cloud deck beneath them.

Nevertheless, considering separately daytime and night-time/twilight scenes as in figures 5.17(a)-5.17(b), it is evident that a certain amount of thick cirrus could be due to cirrus above low or medium clouds, which in low lighting conditions can not be detected due to the lack of the necessary SEVIRI channels able to do this. Actually in daylight the number of thick cirrus drastically decreases (4.6%), while the greatest contribution to the observed percentage in the cumulative study, is given by nighttime or twilight events (26.0%).

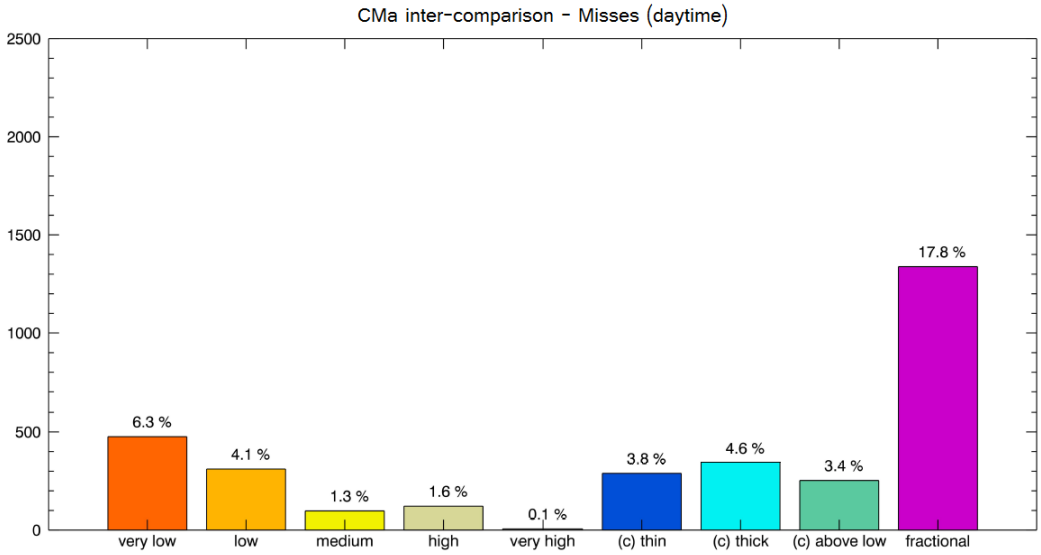

(a) Daytime

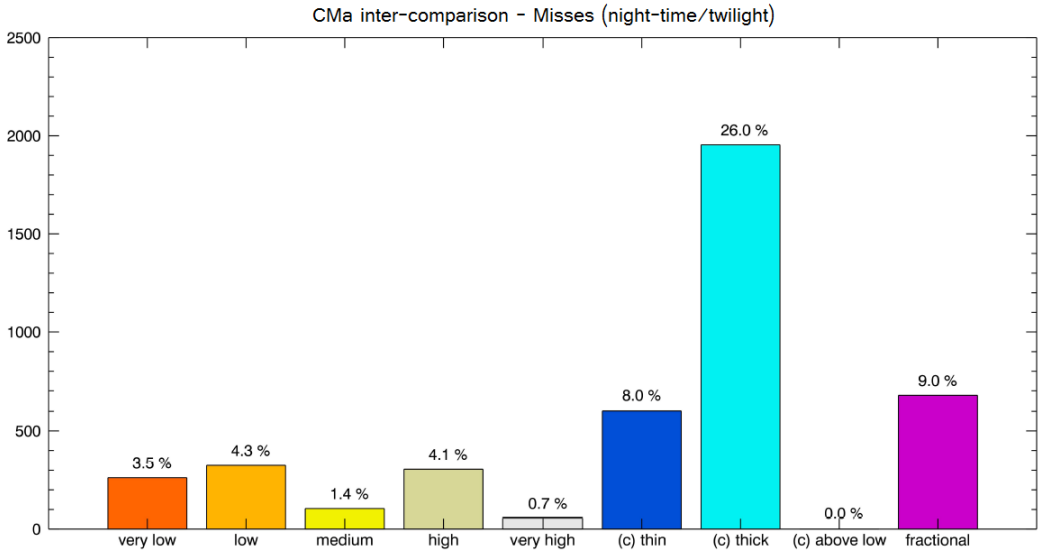

(b) Night-time/Twilight

Figure 5.17: The same as in figure 5.16 for daytime (a) and for the remaining night-time/twilight cases (b). For the subdivision between these two scene categories, see table 4.2.

On the other hand multi-layer system (i.e. cirrus above low or medium clouds) are often not detected, because cloud layers below cirrus are characterized by a medium height and thus are not identified by the MWCC algorithm, usually starting the cloud classification process from lower layers (1-2 km, see section 3.2.2).

As regards the thin cirrus, instead, this kind of clouds have a very small influence on the brightness temperatures at AMSU-B/MHS frequencies [*Hong et al.* (2005b)]. Therefore, most probably the reported 11.9%, depends on it.

As it can also be seen in the examined histogram, the fractional clouds are another category very often missed by the MW detection algorithm (26.8%). Note, however, that this class is primarily constituted by cloud edges and, thus, the high MWCC failure percentage is quite normal if the remarkable attitude of the MW to penetrate too thin or broken clouds is considered and compared to the VIS/IR one.

In terms of numbers, very low and low clouds follow. Due to the way the height ranges of the MWCC classes have been studied, the algorithm should start to work from 1 km altitude. This value, however, is widely affected by a number of factors, such as the ground and the atmospheric temperature and, therefore, by the season and the time throughout the day. In fact, the colder the surface becomes, the more water vapour tends to condense downwards and, therefore, the weighting functions peak lower. If, however, the surface is warmer, the opposite occurs and, consequently, the weighting functions rise up, ensuring the first layer the algorithm is able to reveal is higher than 1-2 km height. For this reason, some low and very low clouds may be invisible to the MW software detection.

Furthemore, as already fully explained, the MWCC algorithm has been designed for the study of convective systems rising from the lower atmospheric layers and then continuing to extend in height. For this reason, it is not able to reveal stratiform isolated systems. Thus, citing again this motivation, it is finally possible to explain the medium, high and very high cloud percentages, whose presence is not absolutely reveled by the MW algorithm (always supposing these formations stand above completely free atmospheric layers).

5.2.2 *Cloud Mask False Alarms*

Although the false alarm number, provided in output from the statistical dichotomous analysis, is lower than the misses one, even in this case it is interesting to comprehend what kind of cloud category makes up the pixels at issue. Therefore, a study has been conducted by calculating the percentage of pixels belonging to each of the tested algorithm classes and flagged as false alarms .

By observing the results shown in figure 5.18, it is clear that the MW software tends to overestimate the presence of stratiform systems ranged between 1 and 4 km, categorized in the ST1 and ST2 classes.

These cloud classes, especially ST1, are fairly uncertain classes, usually exploited with the only purpose to be able to move on the classification of the next cloud levels, or the convective ones. It means that an increasing of the water vapour amount in

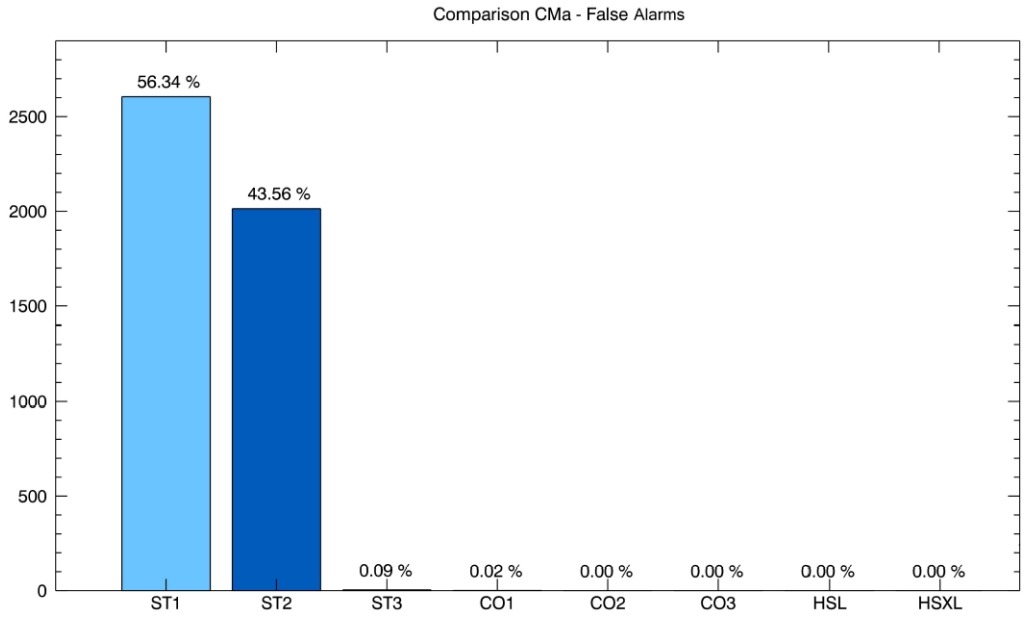

Figure 5.18: The histogram identifies the cloud type that the MWCC reveals where, at the same time, the SAFNWC provides a cloud free outcome. On the x-axis are the MWCC cloud type classes, along the y-axis is the number of occurrences and, finally, in correspondence of each category the percentage calculated over the total number of pixels flagged as false alarms, is shown.

the lower atmosphere can be misinterpreted and then wrongly flagged as very low cloud.

Nevertheless there is also another way of interpreting the present study results: these could be due to an underestimation of the actual cloud cover by the SAFNWC CMa processing algorithm. It is proved that there may be problems in the low cloud detection in case of low solar elevation, over both land and sea [*Derrien and Le Gléau* (2005); *Derrien* (2013)]. Furthemore, it may also happen that large areas of low clouds, over land, are not detected in night-time conditions in the so-called warm sectors[3], but also in areas viewed with high satellite zenith angles or if the low clouds are surmounted by very thin cirrus [*Derrien* (2013)].

All of this happens because the radiances recorded in the different sensor channels and then processed by the software, can be misinterpreted in the aforementioned conditions, and also because certain channels are entirely lacking in a poor illumination state. This can lead to a non detection of the considered clouds and produce, thus, the observed false alarms.

Subsequently, if such study is also repeated by separating the diurnal scenes from the nocturnal or twilight ones (see table 4.2), the percentage of false alarms observed in the latter and illustrated in figure 5.19(b), can be explained most likely in this manner. Note again that, though the difference with the daylight analysis of figure

3 wedges of warm air between the warm and cold fronts of a depression, which is eventually occluded [*Collins English Dictionary*].

5.19(a) is not really marked, the low lighting conditions generate a higher percentage of pixels belonging to such dichotomous class.

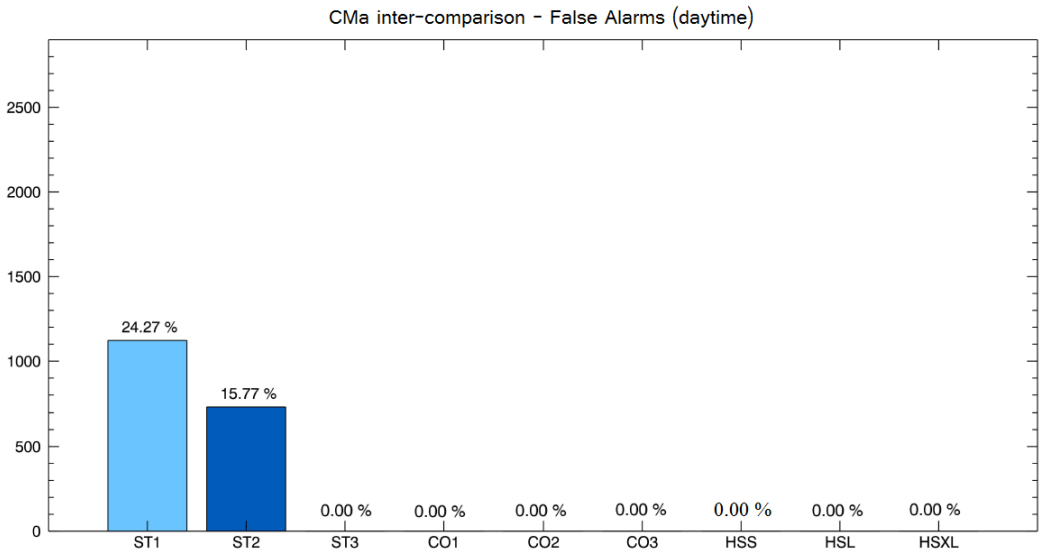

(a) Daytime

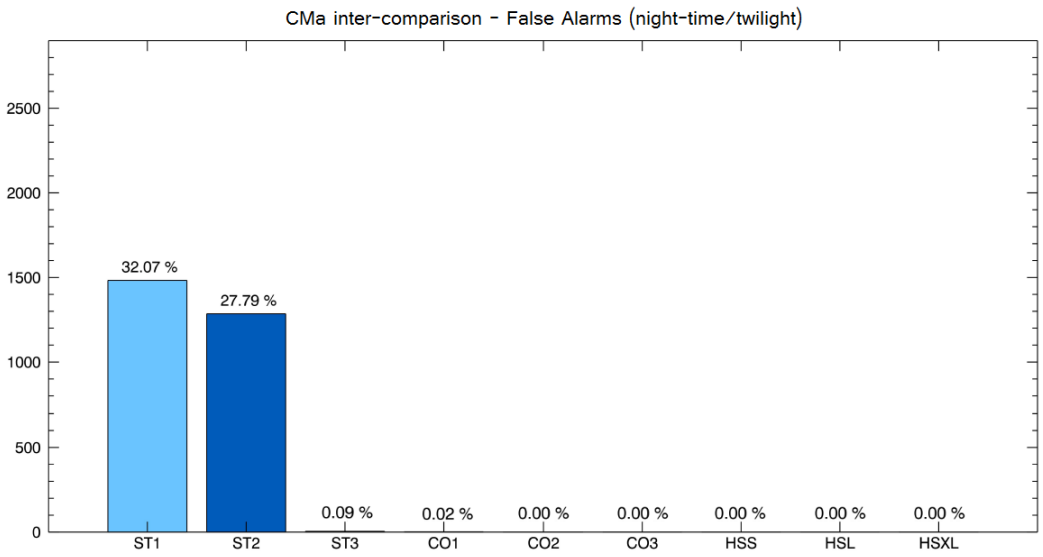

(b) Night-time/Twilight

Figure 5.19: The same as in figure 5.18 for the daytime (a) and night-time/twilight (b) cases.

5.3 CLOUD CLASS INTER-COMPARISON

After dealing with any relevant consideration about the misses and false alarms arised from the cloud mask inter-comparison, the focus is now on the pixels belonging to the hits category. These have been classified by either of the two softwares as cloudy pixels, but no information on the cloud type of such areas has been provided through the work carried out so far. Therefore, the aim of this section is to perform an inter-comparison between the cloud type provided by the classification methods for each pixel identified as cloudy according to both. This is to understand whether the results obtained by two classification methods, working on different parts of the electromagnetic spectrum, are comparable or not and to what extent.

In carrying out such investigation, in order to make the comparison fair without giving priority to a software at the expense of the other, the SAFNWC fractional cloud class will not be taken into account, since it is mainly constituted by cloud edges to which the MW sensors are not sensitive. Finally, given the particular nature of the semitransparent high clouds, these will be dealt apart from the opaque ones.

5.3.1 *Semitransparent High Clouds - Cirrus Clouds*

By developing a strategy in order to compare as well as possible the different kind of results, it is observed that, among the MWCC classes the semitransparent ice clouds (i.e. the cirrus clouds) are not retrieved, even if these are supplied among the SAFNWC output. So we wonder which cloud type, and to what extent, the microwave based software provides in correspondence to the pixels classified as cirrus clouds by means of the visible and infrared method.

By performing such a cross comparison on all the available cases, it appears that, where the SAFNWC senses a cirrus cloud, the MWCC selects one among its first four categories: ST1, ST2, ST3 and CO1. This can be observed in the histogram of figure 5.20(a) and at the first rows of the tables 5.2, which summarize the results of the study.

Let us start by considering the cirrus above low or medium cloud category. The coincidence of such a type of system with the lowest MWCC classes, is easy to be justified. In effect, this algorithm can not detect high clouds if these are significantly separated from the overlying ones, but it is designed to sense what lies beneath. Therefore, the occurrence of ST1 and ST2, followed by the less populated CO1 and ST3, suggests that, actually, the MW algorithm may have detected the underlying formations.

Moving on to deal with the more interesting thick cirrus category, it is possible to observe that its equivalent in the microwave context is a large amount of pixels flagged as ST2 and ST1. Although the microwaves are sensitive to the ice particles that constitute such a kind of semitransparent clouds, the detection mechanism described above, also applies to this matter. Thus, once again, this suggests that the methods have recognized different cloud levels: the SAFNWC tools have recorded the

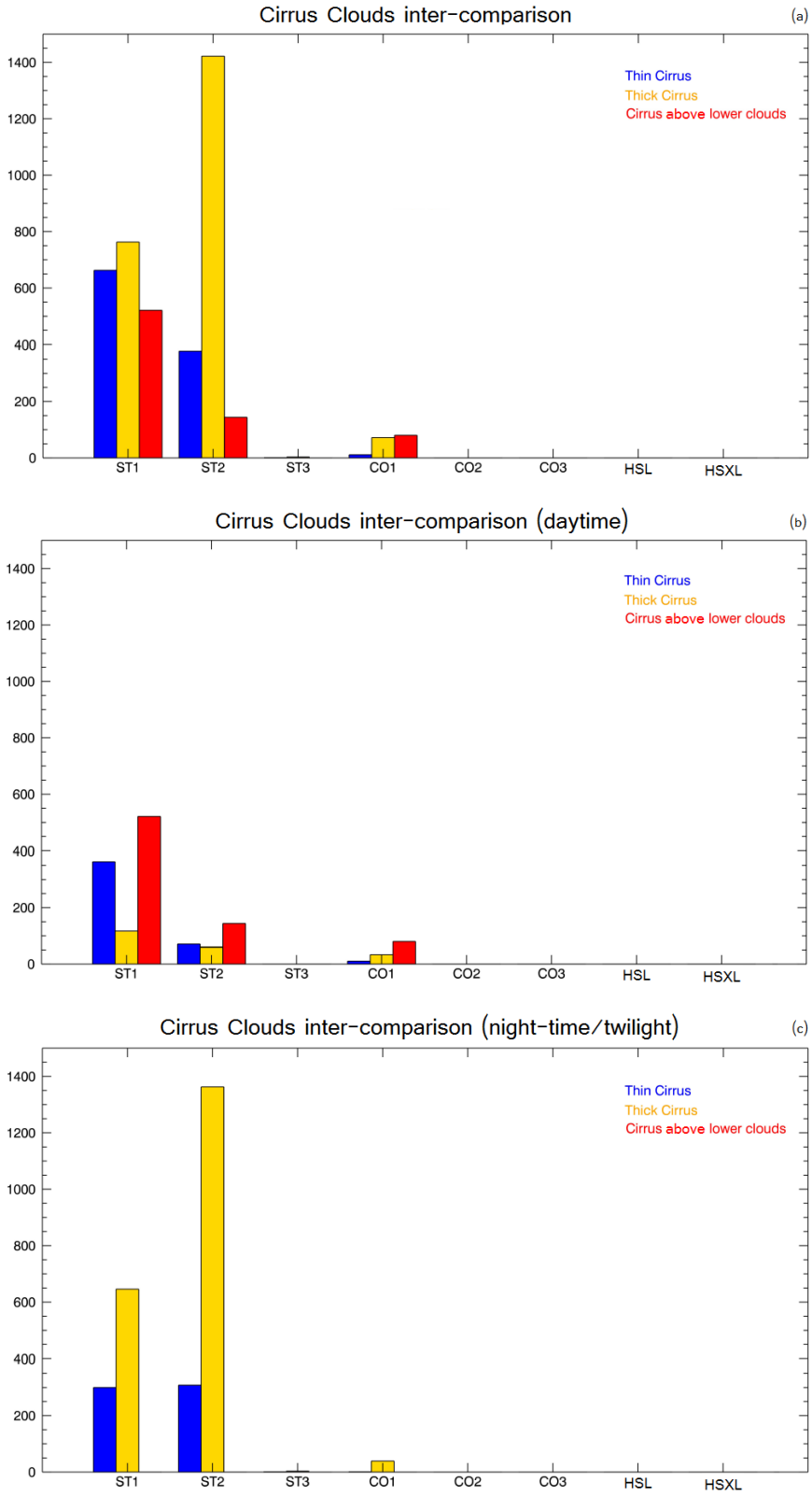

Figure 5.20: Cirrus cloud inter-comparison executed for all of the case studies (a) and then by using only the daytime (b) or night-time/twilight scenes (c). On the y-axis is the number of occurrences of each MWCC cloud type reported on the x-axis. The study has been performed for the three SAFNWC cirrus cloud categories, each shown with a different color.

	Cirrus above Low or Medium Clouds			
	ST1	ST2	ST3	CO1
Cumulative	521	144	0	80
Daytime	521	144	0	80
Twilight/Nigth-time	–	–	–	–

	Thick Cirrus			
	ST1	ST2	ST3	CO1
Cumulative	763	1422	3	72
Daytime	117	59	0	33
Twilight/Nigth-time	646	1363	3	39

	Thin Cirrus			
	ST1	ST2	ST3	CO1
Cumulative	663	379	1	11
Daytime	363	71	0	10
Twilight/Nigth-time	300	308	1	1

Table 5.2: Numerical results for each cirrus cloud class deriving by the involved inter-comparison and reporting, in terms of exploited scenes, the number of pixels attributed to each MWCC cloud category. Observe about this, that only the firts four classes of the microwave based algoritm has been reported, beacuse the other four gave null results.

high cirrus clouds, rather the MWCC algorithm has revealed the lower atmospheric layer content.

However, since the SAFNWC CT algorithm can identify multi-layer cloud systems only during daytime, also in this case the behavior of the two cloud classification methods is analysed by separating daytime and night-time/twilight events.

By considering the outcome reported in figures 5.20(b)-5.20(c) and summarized in tables 5.2 it is evident that during daytime, when it is possible to identify the multi-layer systems, the number of ST2 is drastically reduced, while the biggest contribution to the total amount, is given by the low solar elevation scenes. Therefore, it is reasonable to think that all the ST2 clouds corresponding also to this SAFNWC cloud type, actually are justified by the presence of stratified systems unclassified in night-time/twilight illumination condition for lack of channels or uncertainty on the evaluation, as documented by *Derrien* (2013).

The same behaviour is displayed by the ST1 category, even if this is a very uncertain class since it tends, in general, to be overestimated and evaluated with a low reliability.

That said, we can finally concentrate on the thin cirrus cloud class. While doing this, it is necessary to remember that the microwave sensors, due to the strong power to penetrate most cloud layer at these frequencies, are absolutely unable to reveal the presence of any cloud type with such a limited thickness.

Then, even in this case, the question is entirely analogous to that just faced for the previous cirrus class. The only difference is that the possibility of making an isolated and high cloud detection, is not precluded by a limitation of the algorithm, but by a physical feature on which this is based.

As a consequence, by analyzing the numerical data listed in table 5.2 and again the histograms in figure 5.20, it is evident that, the ST2 category is much lowered in the daytime study, due to the presence of the multylayer system measurement, rather the ST1 is slightly less reduced, for the reasons already explained above. Compared to the thick cirrus class, however, the contribution to the cumulative outcome is almost evenly coming both from the daytime scenes and from those characterized by a lower solar elevation.

5.3.2 *SAFNWC Opaque Clouds vs MWCC Cloud Classes*

After discussing the cirrus matter, we can move on to devise a strategy aimed to establish the relationship among the cloud type outputs provided by the examined softwares. To this purpose, we proceed by observing that every MWCC cloud category is defined through a specific range of cloud top altitudes. Similarly even the SAFNWC opaque cloud types can be associated to coarse ranges of height. Therefore we try to pair the classes obtained by such working on different physical base methods, in order to perform on each couple an analysis by means of the dichotomous statistics. This will be helpful to discover whether the cloud type outputs are comparable or not, also allowing to get some more information on the MWCC algorithm which, in this work, finds its first numerical validation.

Then, according to the scheme reported in figure 5.21, the most suitable matches are the following:

- Very Low vs ST1;
- Low vs ST2;
- Medium vs ST3 and CO1;
- High vs CO2;
- Very High vs CO3, HSL and HSXL.

Using the SAFNWC classes as the leading ones, the statistical study is performed and the results thus produced, event by event and pair by pair, are given in tables

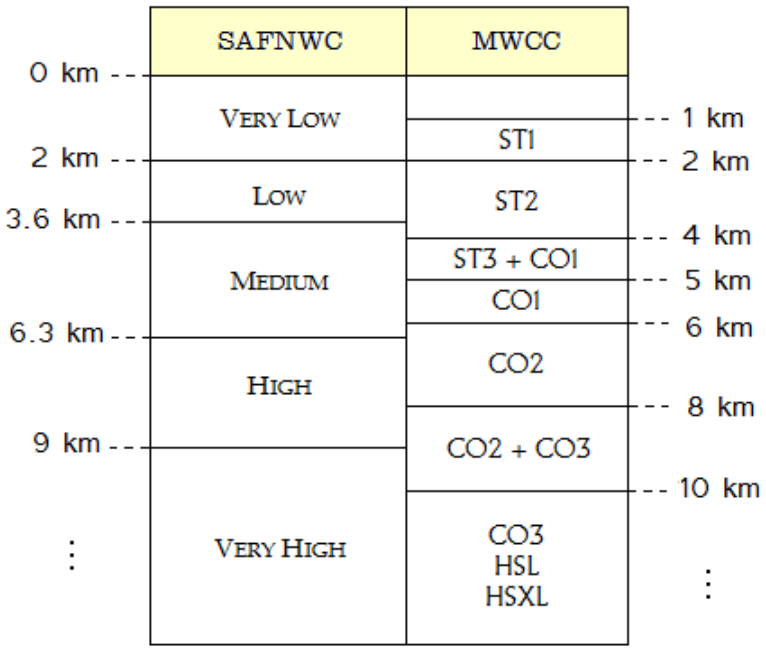

Figure 5.21: Schematic description of the cloud type classes provided in output from the SAFNWC software and the MWCC algorithm, in which the limits of the height ranges are underlined.

5.3-5.7. Then, for a summary overview on the dichotomous study outcome, see also the histogram in figure 5.22.

When comparing the two classes located at the lowest altitude, that is the Very Low and ST1, a strong tendency of the MWCC to overestimate the presence of ST1 clouds emerges. Both BIAS and FAR values, in fact, inform of the conspicuous presence of false alarms. The POD parameter, even if not optimal, is anyway the highest if compared to the outcome related to the other class couples. The cumulative HSS value is indicative of a poor concordance between the involved methods.

Almost the same behaviour is found for the Low and ST2 classes. Indeed, although less pronounced than in the previous case due to the growth in the number of misses, an overestimation of the MWCC cloud class is shown. The accuracy, on the other hand, is further decreased and the general trend showed by the HSS values, is of a quite poor agreement.

Dealing with the next comparison between the Medium clouds and the ST3-CO1, a net change is revealed with a sharp increase in the missed cases. As a consequence the MWCC tendency is to underrate the presence of its two classes with respect to the Medium clouds detected by means of the SAFNWC tools. By contrast the pixels classified as hits are very few, as even evidenced by the POD parameter value.

As regards the High vs CO2 study results, a fair disagreement between the outputs is underlined by the HSS typically negative values. There is again a tendency of the VIS/IR classification algorithm to attribute the questioned class flag to many more pixels if compared to those provided by the other software. The statistical parameters indicate, in fact, a considerable increase of the misses pixels to the detriment of those

Table 5.3: Very Low vs ST1.

Events	Hits	Misses	False Alarms	Correct Negatives	Total	ACC	BIAS	POD	FAR	POFD	HSS
2004/05/27 - 20:32	5	15	49	465	534	0,88	2,70	0,25	0,91	0,10	0,09
2004/11/07 - 12:47	138	1	905	469	1513	0,40	7,50	0,99	0,87	0,66	0,09
2004/11/07 - 16:14	9	1	248	1086	1344	0,81	25,70	0,90	0,96	0,19	0,05
2006/07/03 - 10:18	2	30	1	236	269	0,88	0,09	0,06	0,33	0,00	0,10
2006/07/03 - 12:33	30	12	20	312	374	0,91	1,19	0,71	0,40	0,06	0,60
2006/10/16 - 04:54	18	25	375	525	943	0,58	9,14	0,42	0,95	0,42	0,00
2014/09/05 - 08:36	57	11	341	675	1084	0,68	5,85	0,84	0,86	0,34	0,15
2015/01/22 - 19:28	3	12	67	563	645	0,88	4,67	0,20	0,96	0,11	0,03
Total	**262**	**107**	**2006**	**4331**	**6706**	**0,68**	**6,15**	**0,71**	**0,88**	**0,32**	**0,11**

Table 5.4: Low vs ST2.

Events	Hits	Misses	False Alarms	Correct Negatives	Total	ACC	BIAS	POD	FAR	POFD	HSS
2004/05/27 - 20:32	119	30	255	130	534	0,47	2,51	0,80	0,68	0,66	0,09
2004/11/07 - 12:47	5	282	422	804	1513	0,53	1,49	0,02	0,99	0,34	-0,28
2004/11/07 - 16:14	85	106	887	266	1344	0,26	5,09	0,45	0,91	0,77	-0,12
2006/07/03 - 10:18	65	5	41	158	269	0,83	1,51	0,93	0,39	0,21	0,62
2006/07/03 - 12:33	41	26	38	269	374	0,83	1,18	0,61	0,48	0,12	0,46
2006/10/16 - 04:54	90	204	243	406	943	0,53	1,13	0,31	0,73	0,37	-0,07
2014/09/05 - 08:36	299	228	341	216	1084	0,48	1,21	0,57	0,53	0,61	-0,04
2015/01/22 - 19:28	37	22	383	203	645	0,37	7,12	0,63	0,91	0,65	-0,01
Total	**741**	**903**	**2610**	**2452**	**6706**	**0,48**	**2,04**	**0,45**	**0,78**	**0,52**	**-0,05**

Table 5.5: Medium vs ST3 and CO1.

Events	Hits	Misses	False Alarms	Correct Negatives	Total	ACC	BIAS	POD	FAR	POFD	HSS
2004/05/27 - 20:32	10	127	95	302	534	0,58	0,77	0,07	0,90	0,24	-0,18
2004/11/07 - 12:47	1	277	39	1196	1513	0,79	0,14	0,00	0,98	0,03	-0,04
2004/11/07 - 16:14	0	350	94	900	1344	0,67	0,27	0,00	1,00	0,09	-0,12
2006/07/03 - 10:18	38	6	116	109	269	0,55	3,50	0,86	0,75	0,52	0,17
2006/07/03 - 12:33	50	16	188	120	374	0,45	3,61	0,76	0,79	0,61	0,07
2006/10/16 - 04:54	34	324	144	441	943	0,50	0,50	0,09	0,81	0,25	-0,17
2014/09/05 - 08:36	5	241	38	800	1084	0,74	0,17	0,02	0,88	0,05	-0,04
2015/01/22 - 19:28	1	132	130	382	645	0,59	0,98	0,01	0,99	0,25	-0,25
Total	**139**	**1473**	**844**	**4250**	**6706**	**0,65**	**0,61**	**0,09**	**0,86**	**0,17**	**-0,09**

Table 5.6: High vs CO_2.

Events	Hits	Misses	False Alarms	Correct Negatives	Total	ACC	BIAS	POD	FAR	POFD	HSS
2004/05/27 - 20:32	1	183	0	350	534	0,66	0,01	0,01	0,00	0,00	0,01
2004/11/07 - 12:47	0	705	3	805	1513	0,53	0,00	0,00	1,00	0,00	0,00
2004/11/07 - 16:14	0	668	13	663	1344	0,49	0,02	0,00	1,00	0,02	-0,02
2006/07/03 - 10:18	2	113	1	153	269	0,58	0,03	0,02	0,33	0,01	0,01
2006/07/03 - 12:33	1	177	6	190	374	0,51	0,04	0,01	0,86	0,03	-0,03
2006/10/16 - 04:54	0	143	23	777	943	0,82	0,16	0,00	1,00	0,03	-0,04
2014/09/05 - 08:36	1	236	1	846	1084	0,78	0,01	0,00	0,50	0,00	0,00
2015/01/22 - 19:28	6	323	7	309	645	0,49	0,04	0,02	0,54	0,02	0,00
Total	**11**	**2548**	**54**	**4093**	**6706**	**0,61**	**0,03**	**0,00**	**0,83**	**0,01**	**-0,01**

Table 5.7: Very High vs CO_3, HSL and HSXL.

Events	Hits	Misses	False Alarms	Correct Negatives	Total	ACC	BIAS	POD	FAR	POFD	HSS
2004/05/27 - 20:32	0	44	0	490	534	0,92	0,00	0,00	–	0,00	0,00
2004/11/07 - 12:47	0	104	0	1409	1513	0,93	0,00	0,00	–	0,00	0,00
2004/11/07 - 16:14	8	117	0	1219	1344	0,91	0,06	0,06	0,00	0,00	0,11
2006/07/03 - 10:18	3	5	0	261	269	0,98	0,38	0,38	0,00	0,00	0,54
2006/07/03 - 12:33	0	21	0	353	374	0,94	0,00	0,00	–	0,00	0,00
2006/10/16 - 04:54	16	89	0	838	943	0,91	0,15	0,15	0,00	0,00	0,24
2014/09/05 - 08:36	1	5	0	1078	1084	1,00	0,17	0,17	0,00	0,00	0,28
2015/01/22 - 19:28	6	103	5	531	645	0,83	0,10	0,06	0,45	0,01	0,07
Total	**34**	**488**	**5**	**6179**	**6706**	**0,93**	**0,07**	**0,07**	**0,13**	**0,00**	**0,11**

Notice that the "–" sign is used whenever, during the calculation, the denominator results null and, therefore, the division operation becomes meaningless.

flagged as false alarms. On the other hand, the hits are very low in number and this reflects on a very bad POD value. The POFD is low due to the large population of the correct negatives category with respect to false alarms one.

Finally, the cross check of the last classes, i.e. Very High against CO_3-HSL-HSXL, demonstrates, once again, the predominance of pixels belonging to the misses category. The hits are really very few and the false alarms even less. Moreover, since the study has been performed on each pixel classified as cloudy, but the greatest contribution to the total is given by the correct negatives, the ACC value is pretty high. The general trend of the HSS values shows a slightly better agreement between the two methods than the three previous categories.

In summary, the overall observed tendency of the MWCC method, with respect to the SAFNWC one, is an overestimation of the first cloud classes, ST_1 and ST_2. This

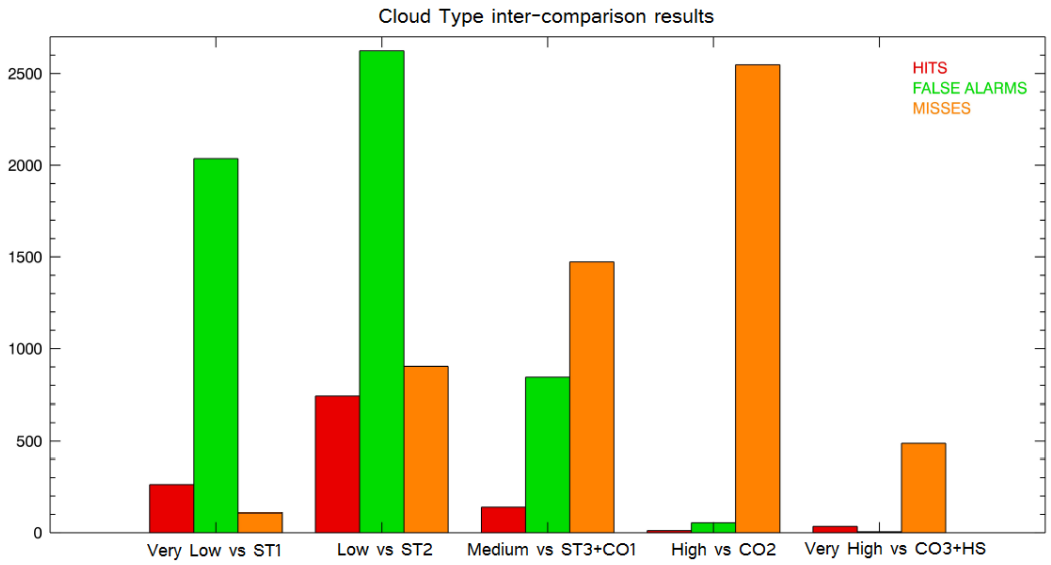

Figure 5.22: Summary of the study results produced by means of the dichotomous statistic applied to every compared class pairs. Note that the "correct negatives" category is not reported in the current histogram because too populated than the others and this would have resulted in the flattening of the remaining categories, not allowing an easy reading.

trend is reversed with the increasing altitude, or rather there is a misses increase at the expense of the false alarms, reaching its maximum in case of High Clouds.

In other words, the lower is the cloud top, the more MWCC seems to be able to detect it. Viceversa, the more the cloud top height increases, the more the MWCC does not reveal a certain cloud portion, rather detected by means of the SAFNWC tool.

It is also necessary to understand the nature of misses and false alarms, as already done in the cloud mask inter-comparison. It means that, for each compared pair of classes, we will analyse what kind of cloud populates such dichotomous categories.

The obtained results are illustrated in the histograms of figures 5.23 to 5.27. These show, in the false alarms matter, i.e. in correspondence with a specific MWCC algorithm response which disagrees with the matched SAFNWC product, the output provided by this latter. For example, where the MWCC detects a ST1 cloud type but SAFNWC disagrees, we are going to investigate which category this confers, and so on for each set against pair. Whereas, where the SAFNWC tool gives a known output, different by the corresponding MWCC one, so in the misses case, the kind of information which this is providing right there, is exposed. For each cloud class a recurrence percentage is also computed on the total number of miss or false alarm pixels, depending on the case.

The general trend emerging by looking at the false alarm values, indicates that the cloud top height achieved by means of the VIS/IR classification method, results higher than that determined by using the MW classifier. This occurs in every comparison between the chosen pairs, except for the very high clouds couple. In this case, in fact,

where the MWCC senses clouds belonging to its last three categories, the SAFNWC provides in output simply high clouds. However, these pixels are low in number and then of few relevance.

Just the opposite occurs in the misses istance. The MWCC method tends, in fact, to classify the questioned clouds by placing them at the lower levels than those assigned by the VIS/IR software, and never to higher ones. The only exception is the pair of lower clouds, where the SAFNWC detects the presence of Very Low clouds and instead the MWCC retrieves systems mainly belonging to the ST2 category. The number of pixels, however, is negligible if compared to those registered for the other comparisons.

In other words, with respect to the SAFNWC, the MWCC pushes down the cloud top height level. On the contrary, the SAFNWC cloud type outputs are shifted upwards with respect to those provided by the other examined software.

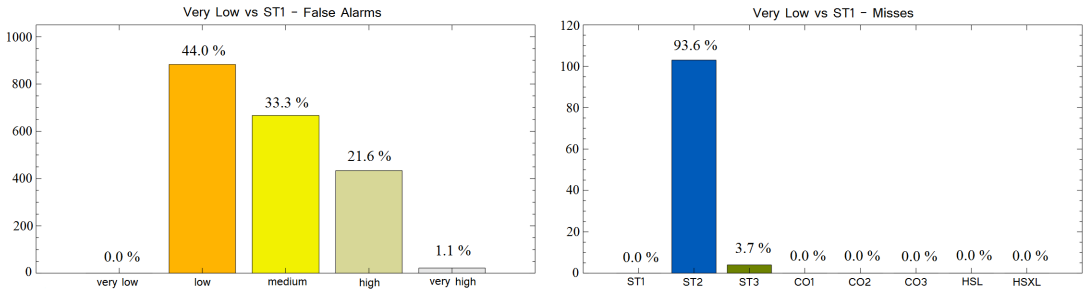

Figure 5.23: Very Low vs ST1 - False Alarms and Misses.

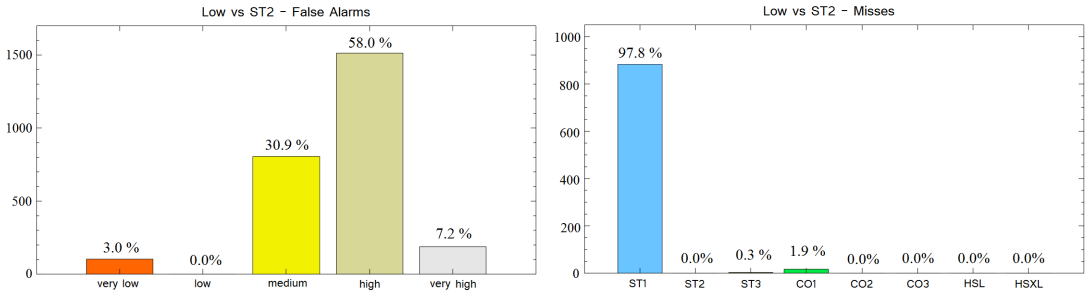

Figure 5.24: Low vs ST2 - False Alarms and Misses.

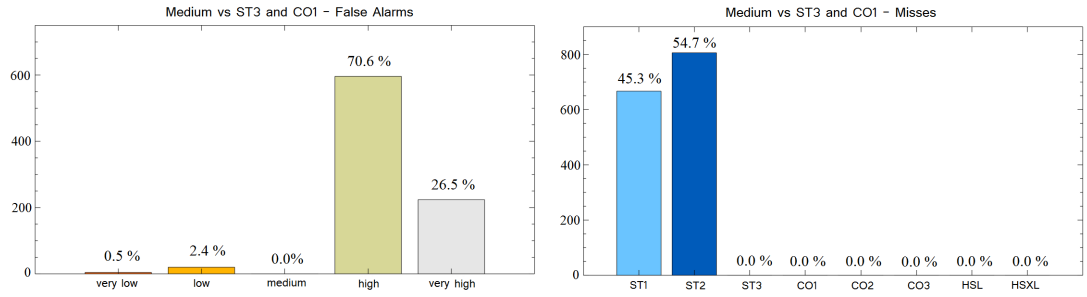

Figure 5.25: Medium vs ST3 and CO1 - False Alarms and Misses.

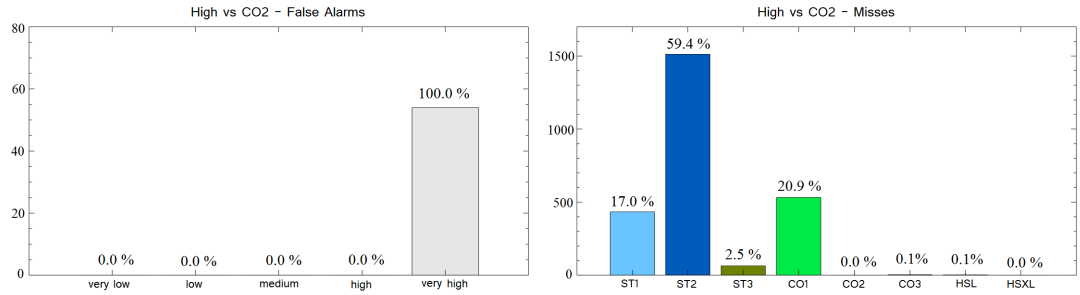

Figure 5.26: High vs CO_2 - False Alarms and Misses.

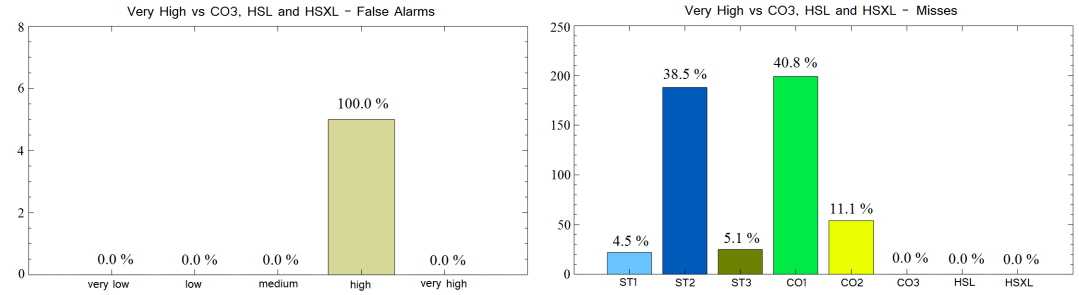

Figure 5.27: Very High vs CO_3, HSL and HSXL - False Alarms and Misses.

Overall, this behavior can be explained bringing up the different physical features on which the classification algorithms are based. The SEVIRI sensor, on which the SAFNWC package works, since has channels in the visible and infrared wavelengths, detects the cloud top properties by measuring the reflected or emitted radiation. In this way, it intercepts the first system starting at the top and often fails to see beyond that. The MWCC, on the other hand, being based on the microwave radiation frequencies, is very inclined to penetrate the cloud more than the former. In addition, this is designed to investigate the vertical structure of convective towers, reconstructing their development, layer by layer, and starting from the bottom. For this reason, it seems to show the opposite trend, lacking in identifying altostratus-cirrus formations which are not part of a deep cloud, but showing more sensitivity to the water vapour masses occupying the lower atmospheric layers, sometimes overrating that or incorrectly reading the radiances recorded by the used sensor.

5.3.3 *Height range investigation results*

Considering that the selected class pairs do not seem to fit well, it is thought that this partly might be due to an inaccurate choice of the couples in question. Therefore, in order to perform a more accurate and focused analysis, we decide to also test the height ranges which should be associated to MWCC by the use of the SAFNWC CTTH product.

In this way, referring again to figure 5.21 and by using the height ranges as the leading information, the pairs on which the dichotomic statistics is applied, are the following:

- 1-2 km vs ST1;
- 2-4 km vs ST2;
- 4-5 km vs ST3;
- 4-6 km vs CO1;
- 6-10 km vs CO2;
- > 8 km vs CO3, HSL and HSXL.

The results thus obtained are listed in the tables 5.8-5.13 and in the summary chart of figure 5.28. Note in this regard, that the pixel total amount, on which the study has been performed, is lower than in the cloud type previous analysis. In fact, some of the concerned pixels were flagged with a value of height equal to zero, indicating that no height value was available [*Derrien* (2013)]. This may be due to problems in the signal acquisition or in the treatment of the data. Anyway, such small areas have been excluded from comparison in order to make it more clean and reliable as possible.

The trend displayed in this case, is approximately the same encountered in the cloud type classes inter-comparison. The MW software seems to overestimate clouds at lower atmospheric levels, that is between 1 and 4 km, compared to the SAFNWC detections. This is shown in tables 5.8 and 5.9, by the high BIAS values and the poor result as regards the FAR parameter. On the other hand, the cumulative POD appears quite good in the ST1 issue, because the amount of hits compensates the misses one, but falls treating the ST2 category. In this case, in effect, the concordance between

Table 5.8: 1-2 km vs ST1.

Events	*Hits*	*Misses*	*False Alarms*	*Correct Negatives*	*Total*	ACC	BIAS	POD	FAR	POFD	HSS
2004/05/27 - 20:32	0	7	51	467	525	0,89	7,29	0,00	1,00	0,10	-0,02
2004/11/07 - 12:47	40	0	993	470	1503	0,34	25,83	1,00	0,96	0,68	0,02
2004/11/07 - 16:14	4	1	248	1085	1338	0,81	50,40	0,80	0,98	0,19	0,02
2006/07/03 - 10:18	0	9	3	251	263	0,95	0,33	0,00	1,00	0,01	-0,02
2006/07/03 - 12:33	9	1	36	319	365	0,90	4,50	0,90	0,80	0,10	0,30
2006/10/16 - 04:54	10	25	381	518	934	0,57	11,17	0,29	0,97	0,42	-0,02
2014/09/05 - 08:36	40	12	348	672	1072	0,66	7,46	0,77	0,90	0,34	0,11
2015/01/22 - 19:28	2	6	68	568	644	0,89	8,75	0,25	0,97	0,11	0,03
Total	**105**	**61**	**2128**	**4350**	**6644**	**0,67**	**13,45**	**0,63**	**0,95**	**0,33**	**0,04**

Table 5.9: 2-4 km vs ST2.

Events	*Hits*	*Misses*	*False Alarms*	*Correct Negatives*	*Total*	ACC	BIAS	POD	FAR	POFD	HSS
2004/05/27 - 20:32	84	18	284	139	525	0,42	3,61	0,82	0,77	0,67	0,08
2004/11/07 - 12:47	1	226	426	850	1503	0,57	1,88	0,00	1,00	0,33	-0,24
2004/11/07 - 16:14	33	95	937	273	1338	0,23	7,58	0,26	0,97	0,77	-0,13
2006/07/03 - 10:18	44	0	56	163	263	0,79	2,27	1,00	0,56	0,26	0,49
2006/07/03 - 12:33	22	12	53	278	365	0,82	2,21	0,65	0,71	0,16	0,32
2006/10/16 - 04:54	91	280	236	327	934	0,45	0,88	0,25	0,72	0,42	-0,18
2014/09/05 - 08:36	68	79	569	356	1072	0,40	4,33	0,46	0,89	0,62	-0,06
2015/01/22 - 19:28	33	19	385	207	644	0,37	8,04	0,63	0,92	0,65	0,00
Total	**376**	**729**	**2946**	**2593**	**6644**	**0,45**	**3,01**	**0,34**	**0,89**	**0,53**	**-0,11**

Table 5.10: 4-5 km vs ST3.

Events	*Hits*	*Misses*	*False Alarms*	*Correct Negatives*	*Total*	ACC	BIAS	POD	FAR	POFD	HSS
2004/05/27 - 20:32	0	51	18	456	525	0,87	0,35	0,00	1,00	0,04	-0,05
2004/11/07 - 12:47	0	159	22	1322	1503	0,88	0,14	0,00	1,00	0,02	-0,03
2004/11/07 - 16:14	0	207	32	1099	1338	0,82	0,15	0,00	1,00	0,03	-0,04
2006/07/03 - 10:18	0	17	0	246	263	0,94	0,00	0,00	–	0,00	0,00
2006/07/03 - 12:33	0	18	0	347	365	0,95	0,00	0,00	–	0,00	0,00
2006/10/16 - 04:54	5	102	52	775	934	0,84	0,53	0,05	0,91	0,06	-0,02
2014/09/05 - 08:36	0	223	2	847	1072	0,79	0,01	0,00	1,00	0,00	0,00
2015/01/22 - 19:28	0	40	0	604	644	0,94	0,00	0,00	–	0,00	0,00
Total	**5**	**817**	**126**	**5696**	**6644**	**0,86**	**0,16**	**0,01**	**0,96**	**0,02**	**-0,02**

Notice that the "–" sign is used whenever, during the calculation, the denominator results null and, therefore, the division operation becomes meaningless.

Table 5.11: 4-6 km vs CO1.

Events	*Hits*	*Misses*	*False Alarms*	*Correct Negatives*	*Total*	ACC	BIAS	POD	FAR	POFD	HSS
2004/05/27 - 20:32	4	117	83	321	525	0,62	0,72	0,03	0,95	0,21	-0,19
2004/11/07 - 12:47	0	307	18	1178	1503	0,78	0,06	0,00	1,00	0,02	-0,02
2004/11/07 - 16:14	0	339	62	937	1338	0,70	0,18	0,00	1,00	0,06	-0,09
2006/07/03 - 10:18	7	24	147	85	263	0,35	4,97	0,23	0,95	0,63	-0,15
2006/07/03 - 12:33	10	33	228	94	365	0,28	5,53	0,23	0,96	0,71	-0,16
2006/10/16 - 04:54	3	220	118	593	934	0,64	0,54	0,01	0,98	0,17	-0,18
2014/09/05 - 08:36	4	452	37	579	1072	0,54	0,09	0,01	0,90	0,06	-0,06
2015/01/22 - 19:28	5	118	126	395	644	0,62	1,07	0,04	0,96	0,24	-0,20
Total	**33**	**1610**	**819**	**4182**	**6644**	**0,63**	**0,52**	**0,02**	**0,96**	**0,16**	**-0,17**

Table 5.12: 6-10 km vs CO_2.

Events	Hits	Misses	False Alarms	Correct Negatives	Total	ACC	BIAS	POD	FAR	POFD	HSS
2004/05/27 - 20:32	1	228	0	296	525	0,57	0,00	0,00	0,00	0,00	0,00
2004/11/07 - 12:47	0	811	3	689	1503	0,46	0,00	0,00	1,00	0,00	0,00
2004/11/07 - 16:14	0	752	13	573	1338	0,43	0,02	0,00	1,00	0,02	-0,02
2006/07/03 - 10:18	0	152	3	108	263	0,41	0,02	0,00	1,00	0,03	-0,02
2006/07/03 - 12:33	0	228	7	130	365	0,36	0,03	0,00	1,00	0,05	-0,04
2006/10/16 - 04:54	0	184	23	727	934	0,78	0,13	0,00	1,00	0,03	-0,05
2014/09/05 - 08:36	0	387	2	683	1072	0,64	0,01	0,00	1,00	0,00	0,00
2015/01/22 - 19:28	13	446	0	185	644	0,31	0,03	0,03	0,00	0,00	0,02
Total	**14**	**3188**	**51**	**3391**	**6644**	**0,51**	**0,02**	**0,00**	**0,78**	**0,01**	**-0,01**

Table 5.13: gt 8 km vs CO_3, HSL, and HSXL.

Events	Hits	Misses	False Alarms	Correct Negatives	Total	ACC	BIAS	POD	FAR	POFD	HSS
2004/05/27 - 20:32	0	163	0	362	525	0,69	0,00	0,00	–	0,00	0,00
2004/11/07 - 12:47	0	621	0	882	1503	0,59	0,00	0,00	–	0,00	0,00
2004/11/07 - 16:14	8	535	0	795	1338	0,60	0,01	0,01	0,00	0,00	0,02
2006/07/03 - 10:18	3	93	0	167	263	0,65	0,03	0,03	0,00	0,00	0,04
2006/07/03 - 12:33	0	186	0	179	365	0,49	0,00	0,00	–	0,00	0,00
2006/10/16 - 04:54	16	182	0	736	934	0,81	0,08	0,08	0,00	0,00	0,12
2014/09/05 - 08:36	1	204	0	867	1072	0,81	0,00	0,00	0,00	0,00	0,01
2015/01/22 - 19:28	11	241	0	392	644	0,63	0,04	0,04	0,00	0,00	0,05
Total	**39**	**2225**	**0**	**4380**	**6644**	**0,67**	**0,02**	**0,02**	**0,00**	**0,00**	**0,02**

Notice that the "–" sign is used whenever, during the calculation, the denominator results null and, therefore, the division operation becomes meaningless.

the methods is further reduced, as underlined by the HSS parameter which reaches a cumulative negative value. In summary what generally emerges in this height range, is a considerable amount of false alarms, in addition to a low number of hit pixels.

Rather, any comparison concerning clouds with a top from 4 km up provides output data in total disagreement with the SAFNWC reference classes. The number of hits falls further, whereas compared to the previous cases the number of misses greatly increases. The HSS values are predominantely negative. Only the POFD parameter is high, due to the very poor population of the false alarms category than the correct negatives one. Therefore, once again, the MWCC classes from the ST3 onwards, tend to be underestimated when compared to their equivalent output from the VIS/IR application.

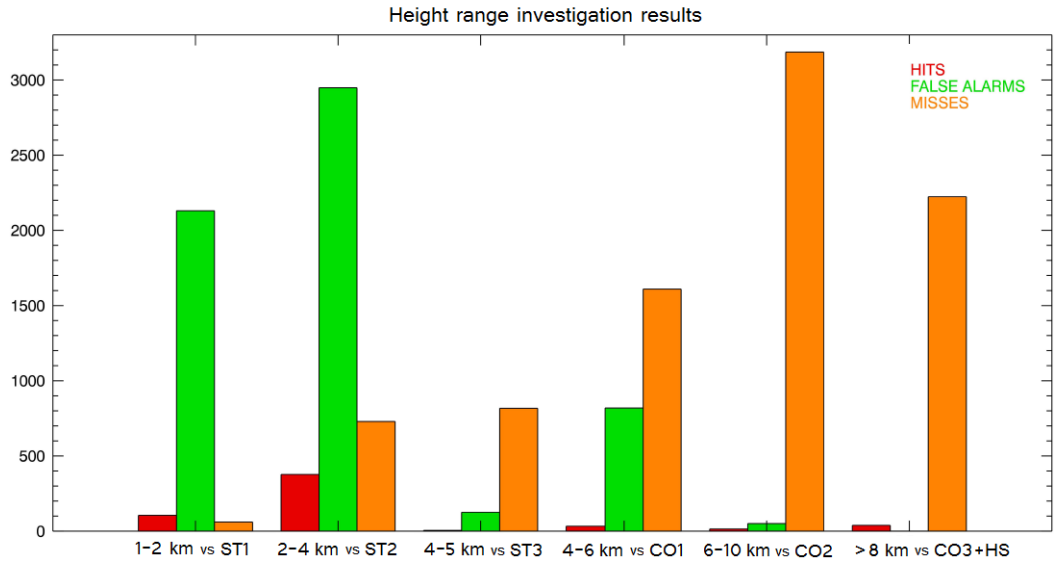

Figure 5.28: Summary of the study results produced by means of the dichotomous statistic applied to each of the compared height-class pairs. Note that the "correct negatives" category is not reported in the chart at issue because too populated than the others and this would have resulted in the flattening of the remaining categories, not allowing an easy reading.

Since the values of height obtained by using the first method do not seem to match the second one, a further study is carried out in order to realise, in correspondence with each MWCC category, which height values the SAFNWC PGE03 provides.

The histograms in figures 5.29-5.31 show, in correspondence with each MWCC class, the occurrence of each height value provided by the aforementioned SAFNWC product.

For the first three stratiform classes the cloud top height product shows a very varied information. The height values in question, in fact, range over the wide band, going from 0 until, approximately, 12 km. In correspondence with the ST1 category a bimodal distribution results: a first mode is detected with the maximum between 3 and 4 km and a second one with a lower peak between 8 and 9 km. Even the ST2 seems to be characterized by two predominant modes, with greater values around 5 and 9 km, and a third, much less populated within the atmospheric layer between 0 and 2 km height. As regards the ST3, the sample connected therewith is definitely less populous of the previous two. This depends on the fact that, being a transition category, it can easily be superimposed on the next CO1. However, even in this case, two main groupings around 6 and 9 km can be observed.

On the other hand, the distributions relating to convective categories, behave differently. The CO1, while still occupying a wide enough range, do not start from the first kilometers of the atmosphere, but extends from 5 up to 5 km. The CO2 and CO3 categories, indeed, match data in height between 8 and 13 km and the same is true for the few pixels related to the HSL. Note that the HSXL results are not present because no pixels belonging to such category remained after the remapping stage.

Ultimately, the results achieved in this section with respect to the previous one, are precisely supplied by the latter histograms. These further demonstrate that, albeith both softwares, in principle, supply a cloud classification linked to cloud top height information, in practice there are not correspondences among the cloud category associated to the same cloud top height ranges.

The SAFNWC retrieval tool, in effect, being very sensitive to the top temperature of a cloud, brings the actual level reached by this. The MWCC, on the other hand, exploiting the capability of the microwaves is able to give an information about the levels that are located more deeply within the atmospheric column. Therefore, in the presence of multi-layer systems, of which schematic examples are in figure 5.32, and in which a thin and high cloud surmounts some lower and thicker one, the VIS/IR software will give info on the system top, rather the MW one will tend to report data relating to the underlying layers. In the presence of well vertically structured deep convention, instead, the two output will tend to comply, although the microwaves will inevitably give an information related to the core rather than to the actual system top.

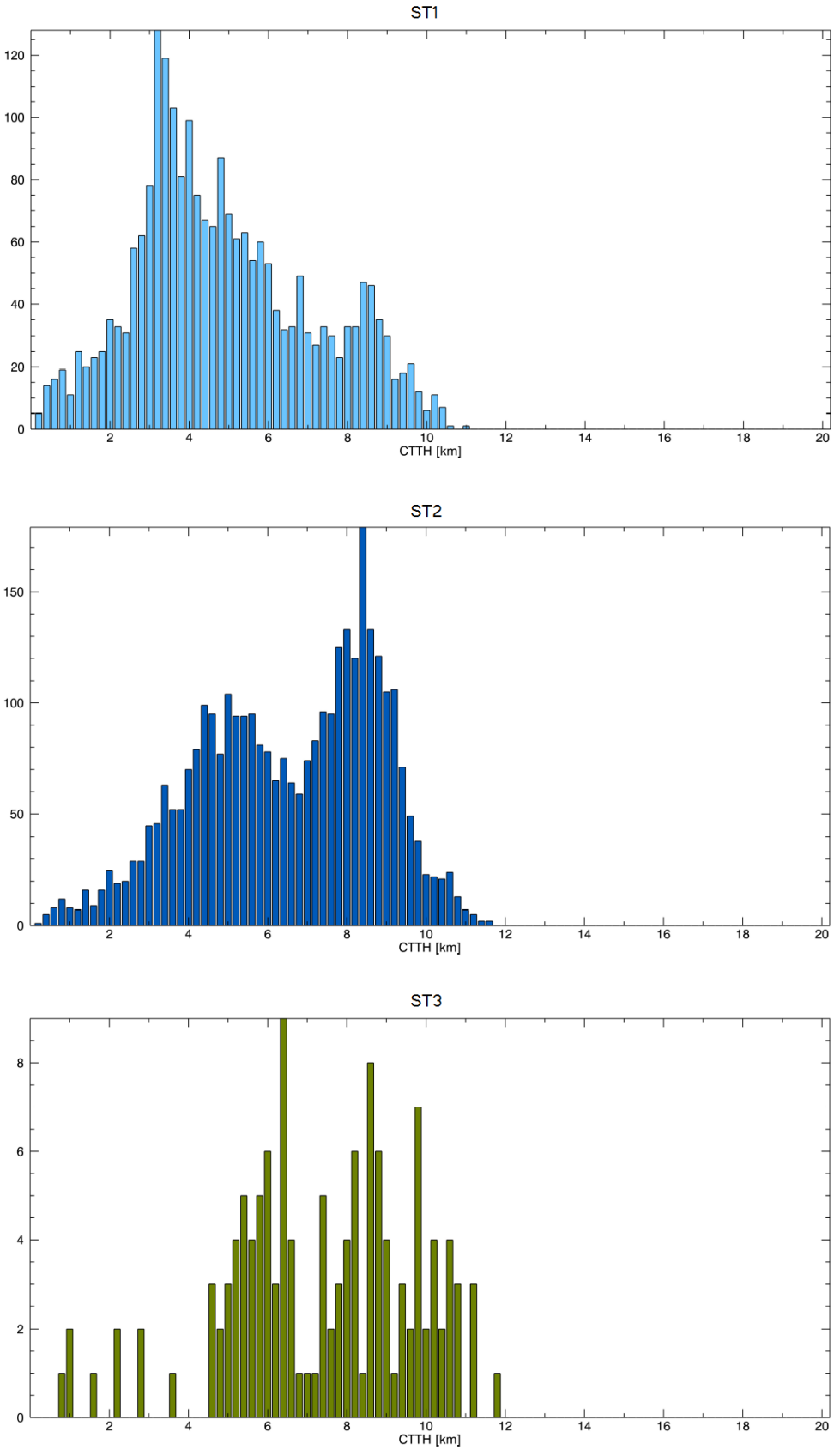

Figure 5.29: Cloud top heights by SAFNWC attributed to the pixels belonging to ST1, ST2 and ST3 MWCC categories.

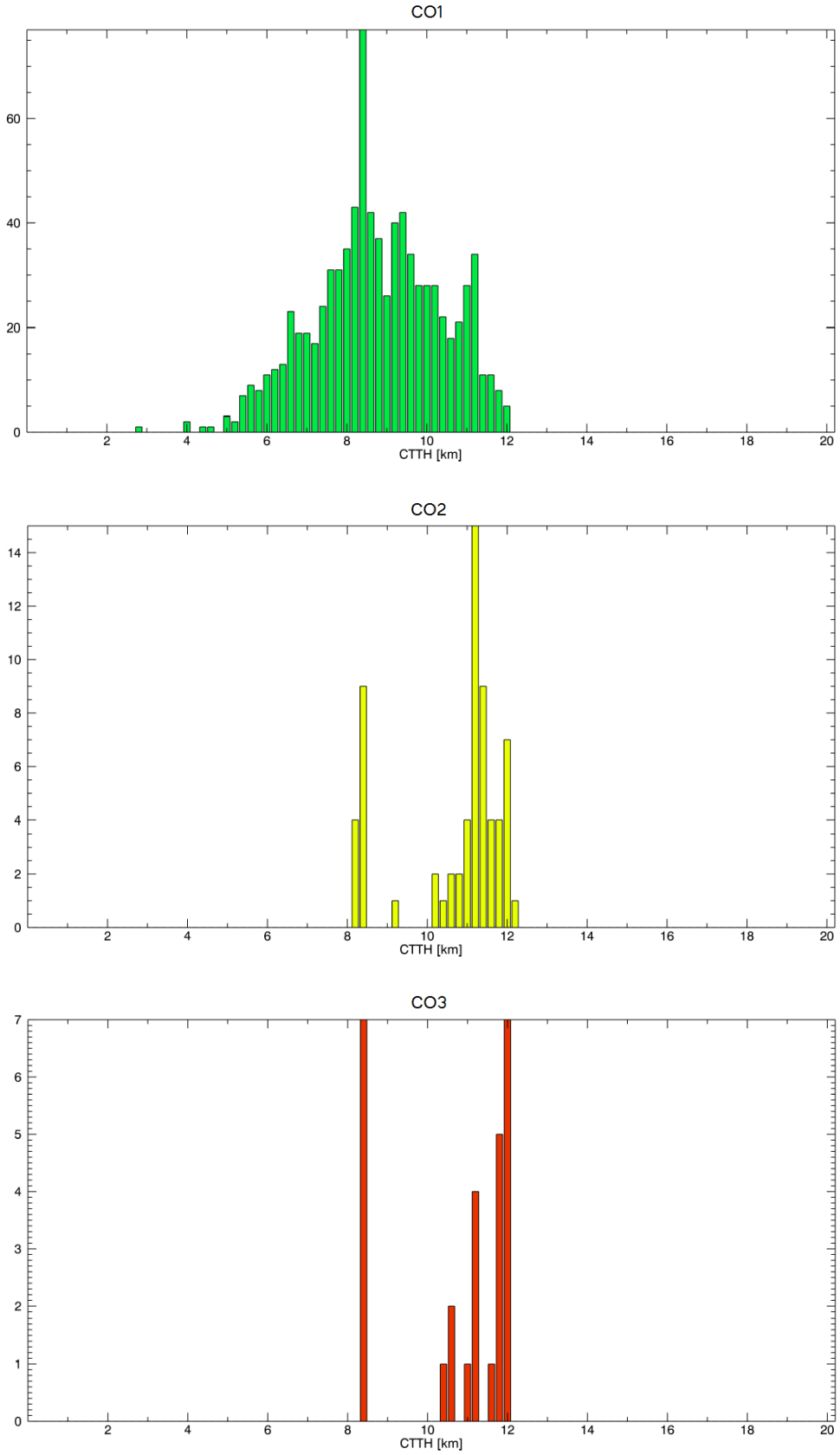

Figure 5.30: Cloud top heights by SAFNWC attributed to the pixels belonging to CO_1, CO_2 and CO_3 MWCC categories.

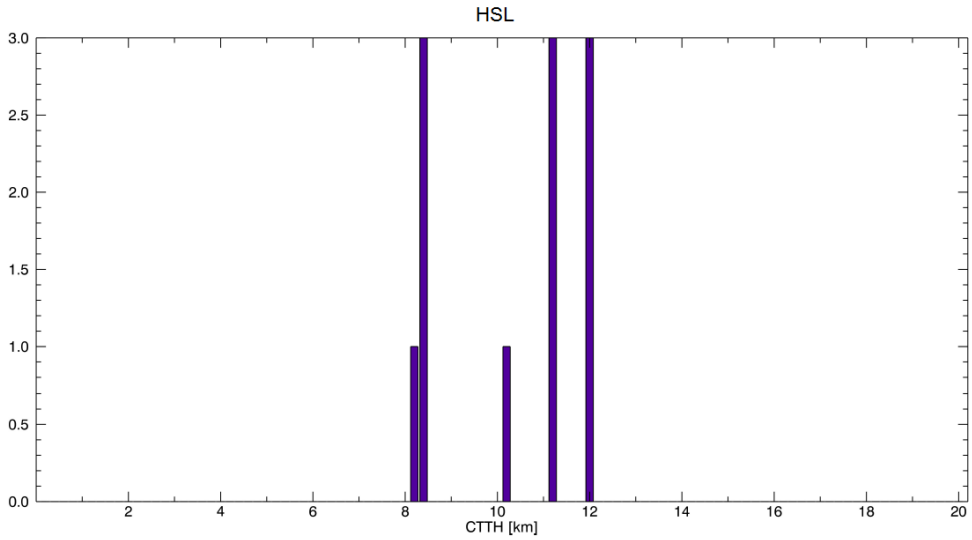

Figure 5.31: Cloud top heights by SAFNWC attributed to the pixels belonging to HSL category.

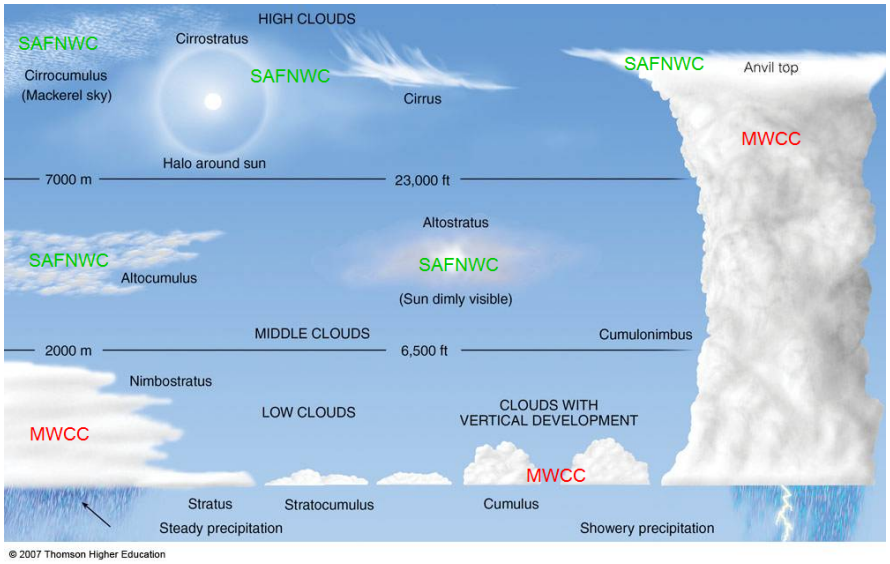

Figure 5.32: Multilayer system outline highlighting the cloud type to which each software is responsive.

6

CONCLUDING REMARKS

The need to detect and classify cloud cover over a specific area is a problem on which most studies have been focused. Over the last 100 years, a number of operational algorithms have been designed with this purpose. A large part of them was based on radiance data acquired by satellite sensors in the VIS/IR wavelenghts. Such specific region of the spectrum, in fact, is particularly suitable to be used in the threshold tests aimed to distinguish clouds from underlying surfaces. These methods are also able to give back information on cloud top height or hydrometeor phase in order to derive an adequate cloud categorisation.

In more recent times, another portion of the electromagnetic spectrum has begun to be studied in order to exploit its potential in the cloud retrieval and categorization fields. We are dealing with the MW radiation, previously used only for the water vapour content or temperature profiling of the atmospheric column, to obtain a rainfall estimation or finally in order to investigate the underlying surfaces.

The object of this thesis was to compare the output from two algorithms for cloud detection and classification based on totally different physical principles. We also aimed to quantitatively evaluate their differences by focusing on the technical and phenomenological causes.

The two methods chosen to be comparared are the SAFNWC software package, working on data in the VIS/IR range of the MSG-SEVIRI sensor, and the MWCC algorithm, built in a rainfall retrieval context then acquiring an its own autonomy, conceived for the exploitation of the MW spectral channels of AMSU-B/MHS sensors.

Firstly the capability of cloud detection of the two different systems has been tested, by comparing the Cloud Masks they produced. This analysis has shown that the two methods are in agreement on the cloud cover detection (POD = 0.62, FAR = 0.27), although some critical situations stand out. More specifically, the MWCC fails to reveal clouds which according to SAFNWC are fractional clouds and cirrus clouds. In addition, it lacks also the detection of a series of very low and high opaque clouds, although in a less extent than the previous. For what concerns the fractional clouds and the thin cirrus category, the MWCC behaviour is not completely unexpected since the MW radiation is very sensitive to the particle size and cloud optical depth, and thus it tends to miss the cloud edges of which this category is mainly composed. Moreover, the thick cirrus and high opaque clouds are perhaps not detected due to the way the MWCC has been conceived. Actually, it studies the convective systems rising from the lower atmospheric layers and then continuing to extend in height and for this reason, it is not able to reveal stratiform isolated systems. On the other hand, low clouds may be undetected because too low with respect to the detection domain of the algorithm wich approximately starts at 1-2 km of height. In effect, the lower and upper limits of the height ranges, in which each MWCC cloud category is

defined, depend on the heights at which the weighting functions peak. Moreover these heights are greatly affected by atmosphere and surface temperature. Since in the present work a seasonal study has not been carried out, we might have considered some situation in which the lower limit was raised over 1 km, thus losing all of the clouds below wich on the contrary the SAFNWC software has detected.

On the other hand the SAFNWC clear pixels which are cloudy according to the MWCC, mainly belong to the ST1 and ST2 typologies. These latter are fairly uncertain classes, usually exploited with the only purpose to be able to classify the next convective cloud levels. It means that a simple large amount of water vapour in a low atmospheric layer can be misinterpreted and then wrongly flagged as very low cloud. Nevertheless these could also be due to an underestimation of the actual cloud cover by the SAFNWC CMa processing algorithm.

After this first analysis stage, we have tested the pixels classified as cloudy according to both softwares, in order to understand if they were also in agreement on the detected cloud type. Since semi-transparent ice clouds (i.e. the cirrus clouds) were not included among the MWCC cloud classes, unlike the SAFNWC software, we have firstly evaluated which cloud type, and to what extent, the MWCC provided in correspondence to the pixels classified as cirrus clouds by the VIS/IR based method. By performing an inter-comparison on all the available cases, it appears that, where the SAFNWC senses a cirrus cloud, the MWCC reveals mostly the ST1 and ST2 categories, and in a lower amount even the CO1 and ST3.

The coincidence of cirrus above low or medium clouds with the lowest MWCC classes is justified once again by the operating MW algorithm mechanism. In effect, this can not detect high clouds if these are significantly separated from the overlying ones, but it is designed to sense the lower overlying cloud layers. This is also confirmed by the occurrence of ST1 and ST2, followed by the less populated CO1 and ST3.

With regard to the thin and thick cirrus categories, a more accurate analysis has been performed via a separate study between the daytime and night-time/twilight scenes. During daytime, when it is possible to identify the multi-layer systems, in correspondence with the thick cirrus class, the ST1 and ST2 amount is drastically reduced. Rather the biggest contribution to the total amount is given by the low solar elevation scenes. This suggested that the methods have recognized different cloud levels: the SAFNWC tools have recorded the high cirrus clouds, rather the MWCC algorithm has revealed the lower atmospheric layer content. For the thin cirrus class the question is entirely analogous to that just faced for the previous class. The only difference is that the possibility to make an isolated and high cloud detection is not precluded by a limitation of the algorithm, but by a physical feature on which this is based.

After discussing the cirrus question we proceed with the inter-comparison among the MWCC categories and the SAFNWC opaque cloud classes. This is performed by selecting class pairs on the basis of the height range in which they are defined.

The overall observed tendency of the MWCC software, with respect to the SAFNWC one, is to overestimate the first cloud classes, ST1 and ST2. This trend is reversed

with the increasing altitude. In other words, the lower is the cloud top, the more SAFNWC seems to miss it. Viceversa, the more the cloud top height grows up, the more the MWCC not reveal a certain cloud portion, rather detected by means of the SAFNWC tool.

For each investigated pair of classes there are many grid cells where the two algorithms do not agree, which we analysed in order to understand by what kind of clouds they were populated. The general emerging tendency indicates that the cloud top height achieved by means of the VIS/IR classification method results higher than that determined by using the MW classifier. Just the opposite occurs in the misses instance. In other words, with respect to what the SAFNWC finds, the MWCC pushes down the cloud top height level. On the contrary, the SAFNWC cloud type outputs are shifted upwards with respect to those provided by the other examined software. Overall, this behavior can be explained bringing up the different physical features on which the classification algorithms are based. The SEVIRI sensor, on which the SAFNWC package works, since has channels in the VIS/IR, detects the cloud top properties by measuring the reflected or emitted radiation. In this way, it intercepts the first system starting at the top and often fails to see beyond that. The MWCC, on the other hand, being based on the microwave electromagnetic radiation is very inclined to penetrate the cloud more than the former. In addition, this is designed to investigate the vertical structure of convective towers, reconstructing their development, layer by layer, and starting from the bottom. For this reason, it seems to show the opposite trend, lacking in identifying altostratus-cirrus formations which are not part of a deep cloud, but showing more sensitivity to the water vapour masses occupying the lower atmospheric layers, sometimes overrating that or incorrectly reading the radiances recorded by the used sensor.

In the final stage of the present work even the height ranges in which each MWCC class is defined have been tested by using the SAFNWC CTTH product data. It was very useful in order to collect additional information on the joint behavior of the two algorithms. The trend displayed in this case, is approximately the same encountered in the cloud type classes inter-comparison. The MW software seems to overestimate clouds in lower atmospheric levels, that is between 1 and 4 km, compared to the SAFNWC detections. On the other hand any comparison concerning clouds with a top from 4 km up provides output data in total disagreement with the SAFNWC reference classes. The MWCC classes from the ST3 onwards, tend to be underestimated when compared to their equivalent output from the VIS/IR application.

Since the values of height obtained by using the first method do not seem to match the second one, a further study is carried out in order to realise, in correspondence with each MWCC category, which height values the SAFNWC PGE03 provides. The results thus achieved underline further that in practice there are not any correspondences among the height range in which each MWCC class is defined and the CTTH SAFNWC output. This is especially true for the ST categories, while the agreement starts to be more consistent for the CO.

The more interesting matter which emerges from this work is the disagreement between the cloud type and cloud top height outputs provided by the two tested softwares. Although they intend to provide the same kind of information, in reality they return quite different details on the same atmospheric column. This can be a very important warning for the users of such a kind of operatiolnal algorithms. For example, in a situation where a rainfall retrieval in a convective sistem needs, a VIS/IR based software exploits measurements of the entire cold cloud top. Contrarily a MWCC-like classification method can help to identify the real convective and precipitating core.

Another important detail which emerges from this research work is the possibility in the MWCC improvement. More specifically the ranges within the different cloud classes are defined can be further narrowed thus providing a greater degree of detail. For instance, the need for more targeted seasonal studies has appeared, which can represent the next step in such software development.

ACRONYMS

ACC accuracy . . . 27
AMSR Advanced Microwave Scanning Radiometer . . . 12
AMSU-B Advanced Microwave Sounding Unit B . . . v
APOLLO AVHRR Processing scheme over cLouds, Land and Oceans . . . 9
AVHRR Advanced Very High Resolution Radiometer . . . 8
BIAS bias . . . 27
BT brightness temperature . . . 17
BTD brightness temperature difference . . . 15
CMa Cloud Mask . . . 2
CO convective . . . 24
CT Cloud Type . . . 2
CTTH Cloud Top Temperature/Height . . . 2
DMSP Defense Meteorological Satellite Program . . . 12
ECMWF European Centre for Medium-Range Weather Forecasts . . . 18
EOS Earth Observing System . . . 11
FAR false alarm ratio . . . 28
GOES Geostationary Operational Environmental Satellites . . . 10
HRV high-resolution visible . . . 16
HSL Hail Storm Large . . . 24
HSS Heidke Skill Score . . . 28
HSXL Hail Storm EXtra Large . . . 24
IR infrared . . . 7
Lidar Light Detection and Ranging . . . 1
MetOp Meteorological Operational satellite programme . . . 21
MHS Microwave Humidity Sounder . . . v
MODIS Moderate Resolution Imaging Spectroradiometer . . . 11
MSG Meteosat Second Generation . . . 11
MVIRI Meteosat Visible and Infrared Imager . . . 10
MW microwave . . . vi
MWCC MicroWave Cloud-type Classification . . . v

NASA National Aeronautics and Space Administration 7
NIR near-infrared 7
NOAA National Oceanic and Atmospheric Administration 8
NWP Numerical Weather Prediction 18
PGEs Product Generator Elements 16
POD probability of detection 27
POFD probability of false detection 28
RTTOV Rapid Transmissions for TOVs 18
SAFNWC Satellite Application Facility in support of NoWCasting and very short range forecasting v
SCANDIA SMHI Cloud ANalysis model using DIgital AVHRR data 10
SEVIRI Spinning Enhanced Visible and Infrared Imager v
SSM/I Special Sensor Microwave/Imager 12
SR Scanning Radiometer 8
ST stratiform 24
TGFs Terrestrial Gamma-ray Flashes 29
TIROS Television and Infrared Observation Satellite Program 7
UV ultraviolet 7
VIS visible 7
VIS/IR visible and infrared vi
VISSR Visible Infrared Spin-Scan Radiometer 10
WMO World Meteorological Organization 5
WRF Weather Research & Forecasting Model 36
183-WSL Water vapour Strong Lines at 183 GHz 13
6S Second Simulation of a Satellite Signal in the Solar Spectrum 18

BIBLIOGRAPHY

Ackerman, S., K. Strabala, W. Menzel, R. Frey, C. Moeller, and L. Gumley, 1998: Discriminating clear sky from clouds with MODIS. *J. Geophys. Res.*, **103** (D24), 32141-32157.

Aires, F., C. Prigent, W. Rossow, and M. Rothstein, 2001: A new neural network approach including first-guess for retrieval of atmospheric water vapour, cloud liquid water path, surface temperature and emissivities over land from satellite microwave observations. *J. Geophys. Res.*, **106** (D14), 1488714907.

Aires, F., F. Marquisseau, C. Prigent, and G. Sèze, 2011: A Land and Ocean Microwave Cloud Classification Algorithm Derived from AMSU-A and -B, Trained Using MSG-SEVIRI Infrared and Visible Observations. *Amer. Meteor. Soc.*, **139**, 2347-2366, doi:10.1175/MWR-D-10-05012.1

American Meteorological Society, 2014. Glossary of Meteorology Available online at http://glossary.ametsoc.org/wiki/Main_Page.

Arking, A., and J. D. Childs, 1985: Retrieval of Cloud Cover Parameters from Multispectrals Satellite Images. *J. Climate Appl. Meteor.*, **24**, 322-333.

Bennartz, R., and P. Bauer, 2003: Sensitivity of microwave radiances at 85-183 GHz to precipitating ice particles. *Radio Sci.*, **38** (4), 8075, doi:10.1029/2002RS002626.

Bennartz, R., A. Thoss, A. Dybbroe, and D. B. Michelson, 2002: Precipitation Analysis Using the Advanced Microwave Sounding Unit in Support of Nowcasting Applications. *Meteor. Appl.*, **9**, 177-189, doi:10.1017/ S1350482702002037.

Buehler, S. A., C. Jimenez, K. F. Evans, P. Eriksson, B. Rydberg, A. J. Heymsfield, C. J. Stubenrauch, U. Lohman, C. Emde, V. O. John, T. R. Sreerekha, and C. P. Davis, 2007: A concept for a satellite mission to measure cloud ice water path, ice particle size, and cloud altitude. *Quart. J. Roy. Meteor. Soc.*, **133**, 109-128.

Burns, B. A., X. Wu, ang G. R. Diak, 1997: Effects of precipitationand cloud ice on brightness temperatures in AMSU moisture channels. *IEEE Trans. Geosci. Remote Sens.*, **35**, 1429-1437.

Chevallier, F., 1999: TIGR-like sampled databases of atmospheric profiles from the ECMWF 50-levelforecast model. NWP SAF Report No. NWPSAF-EC-TR-001,

18.

Coakley, J. A., and F. P. Bretherton, 1982: Cloud cover from high resolution scanner data: Detecting and allowing for partially filled fields of view. *J. Geophys. Res.*, **87**, 4917-4932, doi: 10.1029/JC087iC07p04917.

Coakley, J. A., 1983: Properties of multilayered cloud systems from satellite imagery. *J. Geophys. Res.*, **88** (C15), 10818-10828.

Collins English Dictionary - Complete & Unabridged 10th Edition. Retrieved November 15, 2015, from Dictionary.com website: http://dictionary.reference.com/browse/warm-sector.

Cox, C., and W. Munck, 1954: Measurements of the roughness of the sea surface from photographs of the sun's glitter. *J. Opt. Soc. Amer.*, **44**, 838-850.

Derrien, M., F. Farki, L. Harang, H. Le Gléau, and A. Noyalet, 1993: Automatic Cloud Detection Applied to NOAA-11/AVHRR Imagery. *Remote Sens. Environ.*, **46**, 246-267.

Derrien, M., and H. Le Gléau, 2005: MSG/SEVIRI cloud mask and type from SAFNWC. *Int. J. Remote Sens.*, **26** (21), 4707-4732.

Derrien, M., 2012: Validation Report for "Cloud Products" (CMa-PGE01 v3.2, CT-PGE02 v2.2 & CTTH-PGE03 v2.2). SAF/NWC/CDOP/MFL/SCI/VR/06, Issue 1, 31. [Available online at http://www.nwcsaf.org/scidocs/Documentation/SAF-NWC-CDOP-MFL-SCI-VR-06_v1.0.pdf.]

Derrien, M., 2013: Algorithm Theoretical Basis Document for "Cloud Products" (CMa-PGE01 v3.2, CT-PGE02 v2.2 & CTTH-PGE03 v2.2). SAF/NWC/CDOP2/MFL/SCI/ATBD/01, Issue 3, 87. [Available online at http://www.nwcsaf.org/HTMLContributions/SUM/SAF-NWC-CDOP2-MFL-SCI-ATBD-01_v3.2.1.pdf.]

Desbois, M., G. Seze, and G. Szejwach, 1982: Automatic Classification of Clouds on METEOSAT Imagery: Application to High-Level Clouds. *J. Appl. Meteor.*, **21**, 401-412.

Dybbroe, A., A. Thoss, and K. G. Karlsson, 2001: Validation of Nowcasting SAF polar platform products. *Proc. of the 2001 Eumetsat Meteorological Satellite Conference, 15 October 2001, Antalya, Turkey*, EUM P33 (Darmstadt: Eumetsat), 444-451.

Eyre, J. R., 1991: A fast radiative transfer model for satellite sounding systems. *ECMWF Res. Dept. Tech. Memo.*, **176**. ECMWF, Reading, UK.

Ferraro, R., F. Weng, N. Grody, and A. Basist, 1996: An eight-year (19871994) time series of rainfall, clouds, water vapor, snow cover, and sea ice derived from SSM/I measurements. *Bull. Amer. Meteor. Soc.*, **77**, 891905.

Fishman, G.J., and Coauthors, 1994: Discovery of Intense Gamma-Ray Flashes of Atmospheric Origin. *Science*, **264** (5163), 1313-1316.

Frey, R., S. Ackerman, Y. Liu, K. Strabala, H. Zhang, J. Key, and X. Wang, 2008: Cloud detection with MODIS. Part I: Improvements in the MODIS cloud mask for collection 5. *J. Atmos. Oceanic Technol.*, **25**, 10571072.

Gabriele, S., and F. Chiaravalloti, 2011: Piogge brevi e satellite METEOSAT. *Applicazioni meteoclimatiche nella regionalizzazione delle precipitazioni*, CNR - IRPI, 135-156.

Greenwald, T. J., G. Stephens, T. V. Haar, and D. Jackson, 1993: A physical retrieval of cloud liquid water over the global oceans using Special Sensor Microwave/Imager (SSM/I) observations. *J. Geophys. Res.*, **98** (D10), 1847118488.

Greenwald, T. J., and S. A. Christopher, 2002: Effect of cold clouds on satellite measurements near 183 GHz. *J. Geophys. Res.*, **107** (D13), 4170, doi:10.1029/2000JD000258.

Hong, G., G. Heygster, J. Miao, and K. Kunzi, 2005a: Detection of tropical deep convective clouds from AMSU-B water vapor channels measurements. *J. Geophys. Res.*, **110**, DO5205, doi:10.1029/2004JD004949.

Hong, G., G. Heygster, J. Miao, and K. Kunzi, 2005b: Sensitivity of microwave brightness temperatures to hydrometeors in a tropical deep convective cloud system at 89-190 GHz. *Radio Sci.*, **40**, RS4003, doi:10.1029/2004RS003129.

Howard, L., 1803: On the Modifications of Clouds. J. Taylor, London.

Inoue, T., 1985: On the temperature and effective emissivity determination of semi-transparent cirrus clouds by bi-spectral measurements in the 10 mm window region. *J. Meteor. Soc. Japan*, **63**, 89-99.

Jedlovec, G., 2009: Automated Detection of Clouds in Satellite Imagery. *Advances in Geoscience and Remote Sensing*, G. Jedlovec (Ed.), ISBN: 978-953-307-005-6, InTech, doi: 10.5772/8326.

Jin, Y., and W. Rossow, 1997: Detection of cirrus overlapping low level clouds. *J. Geophys. Res.*, **102**, 1727-1737.

Karlsson, K.G., 1989: Development of an operational cloud classification model. *Int. J. Remote Sens.*, **10**, 687-693.

Karlsson, K.G., and E. Liljas, 1990: The SMHI model for cloud and precipitation analysis from multispectral AVHRR data. PROMIS Report 10, SMHI, 74 pp.

Karlsson, K.G., 1996: Cloud classifications with the SCANDIA model, Reports Meteorology and Climatology, SMHI, 36 pp.

Kotchenova, S. Y., E. F. Vermote, R. Matarrese, and F. J. Klemm, 2006: Validation of a vector version of the 6S radiative transfer code for atmospheric correction of satellite data. Part I: Path radiance. *Applied Optics*, **45** (26), 6762-6774.

Kriebel, K. T., G. Gesell, M. Kästenr, and H. Mannstein, 2003: The cloud analysis tool APOLLO: Improvements and validations. *Int. J. Remote Sens.*, **24** (12), 2389-2408.

Kriebel, K. T., R. W. Saunders, and G. Gesell, 1989: Optical properties of clouds derived from fully cloudy AVHRR pixels. *Beitr. Phys. Atmos.*, **8** (26), 165-171.

Laviola, S., and V. Levizzani, 2011: The 183-WSL Fast Rain Rate Retrieval Algorithm. Part I: Retrieval Design. *Atmos. Res.*, **99**, 443461.

Laviola, S., V. Levizzani, E. Cattani, and C. Kidd, 2013: The 183-WSL fast rain rate retrieval algorithm. Part II: Validation using ground radar measurements. *Atmos. Res.*, **134**, 77-86.

Liljas, E., 1984: Processed satellite imageries for operational forecasting. Swedish Meteorological and Hydrological Institute, Norrköping, Sweden, 43 pp.

Marisaldi, M., and Coauthors, 2010: Detection of terrestrial gamma ray flashes up to 40 MeV by the AGILE satellite. *J. Geophys. Res.*, **115**, A00E13, doi:10.1029/2009JA014502

Minnis, P., and E. F. Harrison, 1984: Diurnal Variability of Regional Cloud and Clear-Sky Radiative Parameters Derived from GOES Data, Part I: Analysis Method. *J. Climate Appl. Meteor.*, **23**, 993-1011.

Menzel, P. , 2012: *Intro to VIS-IR Radiation Lab*, Lecture-Labs in Bologna & Potenza, UW/CIMSS/AOS.

Muller, B. M., H. E. Fuelberg, and X. Xiang, 1994: Simulations of the effects of water vapor, cloud liquid water and ice on AMSU moisture channel brightness temperatures. *J. Appl. Meteor.*, **33**, 1133-1154.

NOAA, 2009: NOAA KLM USER'S GUIDE. Accessed 18 August 2015. [Available online at http://www.ncdc.noaa.gov/oa/pod-guide/ncdc/docs/klm/index.htm.]

O'Dell, C., J. Wentz, and R. Bennartz, 2008: Cloud liquid water path from satellite-based passive microwave observations: A new climatology over the global oceans. *J. Climate*, **21**, 17211739.

Platnick, S., M. D. King, S. A. Ackerman, W. P. Menzel, B. A. Baum, J. C. Riédi, and R. A. Frey, 2003: The MODIS Cloud Products: Algorithms and Examples From Terra. *IEEE Trans. Geosci. Remote Sens.*, **41** (2), 459-473.

Porcù, F., and V. Levizzani, 1992: Cloud classification using Meteosat VIS/IR imagery. *Int. J. Remote Sens.*, **13** (5), 893-909.

Rossow, W. B., E. Kinsella, and L. Garder, 1983: Seasonal and Global cloud variations deduced from polar orbiting satellite radiance measurements. *Proc. Fifth Conf. on Atmos. Radiation*, Baltimore, Amer. Meteor. Soc., 195-198.

Rossow, W.B., F. Mosher, E. Kinsella, A. Arking, M. Desbois, E. Harrison, P. Minnis, E. Ruprecht, G. Seze, C. Simmer, and E. Smith, 1985: ISCCP cloud algorithm intercomparison. *J. Clim. Appl. Meteorol.*, **24**, 877-903.

Saunders, R. W., T. J. Hewison, S. J. Stringer, and N. C. Atkinson, 1995: The radiometric characterization on AMSU-B. *IEEE Trans. Microwave Theory Tech.*, **43**, 760-771.

Saunders, R. W., M. Matricardi, and P. Brunel, 1999: An Improved Fast Radiative Transfer Model for Assimilation of Satellite Radiance Observations. *Quart. J. Roy. Meteor. Soc.*, **125**, 1407-1425.

Saunders, R. W., and K. T. Kriebel, 1988: An improved method for detecting clear sky and cloudy radiances from AVHRR data. *Int. J. Remote Sens.*, **9**, 123-150.

Schmetz, J., P. Pili, S. Tjemkes, D. Just, J. Kerkmann, S. Rota, and A. Ratier, 2002: An Introduction to Meteosat Second Generation (MSG). *Bull. Amer. Meteor. Soc.*, **83**, 977-992.

Schmetz, J., S. A. Tjemkes, M. Gube, and L. van de Berg, 1997: Monitoring Deep Convection and Convective Overshooting with Meteosat. *Adv. Space Res.*, **19**,

433-441.

Simmer, C., E. Raschke, and E. Ruprecht, 1982: A method for determination of cloud properties from two-dimensional histograms. *Annals of Meteor.*, **18**, 130-132.

Smith, D. M., L. I. Lopez, R. P. Lin, and C. P. Barrington-Leigh, 2005: Terrestrial gamma-ray flashes observed up to 20 MeV. *Science*, **307** (5712), 1085-1088, doi:10.1126/science.1107466

Stowe, L. , and P. McClain, 1991: Global distribution of cloud cover derived from NOAA/AVHRR operation satellite data. *Adv. Space Res.*, **11** (3), 51-54.

Tanre, D., C. Deroo, P. Duhaut, M. Herman, J.J. Morcrette, J. Perbos, and P.Y. Deschamps, 1990: Description of a computer code to simulate the satellite signal in the solar spectrum: the 5S code. *Int. J. Remote Sens.*, **11**, 659-668.

Turk, F. J., and S. D. Miller, 2005: Toward Improved Characterization of Remotely Sensed Precipitation Regimes With MODIS/AMSR-E Blended Data Techniques. *IEEE Trans. Geosci. Remote Sens.*, **43**, 1059-1069.

Wallace, J. M. and P. V. Hobbs, 1977: Atmospheric Science: An Introductory Survey. Academic Press Inc, Orlando, Florida.

Wang, J. R., and L. A. Chang, 1990: Retrieval of water vapour profiles from microwave radiometric measurements near 90 and 183 GHz. *J. Appl. Meteor.*, **29**, 1005-1013.

Wang, J. R., J. Zhan, and P. Racette, 1997: Storm-Associated Microwave Radiometric Signatures in the Frequency Range of 90-220 GHz. *J. Atmos. Oceanic Technol.*, **14**, 13-31.

Weng, F., L. Zhao, R. Ferraro, G. Poe, X. Li, and N. Grody, 2003: Advanced microwave sounding unit cloud and precipitation algorithms. *Radio Sci.*, **38**, 80868096.

Wilheit, T. T., 1990: An algorithm for retrieving water vapor profiles in clear and cloudy atmospheres from 183 GHz radiometric measurements: simulation studies. *J. Appl. Meteor.*, **29**, 508-515.

WMO, 1956. International Cloud Atlas. Volumes I and II.

RINGRAZIAMENTI

Desidero in primo luogo ringraziare il prof. Levizzani, relatore di questa tesi, per avermi dato la possibilità di partecipare attivamente alle attività del suo gruppo di ricerca. Questa esperienza formativa è stata per me fondamentale nella crescita professionale e personale, e mi ha permesso di acquisire nuove e interessanti competenze scientifiche, sia teoriche che pratiche.
Un sentito ringraziamento va alla dott.ssa Cattani, la quale, fin dai miei primissimi giorni di lavoro al CNR si è sempre dimostrata disponibile a rispondere ad ogni quesito volessi porle, affiancandomi e supportandomi con infinita pazienza, disponibiltà e professionalità.
Ringrazio, inoltre, il dottor Laviola per avermi affidato il compito di testare, studiare e approfondire il progetto da lui stesso sviluppato.

Un affettuoso grazie va a tutti i miei amici più cari, alcuni fisicamente vicini, altri a chilometri di distanza, ma tutti ugualmente presenti e pronti farmi a sorridere e distrarre, ogni qualvolta io ne avessi bisogno. Ognuno a modo suo è stato fondamentale nel raggiungimento di questo traguardo.
Fra di loro, un pensiero a parte va a Michela, senza la quale, nell'ultimo periodo non ce l'avrei fatta! Come si dice, « coi matti ci vuole pazienza » e lei ne ha avuta tantissima.

Grazie a Matteo... per essermi stato accanto nonostante tutto. Fra i mille imprevisti, tensioni e cambiamenti che si palesavano nelle nostre vite, è ugualmente riuscito a farmi sentire la sua presenza, il suo affetto e il suo calore. Che fossimo in due città o in due stati differenti, non siamo mai stati veramente distanti. « Grazie per i denti stretti, i difetti, per le botte d'allegria... ».

Un grazie enorme va alla mia famiglia: ad Antonio, il mio fratellone, che da quando sono nata, a volte senza neanche accorgersene, è sempre stato per me un modello a cui ispirarsi, e a mamma e papà, senza i quali raggiungere questo traguardo sarebbe stata una pura illusione. Grazie per gli sforzi e i sacrifici fatti, per aver sofferto e gioito insieme a me e per essere sempre stati lì a supportarmi, incoraggiarmi e a crederci, anche quando nemmeno io avevo più la forza di farlo.

Infine grazie a me stessa.. per non aver mollato, consapevole che questo è soltanto il punto di partenza, non di arrivo. Come qualcuno ha detto:

«...it's a long way to the top.. ♪».